

**The root flow of horizontal axis wind turbine blades
Experimental analysis and numerical validation**

Akay, Büsra

DOI

[10.4233/uuid:2a3f9993-d406-42ee-9d64-57da3fbc0d12](https://doi.org/10.4233/uuid:2a3f9993-d406-42ee-9d64-57da3fbc0d12)

Publication date

2016

Document Version

Final published version

Citation (APA)

Akay, B. (2016). *The root flow of horizontal axis wind turbine blades: Experimental analysis and numerical validation*. [Dissertation (TU Delft), Delft University of Technology]. <https://doi.org/10.4233/uuid:2a3f9993-d406-42ee-9d64-57da3fbc0d12>

Important note

To cite this publication, please use the final published version (if applicable).
Please check the document version above.

Copyright

Other than for strictly personal use, it is not permitted to download, forward or distribute the text or part of it, without the consent of the author(s) and/or copyright holder(s), unless the work is under an open content license such as Creative Commons.

Takedown policy

Please contact us and provide details if you believe this document breaches copyrights.
We will remove access to the work immediately and investigate your claim.

Buşra Akay

The root flow of horizontal axis wind turbine blades

Experimental analysis and numerical validation



The root flow of horizontal axis wind turbine blades

Experimental analysis and numerical validation

The root flow of horizontal axis wind turbine blades

Experimental analysis and numerical validation

PROEFSCHRIFT

ter verkrijging van de graad van doctor
aan de Technische Universiteit Delft,
op gezag van de Rector Magnificus Prof. ir. K.Ch.A.M. Luyben,
voorzitter van het College voor Promoties,
in het openbaar te verdedigen op
maandag 12 September 2016 om 10.00 uur

door

Buşra AKAY

Master of Science in Aerospace Engineering,
Middle East Technical University,
Ankara, Turkey
geboren te Develi, Turkey.

This dissertation has been approved by the promotor:

Prof. dr. G.J.W van Bussel
Copromotor Dr.ir. C.J. Simão Ferreira

Composition of the doctoral committee:

Rector Magnificus	chairman
Prof. dr. G.J.W van Bussel	Delft University of Technology, promotor
Dr. ir. Eng. C.J. Simão Ferreira	Delft University of Technology, copromotor

Independent members:

Prof. dr. ir. G.A.M. van Kuik	Delft University of Technology
Prof. dr. F. Scarano	Delft University of Technology
Prof. dr. J. van Beck	The von Karman Institute for Fluid Dynamics, Belgium
Prof. dr. T. Anders Nygaard	Norwegian University of Life Sciences, Norway
Dr. S. Schreck	National Renewable Energy Laboratory, USA

Copyright © 2016 by Buşra Akay

All rights reserved. No part of the material protected by this copyright notice may be reproduced or utilized in any form or by any means, electronic or mechanical, including photocopying, recording or by any information storage and retrieval system, without the prior permission of the author.

Printed on recycled paper by Ridderprint BV, The Netherlands.
Cover design by Pierre Gousseau

Typeset by the author with the L^AT_EX Documentation System.

Author email: busra.akay@gmail.com

ISBN: 978 – 90 – 76468 – 15 – 0

An electronic version of this dissertation is available at
<http://repository.tudelft.nl/>

“Quality... you know what it is, yet you don’t know what it is. But that’s self–contradictory. But some things are better than others, that is, they have more quality. But when you try to say what the quality is, apart from the things that have it, it all goes poof! There is nothing to talk about. But if you can’t say what Quality is, how do you know what it is, or how do you know that it even exists? If no one knows what it is, then for all practical purposes it really does exist. What else are the grades based on? Why else would people pay fortunes for some things and throw others in the trash pile? Obviously some things are better than others... but what’s the “betterness”?... So round and round you go, spinning mental wheels and nowhere finding anyplace to get traction. What the hell is Quality? What is it? ”

Robert M. Pirsig, *Zen and the art of motorcycle maintenance*

Summary

Despite a long research history in the field of wind turbine aerodynamics, horizontal axis wind turbine (HAWT) blade's root flow aerodynamics is among the least understood topics. In this thesis work, a detailed investigation of the root flow is performed to gain a better insight into the features of this particular flow region and their influence on the overall air flow. Two- and three-dimensional flow analyses of a HAWT blade are performed for axial inflow conditions, with both experimental and numerical approaches.

In the experiments, a stereoscopic particle image velocimetry (SPIV) setup is used to measure velocity in the near wake region at different azimuth angles and around the blade at different radial positions. This experimental setup allows measuring three velocity components on 2D planes which can be used to construct three-dimensional flow fields. With this approach, a detailed description of the flow-field in the root region is obtained and 3D visualizations are presented.

Further analysis of the velocity fields allows illustrating and understanding the physics of the formation of the root flow structures for different blade geometries and their evolution in the blade's near wake for different blade tip speed ratios. The effect of the root vortex on the blade's root flow and in the near wake region is studied. In particular, the experimentally-observed spanwise flow in the blade's outer flow region (outside the boundary layer of the blade) questions the two-dimensional flow assumption of the classical momentum theory. The velocity fields are also used to deduce the loads on the blade through the calculation of the momentum change in the fluid.

In addition to the analysis of the experimental results, also comparisons with numerical simulations from Blade Element Momentum (BEM) and Computational Fluid Dynamics (CFD) are made. The (Open Foam) CFD results are validated by comparing the computed velocity fields with the PIV results and a good agreement is obtained. The comparison of the load predictions from the numerical and the experimental methods also shows a very good agreement,

which brings confidence about the capability of these numerical methods to estimate the forces along the blade.

This thesis has contributed to narrowing the knowledge gap in the field of HAWT blade's root flow aerodynamics by:

- (i) providing a solid experimental database of root flow velocities and vortical structures;
- (ii) investigating the existence and hence the role of the root vortex;
- (iii) studying the spanwise flow over the blade's surface and hence identifying the three-dimensionality of the flow in the outer flow region;
- (iv) comparing the experimental and numerical results to study and explain the physics of the root flow;
- (v) demonstrating that with advanced numerical tools realistic and complicated root flow details can be simulated.

Samenvatting

Ondanks de lange geschiedenis van onderzoek op het gebied van windturbine-aerodynamica, is de stroming rond de bladwortel van een horizontale-as windturbine (HAWT) een van de minst begrepen onderwerpen. Dit proefschrift beschrijft een gedetailleerde studie naar de stroming rond de bladwortel, om meer inzicht te krijgen in de eigenschappen van dit stromingsgebied en de invloed op de algemene luchtstroming. Twee- en driedimensionale stromingsanalyses zijn uitgevoerd aan het blad van een HAWT met axiale aanstroming, door middel van zowel experimentele als numerieke methodes.

In de experimenten is een stereoscopische *Particle Image Velocimetry* (SPIV) opstelling gebruikt om de snelheid te meten in het nabije zog voor verschillende azimuthoeken, en rond het blad voor verschillende radiale posities. Deze experimentele opstelling maakt het mogelijk om drie snelheidscomponenten in tweedimensionale vlakken te meten, wat gebruikt kan worden om driedimensionale snelheidsvelden te construeren. Met deze aanpak is een gedetailleerde beschrijving van het stromingsveld in het bladwortelgebied verkregen, en worden driedimensionale visualisaties gepresenteerd.

Verdere analyse van de snelheidsvelden maakt het mogelijk om voor verschillende bladgeometrieën de fysica van de stromingsstructuren bij de bladwortel, en hun evolutie in het nabije zog, te illustreren en begrijpen voor verschillende waarden van de snellopendheid. De invloed van de wervel bij de bladwortel op de stroming rond de bladwortel en in het nabije zog is onderzocht. In het bijzonder stelt de experimenteel geobserveerde radiale stroming in de buitenstroming van het blad (buiten de grenslaag van het blad) de aanname van tweedimensionale stroming in de klassieke impulsstheorie ter discussie. De snelheidsvelden zijn ook gebruikt om de belasting op het blad te bepalen, door berekening van de impulsverandering in de stroming.

Naast de analyse van experimentele resultaten zijn ook vergelijkingen gemaakt met numerieke simulaties door middel van de *Blade Element Momentum* (BEM) methode en *Computational Fluid Dynamics* (CFD). De (OpenFoam)

CFD resultaten zijn gevalideerd door berekende snelheidsvelden te vergelijken met PIV resultaten, en deze kwamen goed overeen. De belastingen berekend op basis van numerieke en experimentele methodes kwamen ook zeer goed overeen, wat vertrouwen geeft in het vermogen van deze numerieke methodes om de krachten op het blad te berekenen.

Dit promotieonderzoek heeft bijgedragen aan het verkleinen van de kennisloof op het gebied van de stroming rond de bladwortel van een HAWT door:

- (i) het beschikbaar maken van een betrouwbare experimentele database met snelheden en wervelstructuren in de stroming rond een bladwortel;
- (ii) onderzoek naar het bestaan en de rol van de wervel bij de bladwortel;
- (iii) het bestuderen van de radiale stroming over het bladoppervlak en het daaruit identificeren van de driedimensionaliteit van de stroming in het gebied van de buitenstroming;
- (iv) het vergelijken van experimentele en numerieke resultaten om de fysica van de stroming rond de bladwortel te bestuderen en verklaren;
- (v) te demonstreren dat realistische en gecompliceerde details van de stroming rond een bladwortel kunnen worden gesimuleerd met geavanceerde numerieke gereedschappen.

Contents

Summary	i
Samenvatting	iii
1 Introduction	1
1.1 Aerodynamic research in wind energy	2
1.1.1 Methods applied in wind turbine aerodynamics	2
1.2 Introduction to the root flow aerodynamics of a HAWT	7
1.2.1 Blade wake region	7
1.2.2 What is root flow?	9
1.2.3 Root vortex	11
1.2.4 3D flow in the root region	13
1.3 Formulation of the research questions	15
1.4 Thesis structure	17
2 Stereoscopic particle image velocimetry experiments	19
2.1 Wind tunnel and HAWT model	20
2.2 Stereoscopic particle image velocimetry	21
2.3 PIV measurement set-ups	23
2.3.1 Spanwise measurement set-up	24
2.3.2 Chordwise measurement set-up	24
2.4 Laser light reflection	25
2.5 Post processing of PIV data	27
2.6 Measurement uncertainty	28
2.6.1 Experimental uncertainties	28
2.6.2 Uncertainty in the PIV velocity fields	30
2.6.3 Uncertainty in the vorticity and in the pressure from PIV	32

3	Experimental investigation of the root flow in a HAWT	33
3.1	Velocity distributions in the root region	34
3.1.1	Axial velocity in the near wake region	36
3.1.2	Azimuthal velocity in the near wake region	36
3.1.3	Radial velocity in the near wake region	38
3.1.4	Tangential velocity around the blade	41
3.2	Vorticity distributions	42
3.2.1	3D vorticity in the root region	42
3.2.2	2D spanwise vorticity around the blade	46
3.2.3	2D azimuthal vorticity in the near wake region	46
3.3	Pressure distribution in the near wake region	51
3.4	Summary and chapter conclusions	53
4	Effects of geometry and tip speed ratio on the HAWT root flow	55
4.1	Comparison of three test cases	56
4.1.1	Velocity distributions in the near wake region	56
4.1.2	Vorticity distributions in the near wake region	62
4.1.3	Spanwise bound vorticity and the strength of trailing vortex	64
4.2	Summary and chapter conclusions	66
5	Role of the root vortex in three dimensional flow	69
5.1	Bound vorticity of the root vortex	70
5.2	Velocity induced by the root vortex	71
5.2.1	Root vortex strength in the near wake	71
5.2.2	Induced velocity from volume distribution of the root vorticity	73
5.3	Spanwise velocity in the inviscid-outer flow region	78
5.3.1	Spanwise velocity around the blade	78
5.3.2	Spanwise velocity over the blade	81
5.4	Summary and chapter conclusions	83
6	Aerodynamic loads from PIV, BEM and CFD	85
6.1	Methodology for load calculation from PIV velocity fields	86
6.1.1	Estimation of forces by contour approach	86
6.1.2	Estimation of pressure	88
6.2	CFD Simulations	89
6.2.1	Numerical procedure	90
6.2.2	Wall treatment and Boundary conditions	90
6.2.3	Computational domain	90

6.3	BEM calculations	91
6.3.1	Tip- and hub-loss corrections	92
6.3.2	3D correction for rotational effects on the airfoil characteristics	93
6.3.3	BEM simulations for the experimental rotors	93
6.4	Validation of CFD and BEM results with experimental loads	94
6.4.1	Blade 1: Normal force distribution	94
6.4.2	Blade 1: Tangential force distribution	98
6.4.3	Flow field around Blade 1: PIV vs. CFD	99
6.4.4	Blade 2: Normal force distribution	107
6.4.5	Blade 2: Tangential force distribution	107
6.4.6	Comparisons of load predictions: Blade 1 and 2	109
6.5	Summary and chapter conclusions	110
7	Conclusions and recommendations	113
7.1	Thesis Conclusions	113
7.2	Suggestions for future work	116
A	Appendix	117
A.1	Performed Experiments	117
A.2	Open jet facility (OJF)	118
A.3	Rotor Model	118
A.3.1	Force measurements	119
A.4	PIV system apparatus	120
A.4.1	Post-processing of PIV data	124
A.4.2	Uncertainties in the measurements	124
A.5	Circulation: Blade 2	125
A.6	Input data in BOT	126
A.7	Lift coefficient distribution	127
A.8	Additional CFD results	128
	Bibliography	133
	Nomenclature	141
	List of Figures	145
	List of Tables	151
	Acknowledgements	153

Curriculum vitae and list of publications

155

Chapter 1

Introduction

This chapter presents a review of the state-of-the-art of wind turbine root flow aerodynamics. The fundamental features of root flow aerodynamics are explained along with observations from earlier studies. Throughout this chapter, the findings of previous research are discussed with the knowledge of the root flow aerodynamics obtained from the present study. The contradictory results obtained from different studies are revealed which support the need for further research, like the one reported in the present thesis.

Chapter outline

- Section 1.1 presents a short background and some key methods in the aerodynamic research of wind turbines.
- Section 1.2.1 explains the flow in the blade wake area by focusing on the root region.
- Section 1.2.2 introduces the characteristics of the HAWT blade's root flow.
- Section 1.2.3 describes the formation of the root vortex and discusses the observations made in earlier studies.
- Section 1.2.4 presents a review of some of the previous research on the three dimensionality of the flow in the blade root region.
- Section 1.3 formulates the research questions which are discussed and analyzed throughout this thesis.

- Section 1.4 summarizes the thesis structure.

1.1 Aerodynamic research in wind energy

Wind turbine aerodynamics deals with the modeling of the interaction between the flow and the wind turbine rotor. The flow field in the modern wind energy rotor aerodynamics can be split into a global and local flow fields. While the global flow field covers the region from far upstream to far downstream of the turbine, the latter consists of only the viscous region in the vicinity of the blade (see Snel (1998)). Although the flow fields in these two regions are often studied independently for the sake of simplicity, the interaction between global and local flows cannot be ignored.

Important to note that besides aerodynamic modeling, which concerns the specific design of some parts of a wind turbine, integrated aeroelastic modeling is also necessary to predict the performance and structural deflections for the design, development and optimization of wind turbines (see Sørensen (2011)).

In the early stages of rotor design, all the focus were on maximizing the power coefficient, which is a measure of how efficiently the wind turbine converts the wind energy into electricity. Later studies aimed at having maximum power production for a range of wind speeds instead of having maximum power coefficient at one certain wind speed. Nowadays, the design philosophy is to minimize the cost of energy, even if it requires decreasing peak aerodynamic efficiency (see Snel (2003)).

Recent rotor aerodynamic research has focused on improving conventional design codes based on the Blade Element Momentum (BEM) method, analyzing the global flow field as well as the blade near flow field by Euler and Navier-Stokes solvers, and obtaining accurate experimental data (see Sørensen (2011)). Besides, there is a lot of effort in the application of panel methods. In the following section, some of the common approaches will be discussed from the aerodynamic design point of view.

1.1.1 Methods applied in wind turbine aerodynamics

In the present section, state-of-the-art methods for the analysis, development and design of wind turbines will be summarized shortly. In order to optimise a wind turbine, the accurate prediction of power generation and loads is necessary. For this purpose, three main methods are summarized in the aerodynamic design of a wind turbine:

- Blade Element Momentum (BEM) method

- Computational Fluid Dynamics (CFD)
- Experiments

Blade Element Momentum method

The Blade Element Momentum (BEM) method is widely used for estimating wind turbine blade performance and design analysis. This method combines the blade element theory and the momentum theory to calculate both the induced velocity distribution and the turbine blade loading. In the blade element theory, the blade is divided into a number of two dimensional (2D) spanwise strips. The force on the blades is then assumed to be distributed over annular rings. Momentum theory can then be applied on these aerodynamically independent rings. A detailed description of the BEM method is presented in Manwell et al. (2002) and Leishman (2000). Nevertheless, the basic assumptions in the traditional BEM method can be summarized as follows:

- two-dimensional flow over the blade,
- no aerodynamic interaction between 2D strips.

A consequence of these basic assumptions of the BEM method is that there is no spanwise flow as airfoil sections are assumed to behave two-dimensionally.

Efforts have been made in the past to improve the performance of the BEM calculations by incorporating engineering methods. For example, a number of solutions have been proposed for including the effect of tip vortices. The most famous one was suggested by Prandtl (see Betz (1919)). This method presents a correction factor which has to be added to the BEM equations. This correction factor is a function of the number of blades, the inflow angle, and the radial position on the blade section. In the same manner, a loss factor due to the root vortex is implemented in some BEM codes (see Moriarty and Hansen (2005)). While most of the flow features of the outboard flow region can be taken into account in these BEM models, the presence of viscous, turbulent and three-dimensional flow in the root region has still some difficulties to be modeled in BEM type codes. Hence, the present research aims to contribute to a more accurate application of the models for the root vortex.

Computational Fluid Dynamics

To overcome the uncertainties due to simplifications of the BEM method and to understand more fundamental physics of wind turbine aerodynamics, there is a need for more sophisticated approaches such as computational fluid dynamics (CFD). As it is reported in Sørensen (2011), the CFD models, based on

the solution of the Euler or Navier-Stokes equations, range from simple panel models and hybrid viscous-inviscid interactive codes to full Navier-Stokes solver tools.

Potential flow modeling One of the first applications of potential flow theory for predicting the aerodynamic properties of a finite wing was developed by Ludwig Prandtl and his colleagues.

In wind turbine applications, the rotor blades are modeled as lifting lines by superposition of a number of horse-shoe vortices. Each of them is composed of a bound vortex and two free-trailing vortices (see Figure 1.1). This method follows the basic principles of vortex behavior which is known as Helmholtz's vortex theorem (see Anderson Jr. (2001)).

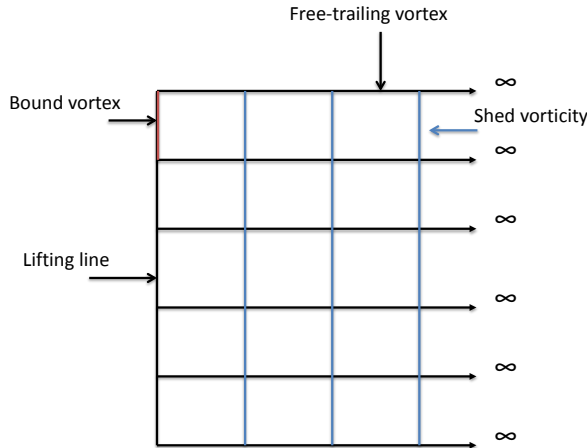


Figure 1.1: Schematic lifting line representation of a blade.

In lifting line methods, the velocity field can be deduced from the vorticity field by the Biot-Savart law. The vortex filaments are transported in the wake by the superposition of the freestream velocity and the induced velocity. These methods determine the trailing vorticity and shed vorticity by the bound circulation change along the spanwise direction, and by the temporal variations as the blade rotates, respectively (see Sørensen (2011)). Although 3D characteristics of these methods can be counted as an advantage in attached flow regions, they are based on inviscid flow equations which brings a significant disadvantage in the separated flow regions.

Panel methods have the advantage of modeling the flow over complex three-dimensional configurations. There are many different variations of panel codes. However, the general idea is to cover the three-dimensional body with panels over which there is an unknown distribution of singularities (such as point sources, doublets, or vortices). Besides modeling the blade geometry more accurately than the lifting line method, these methods enable the modelling of the nacelle and the tower of the wind turbine. A detailed explanation of panel methods can be found in Katz and Plotkin (2001).

A model based on acceleration potential theory was developed by van Bussel (1995) for the application to wind turbines. With the implementation of this model, it is possible to determine blade loads and velocity distributions in the vicinity of the blade in detail. This model can be applied for axial dynamic inflow and yaw flow conditions.

As a general remark to the potential flow models: The methods are based on potential flow solutions and therefore they are successful in solving attached flow fields. In the case of such attached flow fields, the pressure distribution and the lift, calculated by the potential flow solution, will be similar to the experimental results. But for the drag force estimation, only the lift-induced drag portion is provided by the potential flow solution and an estimation of the viscous drag is required. In the case of the flows with considerable areas of flow separations, the potential method usually can capture the areas of large pressure gradients that cause the flow separations, but the computed pressure distributions may be wrong (see Katz and Plotkin (2001)). Hence, the use of viscous-inviscid interaction methods can be applicable for these models.

Navier-stokes models The most advanced aerodynamic methods in the field of wind energy are the Navier-Stokes solvers. Previously gained experience in CFD methods from the aeronautical research has been applied to wind turbine aerodynamics. The motion of the fluids is described by the Navier-Stokes equations which do not have an analytical solution for the majority of flow problems. An estimation of the solution can be obtained by changing the set of partial differential equations into a system of algebraic equations which can be solved with a computer. In the first step of a Navier-Stokes simulation, the geometry of the flow problem under study is generated and the computational domain is formed by a number of cells. The quality of the cells, which compose the computational domain, plays an important role in the accuracy of the numerical solution. The boundary conditions also possess a significant importance in the solution. Another point which affects the accuracy of the numerical flow field simulation is the turbulence modeling of the flow field. Tur-

bulence modeling is essential in wind turbine flow simulations because of the turbulent nature of wind. The numerical simulation of turbulent flows is possible with Direct Numerical Simulation (DNS) which solves from the smallest to largest temporal and spatial scales (see Gousseau (2012)). However, such a simulation of the flow around a wind turbine blade at the relevant value of Reynolds number is not possible (see Snel (2003)). Therefore, turbulence modeling, which simplifies the flow by imitating some turbulence information in the flow, is used. Mainly, two turbulence modeling approaches are used in the numerical solution: Reynolds-Averaged Navier-Stokes (RANS) and Large-Eddy Simulation (LES). In RANS simulations, first the variables are decomposed into the mean value and the turbulent fluctuations. The flow equations are averaged and then solved in terms of the mean variables. On the other hand, in the LES simulations, a filtering method is applied to the equations. While the resulting filtered equations are solved, the effect of the scales smaller than the filter width is modeled. The numerical results shown in this thesis are obtained from RANS simulations.

Notwithstanding the advances of computational fluid dynamics, an accurate modeling of the details of the near wake and blade, in a three-dimensional viscous and turbulent flow, is still a computational challenge. Recent numerical studies have attempted to simulate full wind turbine flows by 3D Navier-Stokes computations. However, Sørensen (2011) implies the dependency of these studies on the adopted turbulence models. In spite of the potential that CFD holds, it is not feasible to employ it alone in the design phase of a wind turbine; as validation is still needed. CFD validated with experiments can however be used to attain fundamental and detailed understanding of the aerodynamic phenomena of wind turbines.

Experimental simulations and measurements

As mentioned in the previous paragraph, experiments are an inevitable step to improve the basic knowledge of wind turbine aerodynamics. It is not only necessary for the development and validation of numerical tools, but it is also needed for the direct observations of aerodynamic phenomena, especially in the complex flow fields such as the root region of a HAWT blade. The experiments, particularly for wind turbine flow field investigations, can be divided into two main test environments: (i) field tests in the natural wind environment, (ii) wind tunnel tests in controlled conditions. Field tests have the disadvantage that the flow interacting with the wind turbine is mostly unknown and stochastic. In contrast, the flow in wind tunnel tests is well defined. However, in wind tunnel tests the turbine model has usually a smaller size than

the real turbine. Thus, the flow similarity requirements cannot be met, such as Reynolds number. This limits the validity of the extrapolation of the insight obtained in the experiment to the full scale rotors.

Different measurement techniques can be applied to measure the aerodynamic loads and the flow field produced by a wind turbine blade. These methods may vary from pressure taps to advanced laser techniques. Improved measurement accuracy and detailed measurement capacity in modern techniques such as particle image velocimetry (PIV), which captures the whole field of interest, and allows the comparison and validation of numerical results with an extensive amount of accurate and detailed experimental data.

A detailed explanation of the PIV technique used in the present experimental work is given in Chapter 2, Section 2.2. In the present thesis, an extensive PIV experiment in the wind tunnel is used to study the root flow aerodynamics.

1.2 Introduction to the root flow aerodynamics of a HAWT

Although research in wind turbine aerodynamics has been conducted for a long time, HAWT blade root flow aerodynamics is one of the least known topics. Even some of the root flow features are sometimes called as the *Higgs particle* of the root flow ¹.

Less power production from the root region, as well as the complexity of the root flow field can be counted as reasons for the lack of information about the flow in the root region compared to other parts of the wind turbine blade. In the following sections, the blade wake and potential flow region and some of the root flow features along with the previous observations will be explained.

1.2.1 Blade wake region

The rotor wake, which can be anticipated as a vortex system, conveys downwind the flow structures such as the trailing vortices released from the blade. A distinct tip vortex and a less concentrated trailing vorticity in the blade root are formed in the rotor wake region. The wake region of a HAWT is typically divided into a near and a far wake. The difference between these two regions is

¹During a private communication with Andrew Garrad, he called the root vortex as Higgs particle of the root flow. Andrew Garrad is seen as one of the most influential individuals in the early wind industry, and is widely regarded in the global wind industry as the godfather of wind technology innovation.

spatial distribution and intensity of turbulence in the flow field. The far wake, which extends after the near wake, typically shows more evenly distributed turbulence and velocity profiles. The turbine-generated turbulence and velocity deficit vanish as a result of mixing and diffusion in the far wake (see Manwell et al. (2002)).

A comprehensive review of wind turbine wake studies was performed by Vermeer et al. (2003). In this review, the need for substantiating the case-dependent computations with experimental data such as NREL Unsteady Aerodynamic Experiment in the NASA-Ames wind tunnel (see Hand et al. (2001)) and the MEXICO projects (see Schepers and Snel (2007)) was highlighted.

The flow field at the blade root can be divided into the potential and viscous flow regions. The latter includes the boundary layer of the blade and the viscous wake of the blade in the wake region, while the former refers to the remaining flow field. Although this flow division helps to deal with the problems separately, the interaction between the regions should be considered as well. For example, the effects of the wake vortex system on the inflow conditions of the potential flow as well as on the boundary layer flow were indicated in the early study of Sørensen (1986). Sørensen (1986) modelled the blade flow in two regions; viscous domain, governed by the boundary layer equations, and inviscid domain, represented by the inviscid Euler equations. This model aimed to handle three dimensional flow separation in rotation.

There are experimental (e.g. Whale et al. (2000), Massouh and Dobrev (2007), Sherry et al. (2010)) and numerical (e.g. Ivanell et al. (2007)) studies which have analyzed the flow in the near wake region of the HAWT blade. The vortex wake behind a HAWT rotor obtained from experiments was analyzed in the study of Whale et al. (2000) and compared with the Rotor Vortex Lattice Method computations at different tip speed ratios. However, the results of this study have some conflicts with the present knowledge of the wind turbine root flow aerodynamics. Whale et al. (2000) showed that the root vortex system is rotating in the same direction with the tip vortex system and finally merges with the tip vortex.

The flow characteristics may change in the blade wake region based on the operating tip speed ratio, λ , and the blade geometry (see Ebert and Wood (1997, 1999, 2001) and Massouh and Dobrev (2007)). To see the effects of tip speed ratio on the blade wake development, Ebert and Wood (1997, 1999, 2001) tested three different tip speed ratios ($\lambda = 2, 4, \text{ and } 6$). Based on the experimental results, it was concluded that at the lowest λ , the blade wake was larger and there was evidence of separation due to high blade angles of attack. However, it should be noted here that the evidence of these results are not clearly proven in their research paper.

Moreover, when analyzing the velocity and vorticity distributions of a HAWT and of a propeller, some similarities are found. Cotroni et al. (2000) investigated a propeller wake by means of PIV; there it was shown that the blade wake created a velocity deficit in the axial velocity distribution and it was also noted that the spatial positions of the blade wake and of the trailing vorticity were highly correlated. The similarities between propeller and HAWT wake structures were also mentioned in the study of Ebert and Wood (1999).

In this thesis, deeper and more substantial knowledge of the wind turbine wake flow in the root region is gained with direct observations.

1.2.2 What is root flow?

The blade of a horizontal axis wind turbine (HAWT) can be divided into three regions; tip, mid and root regions, defined by the local flow characteristics. In their study, Dumitrescu and Cardos (2003) delineated the root region around $r/R \leq 0.3$ where r is the local radius and R is the radius of the rotor. However, this value may vary depending on the blade geometry and on the operating conditions. Hence, defining the limit of the root region by specific flow characteristics, like three-dimensionality and separation, may be the most accurate approach.

A schematic representation of one of the rotor models studied in the present thesis is given in Figure 1.2 as an example. For structural reasons, the blade is connected to the hub by a circular cross section region, which is not considered as an aerodynamic part. After this cylindrical part, the cross section of the blade gradually changes from circular cross section to a thick airfoil in the transition region. Note, however, that some wind turbines have an aerodynamic shape until the connection with the hub (see Figure 1.3).

In the root region, the blade geometry is different to that in the outboard region. While the choice of the thickness of the airfoil is due to structural reasons, the planform of this region is driven by aerodynamic basis. Hence, the flow characteristics in the root region differ from the flow behavior in the outboard region, primarily because of the blade geometry in the root region. Yet to date, most of the previous studies (e.g. Ferrer and Munduate (2007), Shen et al. (2005)) have focused on analyzing the characteristics of the outboard flow region. And there has been a limited interest in the study of the root region mostly because the majority of energy production is gained from the outboard region of the blade. Moreover, the flow characteristics are complex, unexplored, and the experiments are difficult to perform in the root region. This leads to an incomplete understanding of the flow field in the root region. The aim of the present work is to explore this complex flow phenomenon, and to provide a

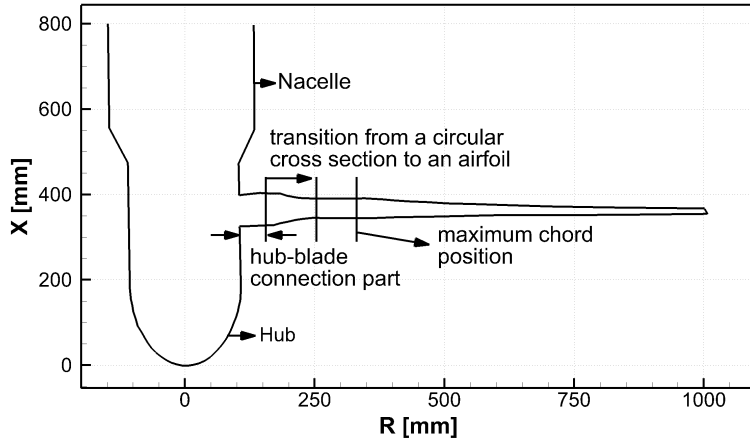


Figure 1.2: Schematic representation of the present rotor model's parts (**Blade 1**).



Figure 1.3: An example of a wind turbine blade without transition part (Enercon E 82). The figure is taken from <http://www.wind-energy-the-facts.org/large-commercial-wind-turbines.html>

better understanding of the root flow aerodynamics. The following key aspects are essential in the blade root region:

- Vorticity evolution in the blade root region.
- Possible flow separation due to large flow angles.
- The effect of trailing root vorticity on the flow near the blade.
- Large rotational effects in the thick boundary layer.
- Geometrical effects in the root region.

1.2.3 Root vortex

There are two basic optimum rotor interpretations: Joukowsky (1912) and Prandtl & Betz (1919). As explained shortly in the review by Sørensen (2011), Joukowsky (1912) affirmed that the optimum rotor which has N_b blade, creates a vortex system which consists of a N_b number of helical vortices with a strength Γ and one axial root vortex with a strength of $N_b\Gamma$ (see Figure 1.4-a). According to Prandtl & Betz (1919) the optimum rotor efficiency can be achieved if the blades create a rigid helicoidal wake which moves in the axial direction with a constant but reduced axial velocity (see Figure 1.4-b).

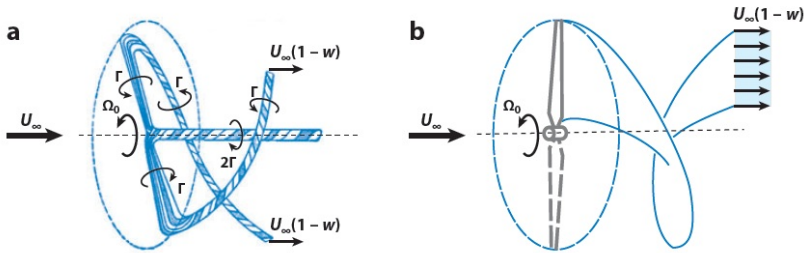


Figure 1.4: Sketch of the vortex system corresponding to lifting line theory of the ideal propeller of (a) Joukowsky and (b) Prandtl & Betz. Figure is taken from Sørensen (2011).

A HAWT blade can be represented by a lifting line by superposition of a number of horse-shoe vortices, as a variation of Prandtl's lifting line theory. Each trailing vortex on a HAWT blade has a circulation equal to the change in circulation along the span (see Anderson Jr. (2001)). Whale et al. (2000)

hypothesized that the wake deforms into a system resulting in a weak diffused trailing vortex in the inner region and an intense tip vortex spiral in the outer region. However, it is important to note that the formation and development of the trailing vorticity in the root region highly depends on the blade geometry and the operating condition of the rotor. Therefore, this hypothesis may not be true for different blade root geometries and for different operating conditions.

The vorticity in the root region has been studied numerically (e.g. Ivanell et al. (2007)) and experimentally (e.g. Ebert and Wood (2001), Whale et al. (2000), Massouh and Dobrev (2007), Sherry et al. (2010)). These studies use different definitions for the root flow features. Three terms have been used in the literature to explain the basic feature of the root flow: inner and/or inboard vorticity, hub vortex and root vortex. Whale et al. (2000) showed that the inboard vorticity had the same sign as the tip vortex. However, the horseshoe vortex interpretation demonstrates that the root and tip vortices are counter-rotating free trailing vortices. Whale et al. (2000) also explained the formation of inner vorticity as a result of high solidity of the inboard region at high tip speed ratio, λ . In contrast, in the experiment of Massouh and Dobrev (2007), who investigated the wake of a small commercial wind turbine rotor by means of PIV, the cause of the expanding inner vorticity was not related with high solidity of the inboard region.

Ebert and Wood (1997, 1999, 2001) analyzed the three velocity components and the formation of hub and tip vortices by means of hot-wire anemometry. In this study, the term hub vortex was used for the vorticity generated in the vicinity of the hub. It differs from the root vortex which emanates from the blade. The hub vortex analysis of Ebert and Wood (2001) suggested that the hub vortices merge into a single hub vortex along the axis of rotation in opposition to the experiments of Whale et al. (2000), which showed that the inner vorticity merges with the tip vortex system.

These apparently contradicting results in the analysis of the root flow features show the need of further investigation, which is the purpose of the present research. A vortex may, qualitatively, be explained as a connected fluid region with high concentration of vorticity compared to its surroundings (see Saffman and Baker (1979)).

In this thesis, the root vortex is defined where an increase in the strength of the vorticity near the root occurs over a small range of radii. This indicates the existence of a root vortex. This thesis documents direct observations in order to identify the possible presence of a root vortex with a comprehensive experimental analysis.

1.2.4 3D flow in the root region

The root flow may have three dimensional characteristics due to the root vortex, the blade rotation and the blade geometry in this region. An outboard motion of the flow was noted in the velocity measurements of Ebert and Wood (1997). Medici and Alfredsson (2006) also mentioned the expansion in the wake demonstrated by an outboard motion. However, the radial velocity in the vicinity of the nacelle was found to be in the inboard direction.

Stall delay

It was firstly observed in the famous aircraft propeller experiment of Himmelkamp (1947) that rotation has a delaying effect on the occurrence of separation. Similar to this, many other studies showed that rotational effects are the main cause of a phenomenon which is called as rotational augmentation, or more commonly, as stall delay. Later on, stall delay was also studied on wind turbine blades by Milborrow (1985) (ref. Breton et al. (2008)).

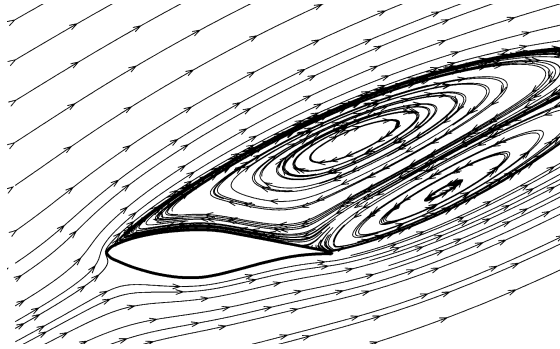
The early investigations on rotational effects did not show a significant effect on the boundary layer development in the attached flow region (see Fogarty (1951) in Ref. Sørensen (1986)). This conclusion was supported by Schreck et al. (2007): the rotational effects are more pronounced in the separated flow region than in the attached flow region.

Based on the measurements and flow visualization on a rotating blade, McCroskey [Ref. 6 in Snel et al. (1993)] notes that there is no remarkable change in the transition or separation location, but observes significant radial flow in separated flow regions, even in laminar separation bubbles.

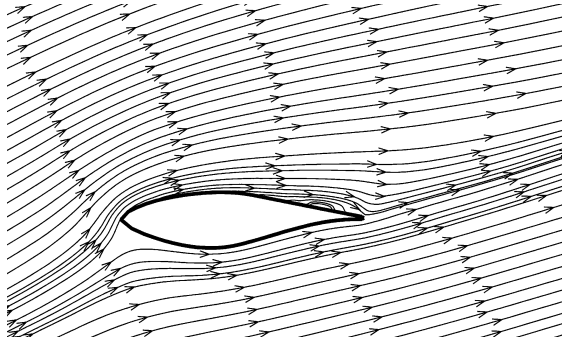
Coriolis force has the tendency to push the flow in the chordwise direction towards the trailing edge. This mechanism results in a thinner and more stable boundary layer which also moves slightly outboard. As a result of these, the formation of separation bubbles and the leading edge stall is reduced (see Lindenburg (2004)). This mechanism is the so called stall delay or rotational augmentation.

Du and Selig (2000), Dumitrescu and Cardos (2003), Hu et al. (2006) showed that the stall delay mechanism is more apparent in the blade root region where the angles of attack are high. The effects of rotation at high angle of attack can be clearly seen in the study of Hu et al. (2006) in Figure 1.5.

In their study, Schreck et al. (2007) combined surface pressure measurements with computations to obtain high-resolution boundary layer topologies and detailed flow field structures above the boundary layer. The link between the stall delay and the cohesive vortical structures in the above boundary layer



(a) 2D stationary condition, $\Omega = 0$ RPM.



(b) 3D rotating condition, $\Omega = 100$ RPM.

Figure 1.5: Streamlines at local angle of attack $\alpha = 24.588^\circ$. Figures are taken from Hu et al. (2006). The radial position is not mentioned.

flow field was emphasized.

Dumitrescu et al. (2007) performed a theoretical analysis on the boundary layer characteristics of a wind turbine blade root region by discussing the 3D and rotational effects for both attached and separated flows. It was also shown that c/r is the parameter which affects the separated flow structure. It was also shown that an energetic vortex bubble generated in the inner part of the blade may be responsible for stall delay. The deficiency of this study was found to be the inviscid flow field assumption, which did not have either full separation nor wake effects.

3D corrections

There is an increase in the blade loading due to the stall delay mechanism, appearing in rotation especially at higher angles of attack. However, this tendency in loads cannot be captured when simulating a rotating wind turbine using 2D aerodynamic data. It was already revealed that the models based on 2D airfoil data like BEM methods cannot capture the real physics in the three dimensional flow regions (see Chaviaropoulos and Hansen (2000)). Hence, there is a need for correction of the three-dimensionality of the flow on the 2D airfoil data, if methods fed by 2D airfoil data are to be used.

Different correction models have been developed to correct aerodynamic coefficients for the modelling of wind turbine loads. Breton et al. (2008) examined the performance of six 3D correction models. The results were compared with the wind tunnel data from NREL's phase VI experiment (see Hand et al. (2001)). Breton et al. (2008) showed that none of the correction models could produce the actual flow physics (see Figure 1.6). This conclusion is particularly important and shows the limitations of the 3D corrections in the BEM models as well as the need for alternative methods for the design of HAWT blades.

Wood (1991), Snel et al. (1993), and Dumitrescu et al. (2007) demonstrated that c/r is a reference parameter in the stall delay mechanism. In the work of Chaviaropoulos and Hansen (2000), besides c/r , the local twist angle of the blade section, was introduced as a triggering parameter of 3D effects. In addition to these parameters, Du and Selig (2000) mentioned two other non-dimensional parameters ($\Omega r/U$, Re) which affect the location of separation. Certainly, the validity of these suggestions can be discussed.

1.3 Formulation of the research questions

In conclusion, HAWT root flow has very complex characteristics due to three dimensionality, separation, and rotation of the blade. Without having the much more detailed knowledge of the flow behavior in the root region, it is impossible to produce accurate and reliable aerodynamic modeling of the root flow. As it is mentioned previously, various types of analysis have been performed in the root region to have a comprehensive knowledge about this region. However, there are inconsistent explanations and observations from these previous studies. This shows the need for the further analysis of the root flow which is the purpose of the present research.

The present research aims at providing very detailed velocity measurements

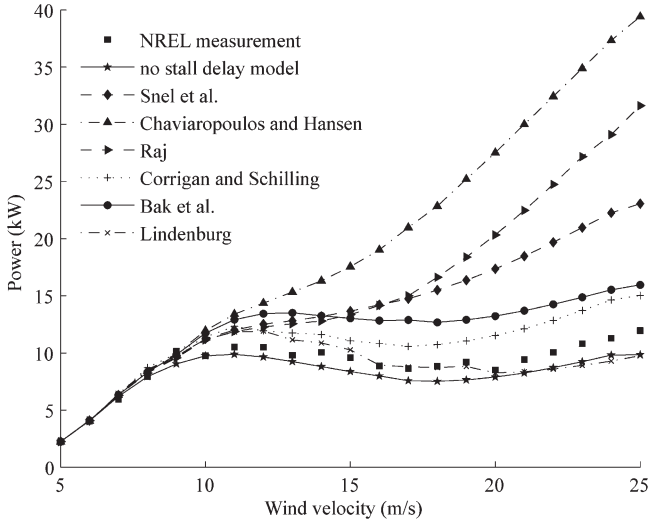


Figure 1.6: Measured power as a function of incoming wind speed compared with power predicted from a prescribed wake model (HAWTDAWG) with and without different stall delay models. Figure is taken from Breton et al. (2008).

in the root region with the help of PIV. The analysis of the results may uncover the flow properties in the blade's root region, and may show unique particularities about the flow structures in the blade root region of a HAWT. 3D flow construction in the root region may bring new knowledge of the root flow behavior.

The present thesis attempts to answer the following questions:

Phenomena:

1. How does the flow behave in the root region of a HAWT?
 - (a) Are there effects of the blade geometry and tip speed ratio on the root flow behavior?
 - (b) Can a root vortex be identified and if so how does this root vortex evolve in the near wake region?
 - (c) What is the role of this root vortex on the local blade flow?

2. Does radial flow exist in the inviscid-outer flow region of HAWT blade root?

Parameter variation:

3. How are the blade wake, root vorticity and radial flow affected by the change of blade geometry and the tip speed ratio?

Simulation:

4. How well can CFD and BEM models simulate the observed flow phenomena around the blade root?

Validation:

5. What are the sources of discrepancy between CFD, BEM and experimental results in predicting the blade aerodynamic loading?

In order to answer these research questions, an experimental approach will be followed and supported by numerical analysis. Two HAWT models will be measured in the wind tunnel under design conditions. Some off-design operating conditions will also be tested. Different blade geometries will be used in the experiments. The experiments will be simulated by BEM and CFD methods. The results obtained from different methods may be used to point out the discrepancies of the methods.

1.4 Thesis structure

In the framework of this research several experiments are performed. These experiments are tabulated in Table A.1 in Appendix A.1.

This thesis is composed of eight chapters. Some chapters of the present thesis are based on the articles written during this study.

Chapter 1 (p. 1) provides a short background to wind turbine aerodynamics and explains the main topics in the root flow aerodynamics along with the previous studies. The chapter presents the research questions driving this research.

Chapter 2 (p. 19) explains the experiments performed during this study. The applied measurement technique, HAWT models, experimental apparatus and the set-ups are presented in detail. Moreover, the post-processing of the experimental data and the measurement uncertainties are also given in this chapter.

Chapter 3 (p. 33) presents the three components of velocity and vorticity distributions in the blade near wake region in 3D and 2D representations. Additionally, the effects of the root flow features on the local pressure distribution are investigated in the blade near wake region. Moreover, the velocity and the vorticity around the blade are also analyzed in this chapter. Experimental data used in this chapter are from test 1 (Blade 1, $\lambda = 7$), which are obtained at the same operating condition but in a different experimental campaign compared to the one in the thesis of Micalef (2012).

Chapter 4 (p. 55) conducts a comparison of three test cases. Besides the comparison of velocity and vorticity distributions in the near wake region with two different blade geometries and at two tip speed ratios ($\lambda = 5$ and $\lambda = 7$), the bound circulation and the strength of the trailing vortices are also compared.

Chapter 5 (p. 69) presents the velocities induced by the root vortex obtained by using vortex line segment and volume distribution of vorticity methods. In this chapter, the inviscid outer flow spanwise velocity around the blade is also analyzed and compared with the analytical approach.

Chapter 6 (p. 85) shows the comparison between the velocity distributions around the blade obtained from experiments and computations. The aerodynamic load calculations by different methods are also given in this chapter. Moreover, the discrepancies of the methods are discussed.

Chapter 7 (p. 113) is the main conclusion of the thesis.

Appendix (p. 117) presents some details of this work such as the experimental set-up and tests.

Chapter 2

Stereoscopic particle image velocimetry experiments

In the previous chapter, the current knowledge about the HAWT blade's root flow was analyzed along with the previous studies. The need for further analysis on the root flow was revealed. And finally, the research questions that aim to fill some of the knowledge gap in this field were stated precisely.

The aim of the present chapter is to describe the experimental setup in detail. A two-bladed rotor is tested in an open jet closed circuit wind tunnel. The velocity fields around the blade and in the near wake are measured by using stereoscopic particle image velocimetry (PIV). The flow fields produced by two different blade geometries are measured at two different blade tip speed ratios.

The main advantage of using stereoscopic PIV in such experiments are having the three components (3C) of velocity information from the whole field of interest. Moreover, PIV makes it possible to approach the flow field in the root region without disturbing the flow. However, the PIV setup used in the present study does only provide the velocity information from outside of the boundary layer.

Chapter outline

- Section 2.1 gives information about the HAWT blades used in the experiments.
- Section 2.2 describes the stereoscopic particle image velocimetry (PIV)

technique.

- Section 2.3 gives information about the stereoscopic PIV equipment and the experimental set-ups.
- Section 2.4 describes the laser light reflection in the experiments and masking procedure in the PIV images.
- Section 2.5 explains the post-processing of the PIV data.
- Section 2.6 presents the uncertainty analysis performed on the PIV data. Here, uncertainty in the velocity derivatives used in vorticity and pressure calculations is also analyzed.

2.1 Wind tunnel and HAWT model

The experiments are performed at the Open Jet Facility (OJF) of the Aerospace Faculty of Delft University of Technology (TU Delft). The details of the wind tunnel are given in Appendix A.2.

The models used in the experiments two bladed horizontal axis wind turbine (HAWT) rotor models with a 1m radius. Two different blade geometries were designed to be tested in the wind tunnel. The blade planforms are presented in Figure 2.1.

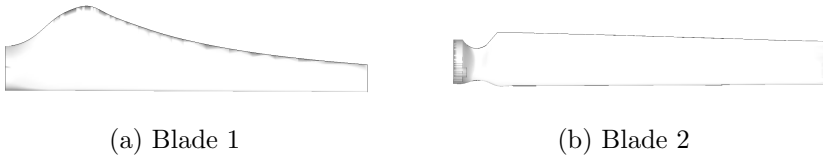


Figure 2.1: Geometrical representation of the blades used in the wind tunnel experiments.

A DU96-W-180 airfoil is used over the entire span of both blades except for the regions where the blade is connected to the hub and where the airfoil transforms to a circular cross section. A schematic representation of these regions is already shown in Figure 1.2. The chord and the twist distributions of the experimental blades along the span are presented in Figure 2.2. *Blade 1* is designed as an optimum blade with a high chord to local radius ratio (c/r) at the maximum chord position. It is known from the literature that c/r is the parameter which enhances the 3D effects at the root region of the blade. Hence,

Blade 1 has a relatively large root chord which enables to investigate the effects of taper and chord length in the root region. *Blade 2* is designed with a less pronounced c/r distribution compared to *Blade 1* (see Figure 2.2). The aim of this design is to reduce the stall delay and hence to be able to observe mostly attached unsteady flow physics.

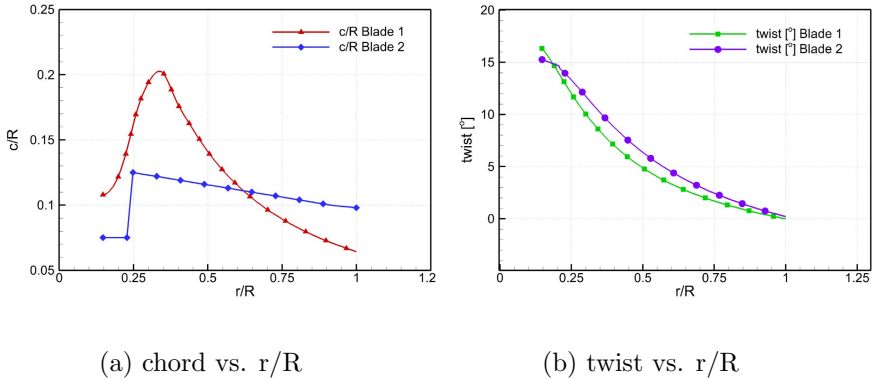


Figure 2.2: Chord and twist distributions of the two model rotor blades.

The forces (thrust and torque) are measured by the strain gauges installed in the hub. Detailed explanation of the rotor model and the force measurements are given in Appendix A.3. The strain gauges are only used to obtain the thrust and torque for three test set-ups. The measurement conditions for each test and the forces, measured during each test campaign, are summarized in Table 2.1 where λ is tip speed ratio, Ω is rotational speed, U_∞ is freestream velocity, C_T is thrust coefficient, C_P is power coefficient.

The tests are performed at two tip speed ratios to be able to analyse the performance of the rotors in design ($\lambda = 7$) and off-design conditions ($\lambda = 7$). These tip speed ratios are also covered the range of commercial rotors' operating conditions.

2.2 Stereoscopic particle image velocimetry

Particle image velocimetry (PIV) is a state-of-the-art method which allows extracting the velocity information from recorded images of large parts of flow fields. This feature is unique to the PIV technique. PIV determines the velocity

Table 2.1: Measurement conditions.

Test	Blade	yaw	λ	Ω [RPM]	U_∞ [m/s]	C_T	C_P
1	Blade 1	0°	7	400	6	0.89	0.26
2	Blade 2	0°	7	400	6	0.89	0.39
3	Blade 2	0°	5	400	8.4	0.75	0.40

of a fluid element indirectly by means of the measurement of the displacements of tracer particles within the flow, which - in most applications - have been added to the flow. In contrast to techniques for the measurement of flow velocities employing probes such as pressure tubes or hot-wires, the PIV technique, being an optical technique, works non-intrusively. This allows the application of PIV even in high-speed flows with shocks or in boundary layers close to the wall, where the flow may be disturbed by the presence of the probes (the reader is referred to Raffel et al. (2007) for complete explanation).

In Figure 2.3, a typical stereoscopic PIV setup is presented. Small tracer particles are added to the flow. A plane (light sheet) within the flow is illuminated twice by means of a laser. The tracer particles move with the local flow velocity between the two illuminations. The light scattered by the tracer particles in the camera's field of view (FOV) is recorded via a high quality lens either on a single image frame or on two separate image frames. The local displacement of the tracer particles from the first to the second illumination is determined by means of auto/cross correlation of the images captured by the camera(s). By knowing the time delay between the two illuminations and the relation between image space and real space (spatial calibration), the projection of the vector of the local flow velocity into the plane of the light sheet is calculated (see Raffel et al. (2007)).

One of the disadvantages of the classic application of PIV is the absence of the out-of-plane component of velocity. In highly three dimensional flows, this can lead to substantial measurement errors. There are a variety of approaches to obtain the three components of velocity from PIV measurements. One of them is stereoscopic PIV which uses a second camera to provide the measurement of the motion of the tracers from an additional perspective. The combination of the two perspective allows a 3C (three components of velocity in a plane) quantification of the velocity field.

The flow in the root region of a HAWT is known to have 3D characteristics, hence in the present thesis, the stereoscopic PIV technique is used to obtain the three components of velocity.

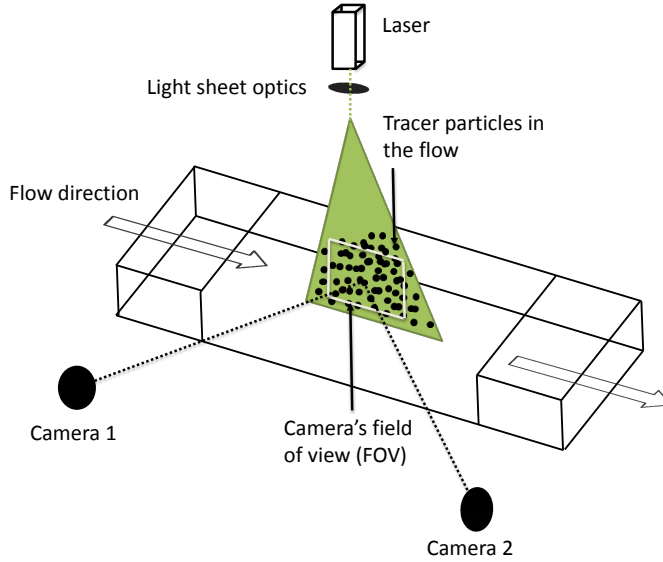


Figure 2.3: Schematic representation of stereoscopic PIV setup.

2.3 PIV measurement set-ups

Two different stereoscopic PIV set-ups, namely spanwise and chordwise measurement set-ups, are built to measure the three components of the velocity field at the blade root region of the HAWT model.

Spanwise measurements provide velocity information in the near wake region at different blade azimuth angles which enable 3D flow reconstruction. Moreover, it provides radial velocity measurements as in-plane component. Furthermore, velocity components around the blade are measured by chordwise measurements at different spanwise positions along the blade. Contrary to the spanwise measurements, in chordwise measurements spanwise velocity is measured as out-of-plane component.

More detailed explanation of PIV procedure and apparatus can be found in Appendix A.4. A picture of the PIV set-up preparation in OJF can be seen in Figure A.6.

2.3.1 Spanwise measurement set-up

The spanwise measurement configuration is presented in Figure 2.4. Contrarily to the common PIV measurement procedure where the measurement plane is typically moved through a scanning device, in this study, the laser sheet is kept at the same location and the measurements are performed at different blade azimuth angles. The azimuth angle is assumed to be $\Theta = 0^\circ$ when the blade is at the 3 o'clock position when looking from upwind to downwind direction (see Figure 2.5-a) and rotation of the blade is positive in the clockwise direction. Measurements are performed from $\Theta = -45^\circ$ to $\Theta = 90^\circ$ azimuth angles at every 5° on measurement planes with three components of velocity. Hence, the measurements at different azimuth angles allow constructing the entire 3D flow field, by assuming the flow is axisymmetric.

In order to investigate the full near wake of the rotor with sufficient resolution, the measurement area is divided into a number of field of views (FOVs), ensuring an overlap between every two FOVs (see Figure 2.5-b). The cameras and the laser are fixed on a computerized traverse system so that they move together (see Figure 2.4). Therefore, it is not necessary to repeat calibration at each FOV position. The synchronization between the laser pulses and the position of the rotating blade is achieved with a triggering system in the hub. The PIV system parameters for spanwise measurements are summarized in Table A.3 in Appendix A.4.

2.3.2 Chordwise measurement set-up

The chordwise measurement configuration is presented in Figure 2.6. In this set-up, contrarily to the spanwise measurement set-up, during the measurements the blade is captured at the same position but the laser sheet and the cameras are moved along the blade span. The measurements are performed when the blade is at $\Theta = 0^\circ$ azimuth angle, in other words where the blade is at the 3 o'clock position when looking from upwind to downwind direction (see Figure 2.5-a).

With the available PIV system used in the present study, it is impossible to visualize the whole blade cross section at one laser illumination. This is because when the laser is shot from one side of the blade, the other side of the blade is obscured by the blade's shadow and the blade itself (see Figure 2.7). To be able to measure all around the blade cross section, pressure and suction sides are measured independently. After post-processing the two measurements separately, they are stitched to each other based on a correlation method on the overlapped region. The measurements are performed at 30 different radial

locations along the blade span.

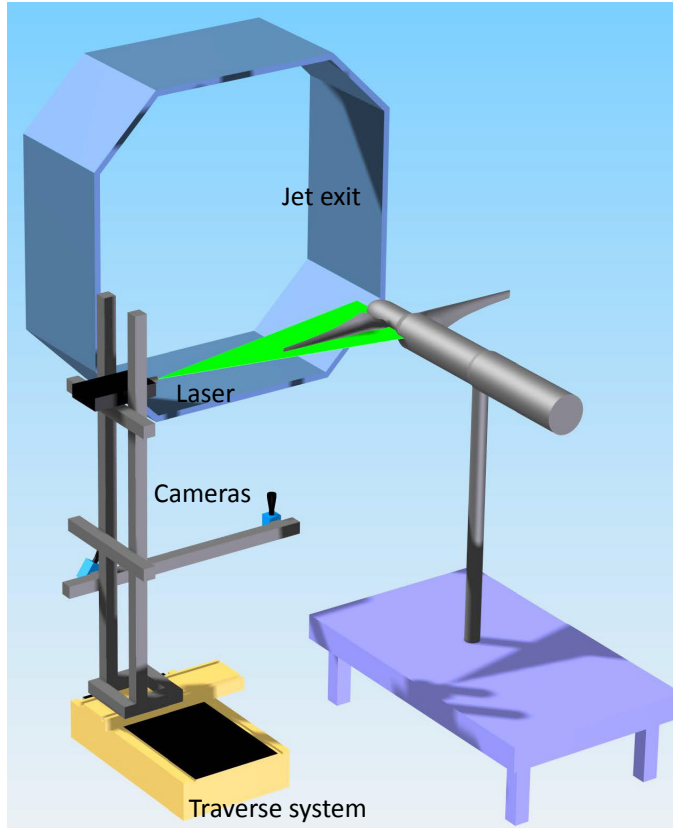


Figure 2.4: Schematic representation of the spanwise measurement set-up in the OJF.

2.4 Laser light reflection

Reflection is a problem arising during the PIV measurements which must be treated for the correct and complete measurement. The signals obtained from the area contaminated by the reflections are corrupted. Hence, the information near areas of reflection may not be realistic. In order to avoid laser light

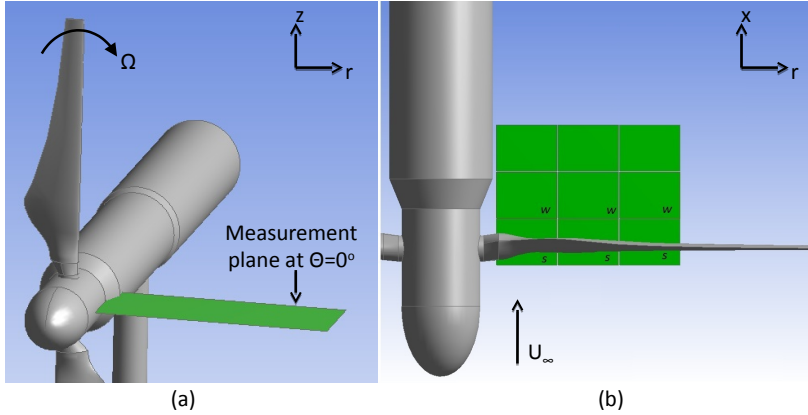


Figure 2.5: (a) Measurement plane location at $\Theta = 0^\circ$ (reference angle). (b) Combined fields of views (FOVs) in the blade flow, the "s" panels, and in the near wake, the "w" panels.

reflection from the blade surface, some model treatments are performed in the present PIV experiments. First, the measurement blade is painted with matte black paint to absorb the incident light. The next approach is painting the blade with rhodamine. Rhodamine is a fluorescent dye, absorbing light with the wavelength of the laser light and reflecting the light which has a wavelength different from the absorbed one.

In the present experiments, reflection is the major problem in the blade root region due to the more rounded geometry of the blade. There are some regions especially in the leading edge of the blade where the reflections are unavoidable.

Masking

In order to obtain the best spatial resolution, the experimental setup should be arranged in a way that the complete image can be used for vector calculation. However, this is not always possible due to the experimental conditions. Sometimes, the image includes the body or includes the laser light reflections. The regions, where the information is obscured by these effects, are masked. No evaluation is performed in the masked region where the intensity is zero (see LaVision Product Manual (2009)).

In the present study, the regions where the image is obscured by the blade

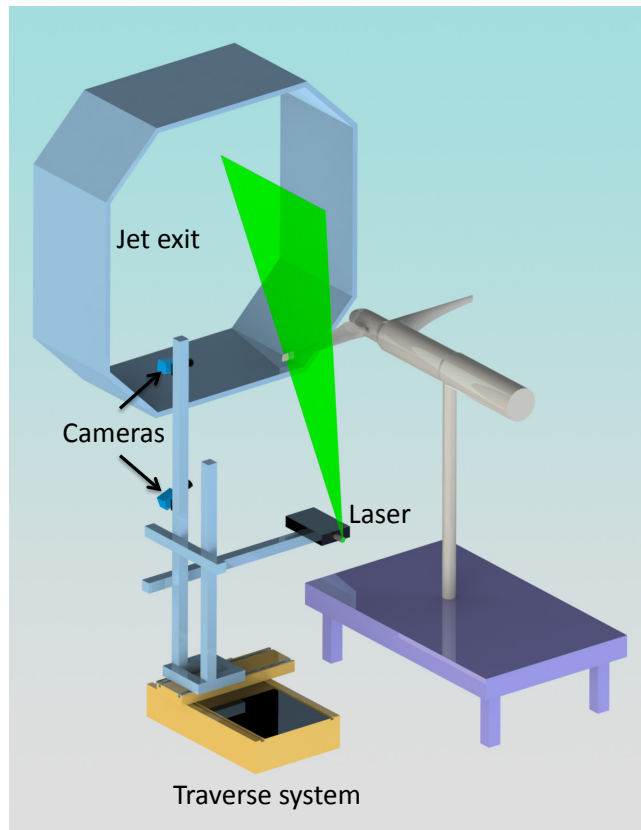


Figure 2.6: Schematic representation of the chordwise measurement set-up in the OJF.

and its shadow and/or by the laser light reflection are masked during the post-processing of the PIV data.

2.5 Post processing of PIV data

After post-processing the PIV velocity fields, the phase-locked average velocity and the velocity RMS (root mean square) vector fields are obtained. The average velocity fields contain three components of absolute velocity. Velocity

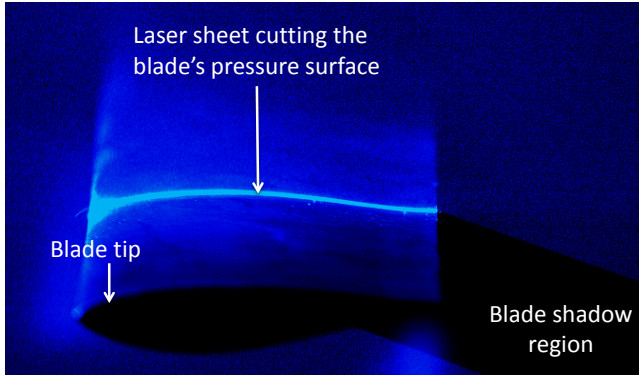


Figure 2.7: An example of PIV image for pressure side measurement.

RMS values are calculated according to Equation A.1, in Appendix A.4.1.

For the spanwise measurements, the flow properties are evaluated in cylindrical frame of reference with axial, radial and azimuthal velocity components (V_x , V_r , V_θ respectively). After constructing the 3D volume distribution of velocity from 2D measurement planes with three components of velocity (see Figure 2.8 as an example), the vorticity in cylindrical coordinates is calculated (see Appendix A.4.1 for the vorticity formulation in cylindrical coordinates).

The flow properties in the chordwise measurements are evaluated with axial, spanwise and tangential velocity components (V_x , V_y , V_z respectively).

2.6 Measurement uncertainty

The stereoscopic PIV measurement system consists of several sub-systems. The overall accuracy in PIV measurements may depend upon aspects ranging from the recording process to the methods of evaluation. The accuracy of the velocity related quantities, such as vorticity, strongly depends on the quality of the PIV velocity measurements, and on the methods of data evaluation.

2.6.1 Experimental uncertainties

The uncertainty due to design of the experiment is difficult to estimate. Source of uncertainties may vary from the instrumentation of the set-up to experiment-
alists. Some of the experimental uncertainty's sources can be listed as follows:

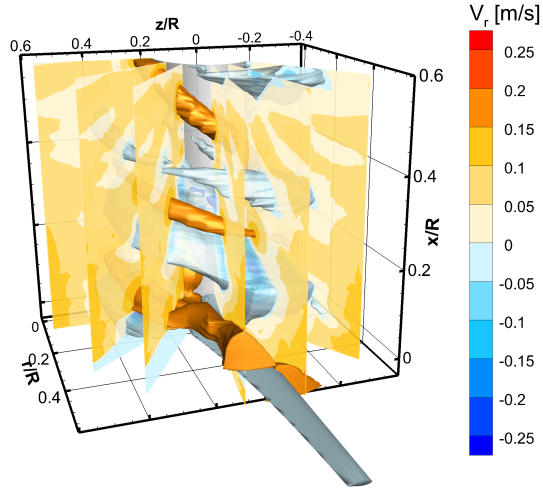


Figure 2.8: Measured radial velocity fields at some blade azimuth angles with iso-surfaces at $V_r = 0.15, 0,$ and -0.2 .

1. blade pitch angle setting,
2. rotation of the calibration plate in the PIV measurements,
3. movement of the traverse system,
4. freestream velocity of the wind tunnel,
5. rotational velocity of the rotor.

Blade pitch angle

The nominal setting angle of the blades is set to $\theta_{p,0} = 0^\circ$ at the tip. However, it is noted that the procedure to set the pitch angle of the blade does not allow for accuracies smaller than $\pm 0.5^\circ$.

Other sources of experimental uncertainty

An uncertainty in the movement of the traverse system may cause a shift in the measurements. The accuracy of the traverse system was tested and found to be in between 0.01mm-0.03mm (see Bernardy (2013)).

It was observed that the uncertainty of the rotational speed amount 0.25% of the rotational speed ($\Omega = 400RPM$) during the experiments.

2.6.2 Uncertainty in the PIV velocity fields

Absolute measurement errors in PIV velocity measurements contain systematic and residual errors. The systematic error occurs due to lack of the cross-correlation in the post-processing of a PIV recording. For the cross-correlation uncertainty, a typical value of 0.1 pixel standard error is expected (see Westerweel (1993)). The systematic errors can be removed/minimized by choosing different analysis methods. However, residual errors remain as a measurement error and sometimes it is difficult to separate it from systematic errors (see Raffel et al. (2007)). Hence the absolute measurement error is expressed with bias and random or measurement error (see Equation 2.1).

$$\epsilon_{tot} = \epsilon_{bias} \pm \epsilon_{rms} \quad (2.1)$$

Relevant bias error components are typically displacement bias error (peak locking), spatial resolution and image stitching, which are explained below.

When the particle images become too small (less than 3 pixel, see Westerweel (1998)), the displacements of the particles tend to be biased towards integral values. This systematic error is called peak locking. The error due to peak-locking (PL) is quantified by statistical analysis on the histograms of the round-off values of velocities in the spanwise measurements of the present study. Assuming a linear weight between a totally peak-locked distribution (0.5 pixel maximum error) and a Gaussian uniform distribution (0 pixel error), the value corresponding to the measurement velocity histograms can be estimated. Therefore, the RMS of the maximum and average error due to peak-locking in the axial direction is estimated to be 0.1 pixel and 0.06 pixel respectively corresponding to maximum 0.076 m/s.

Another most relevant systematic source of uncertainty in the present investigation is the spatial resolution. It is rather difficult to estimate the error due to the finite spatial resolution, which depends on the measurement location and on the ratio between the size of the structures to be resolved and the selected window size. The stability and resolution of iterative PIV image analysis with spatial filtering methods were investigated theoretically by Schrijer and Scarano (2008). By using the method explained in their study, given the window size used in the post-processing of the PIV velocity fields, the minimum size of the structures ($\lambda/2$) is 1.44 mm, which can be measured with an uncertainty corresponding to less than 10%.

Image stitching is applied to produce the complete velocity fields from separate velocity measurements. The uncertainty in this procedure is estimated as 1 pixel (see Ragni (2012)).

The velocity fluctuations, the particle image density, and background noise can be counted as sources of measurement uncertainty. For N statistically independent images, where N is the number of velocity field acquired, the uncertainty in the mean velocity can be determined with the turbulence intensity (TI) and coefficient of confidence ($z_{\alpha/2}$) as follows (see Bruun (1995)):

$$\varepsilon_{\mu} = \frac{TI}{\sqrt{N}} z_{\alpha/2} \quad (2.2)$$

The turbulence intensity of OJF in the axial direction is measured below 1%. However, due to flow non-uniformity in the test room, the flow in the vicinity of the blade may have a higher turbulence intensity. Hence, the turbulence intensity in the blade flow is assumed to be 10% which is a typical value for a conservative uncertainty estimation (see Ragni (2012)). The uncertainty in the mean velocity value due to turbulence can be estimated as 0.38% of freestream velocity of $U_{\infty} = 6$ m/s.

The uncertainty in the velocity fluctuations, which is a component of measurement error, can be calculated as:

$$\varepsilon_{\sigma} = \frac{\sigma}{\sqrt{N}} z_{\alpha/2} \quad (2.3)$$

where the numerator is the standard deviation. This uncertainty is primarily due to the fluctuations in the velocity measured as e.g., $\sigma_x: u_{rms} = \sqrt{u'^2}$, where u' is the velocity fluctuation and the overbar indicates phase-locked (ensemble) averaging.

The velocity fluctuations, as evaluated from the RMS in the acquired planes, depend upon the measurement location in the field. The measured fluctuations in the averaged axial velocity field at a location in the upstream correspond to $\sigma_x = 0.08$ m/s, which is the 1.3% of the freestream velocity of $U_{\infty} = 6$ m/s.

Typical uncertainty in the velocity fluctuations in axial direction amounts to $\varepsilon_{\sigma,x} = \pm 0.01$ m/s at an upstream location, reaches $\varepsilon_{\sigma,x} = \pm 0.1$ m/s at around $x/R = 0.5$ in the rotor wake.

The fluctuations due to the jitter of the timing pixel correspond to $\varepsilon_t = \pm 0.02$ pix in the raw images, or to ± 0.0174 m/s at the tip.

A summary of the uncertainties in the spanwise PIV velocity fields are summarized in Table A.4 in Appendix A.4.2.

2.6.3 Uncertainty in the vorticity and in the pressure from PIV

In the vortical region, the pressure is integrated from the three dimensional momentum equation by a Poisson algorithm with a second order differentiation of the pressure as already applied in Ragni et al. (2011). Detailed information about the pressure calculation will be given in Chapter 6. As for the computation of the vorticity, the evaluation of the pressure gradient requires indication of the uncertainty in the velocity derivatives. The flow pressure is computed from the flow velocity and from the velocity derivatives by use of the Navier-Stokes momentum equations. As Lourenco and Krothapalli (1995) mentioned in their study, which proposes an algorithm to minimize the error in the estimation of vorticity using the velocity fields obtained from PIV measurements, the out-of-plane component of the vorticity consists of the velocity derivatives with a suitable finite difference scheme (see Equation 2.4 with a second order scheme).

$$\left(\frac{\partial v}{\partial x} - \frac{\partial u}{\partial y}\right)_{x,y} = \left(\frac{v_{i+1} - v_{i-1}}{2\Delta x} + \Delta x^2 \mathfrak{R} + \frac{\varepsilon}{\Delta x}\right) - \left(\frac{u_{i+1} - u_{i-1}}{2\Delta y} + \Delta y^2 \mathfrak{R} + \frac{\varepsilon}{\Delta y}\right) \quad (2.4)$$

where \mathfrak{R} represents the higher order terms. Once a second order scheme is used, the error in the evaluation of the derivatives consists of a truncation error, Δx^2 , Δy^2 , Δz^2 and an uncertainty in the velocity measurement of order $(1/\Delta x, 1/\Delta y, 1/\Delta z)$ (see Equation 2.4). Coherent with this formulation, the uncertainty on the computed Bernoulli pressure is related to the error on the velocity, while the uncertainty in the integrated pressure depends upon the integration procedure.

The truncation errors and the uncertainty in the velocity measurement that the velocity gradients include are calculated for an upstream position of a PIV velocity field in the axial, radial and azimuthal directions and given in Table A.5 in Appendix A.4.2. Although the truncation error goes down with the smaller spacing and a better estimation of vorticity is expected, the error coming from the velocity measurements is affected contrarily with a smaller spacing as it is also mentioned in Lourenco and Krothapalli (1995).

Chapter 3

Experimental investigation of the root flow in a HAWT

This chapter is based on the published journal paper:

*Experimental investigation of the root flow in a Horizontal Axis Wind Turbine
B. Akay, D. Ragni, C.J. Simão Ferreira and G.J.W. van Bussel
Wind Energy, John Wiley & Sons, Ltd. (2013)*

Detailed information about the experimental set-up and procedure used in this research was given in Chapter 2. The results obtained from Test 1 (see Table 2.1 for the measurement conditions) are presented in this chapter.

HAWT root flow has very complex characteristics due to three-dimensionality, separation, and blade rotation. Without having complete knowledge of the flow in the root region, it is impossible to retrieve accurate and reliable aerodynamic modeling of the root flow. Various types of analysis/modeling have been performed in the root region to understand stall delay mechanisms (e.g. Schreck et al. (2007)), to correct the 2D airfoil data for 3D flow (e.g. Snel et al. (1993)), to limit the secondary flows by using boundary layer fences (e.g. Heinzelmann et al. (2008)), to simulate the flow-field produced by a HAWT blade by CFD

(e.g. Sørensen et al. (2011)). However, there is a lack of detailed experimental data and data analysis to provide understanding of the global flow behavior in the root region.

In the present chapter, we aim to demonstrate the existence of a root vortex and the role of root vorticity on the local blade flow. Hence, this chapter aims to answer the following questions: (i) How does the flow behave in the root region of a HAWT? (ii) How does the root vortex evolve in the blade root flow? (iii) How does the radial flow enhance in the near wake of a HAWT blade root?

The evolution of the vortices conveyed downstream by the local velocity are analyzed through vorticity and pressure distributions. The 3D pressure field is evaluated from the velocity field by use of the Navier-Stokes momentum equation to determine the local effects of the root vortex on the pressure distribution.

Chapter outline

- Section 3.1 presents the three components of velocity distributions in the blade near wake region in 2D and 3D forms.
- Section 3.2 presents vorticity distributions computed by using the PIV velocity fields in 2D and 3D forms. In this section, the evolution of the root vortex and separation are discussed.
- Section 3.3 presents pressure distributions computed by using the PIV velocity fields in 2D and 3D forms.
- Section 3.4 gives the key results of this chapter and the main conclusions.

3.1 Velocity distributions in the root region

In this section, the velocity fields obtained from stereoscopic PIV measurements are investigated at different blade azimuth angles. The phase-locked average velocities are combined to produce a three-dimensional (3D) velocity distribution. A visualization of a 3D velocity distribution, obtained by PIV measurements, can be seen in Figure 3.1. In a later stage, velocity distributions are analyzed in four azimuth angles on 2D planes (see Figures 3.2, 3.3, 3.4). The 3D radial velocity distribution (see Figure 3.1) shows outboard flow around the blade and mainly an inboard flow just behind the blade, and the whole system is wrapped around the nacelle.

To analyze the velocity distribution in the near wake region of the blade in more detail, the phase-locked average velocities at four azimuth angles of

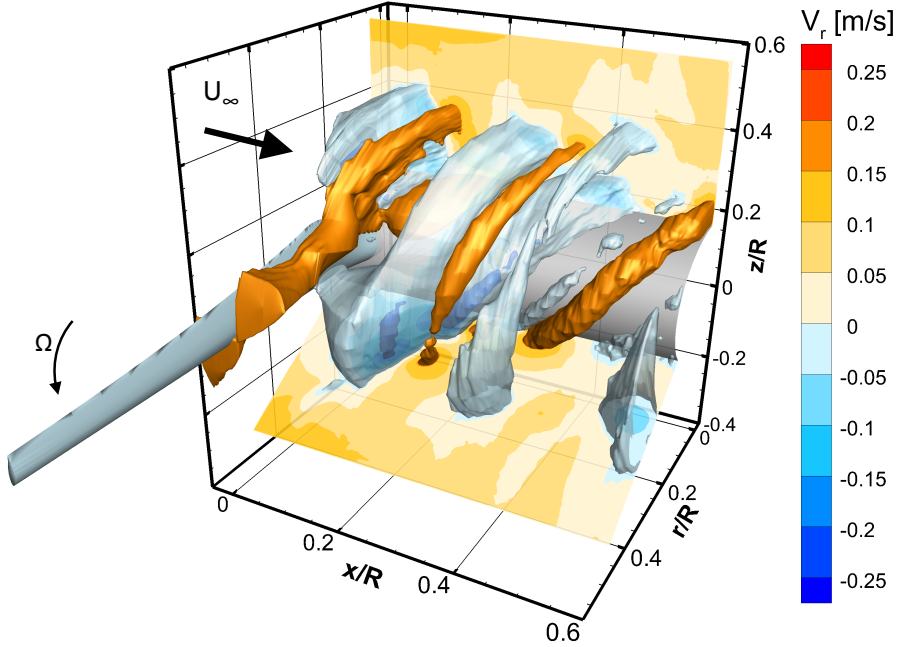


Figure 3.1: 3D visualization of radial velocity from stereoscopic PIV measurements. Iso-surfaces at $V_r = 0.15, 0$, and -0.2 .

the nine measured field of views (FOVs) are presented in 2D contour plot in Figures 3.2, 3.3, 3.4. The position of the measured fields with respect to the rotor can be seen in Figure 2.5. Three components of velocity distributions before, at and after the blade passage provide information about the flow evolution in the near wake of the blade. The connections between the different FOVs are visualized by dashed lines on the contour plots. In the present representations, the coordinate system used in the figures has a positive axial flow (in the freestream direction) upward directed $+x/R$, a positive radial flow moving from the blade root to the blade tip $+r/R$, and a positive azimuthal flow represented by the out-of-paper direction. The velocity distributions presented

here are non-dimensionalized by the freestream velocity of $U_\infty = 6$ m/s.

3.1.1 Axial velocity in the near wake region

Figure 3.2 presents axial velocity distributions around the blade and in the near wake region at four blade azimuth angles. The axial velocities in the blade wake are varying between $0.5 \times U_\infty$ and U_∞ . High axial velocities are observed in the inboard region (up to $r/R = 0.35$). At azimuth angles $\Theta = -30^\circ$ and $\Theta = 0^\circ$ along the nacelle the velocity values approach U_∞ which is significantly above the expected axial velocities based on the momentum theory. Similar velocity increase was also observed in the study of Sherry et al. (2013) and explained that it is due to the flow interaction with the nacelle. However, the axial velocities beyond $r/R = 0.35$ are as expected. There is also velocity increase observed just behind the blade at $\Theta = 0^\circ$. The reason behind this velocity increase is the upward movement of the flow in the front of the blade leading edge which creates lift over the blade. Another reason is the displacement due to the thickness of the blade.

The negative velocity observed on the pressure surface of the blade at $\Theta = 0^\circ$ can be explained with the *displacement effect* which was already shown in the work done by Mast et al. (2004). This explanation is also supported with a significant increase in axial velocity (dark red) on the suction side which is consistent with the negative velocity (blue) on the pressure side. Hence, this flow motion on the pressure side can also be explained with an upward movement of the flow caused by the blade. However, it has to be noted that the negative velocity on the pressure side may also be due to the complex geometry of the blade and due to the laser light reflections from the blade surface. This may also cause unrealistic velocities in the vicinity of the blade.

3.1.2 Azimuthal velocity in the near wake region

Figure 3.3 presents the azimuthal velocity distributions around the blade and in the near wake region at four blade azimuth angles. The overall azimuthal velocity distribution in the near wake is positive. This flow behavior is in agreement with momentum theory which says that the inviscid part of the wake rotates opposite to the blade rotation. (Note that blade moves into the paper.) In Figure 3.3-b, the local effects of the presence of the blade on the azimuthal velocity distribution are clearly visible. At the pressure side of the blade (windward side), negative azimuthal velocities, which are in the same direction with the blade rotation, are measured. This is the local effect of the blade sections (airfoil) which create higher velocity on the suction side and

lower (negative) velocity on the pressure side. This can be clearly seen in Figure 3.5. In contrast, higher positive azimuthal velocities are observed just behind the blade (leeward side). The increase of the azimuthal velocity with the blade radius is due to the increase of the lift from root to tip of the blade.

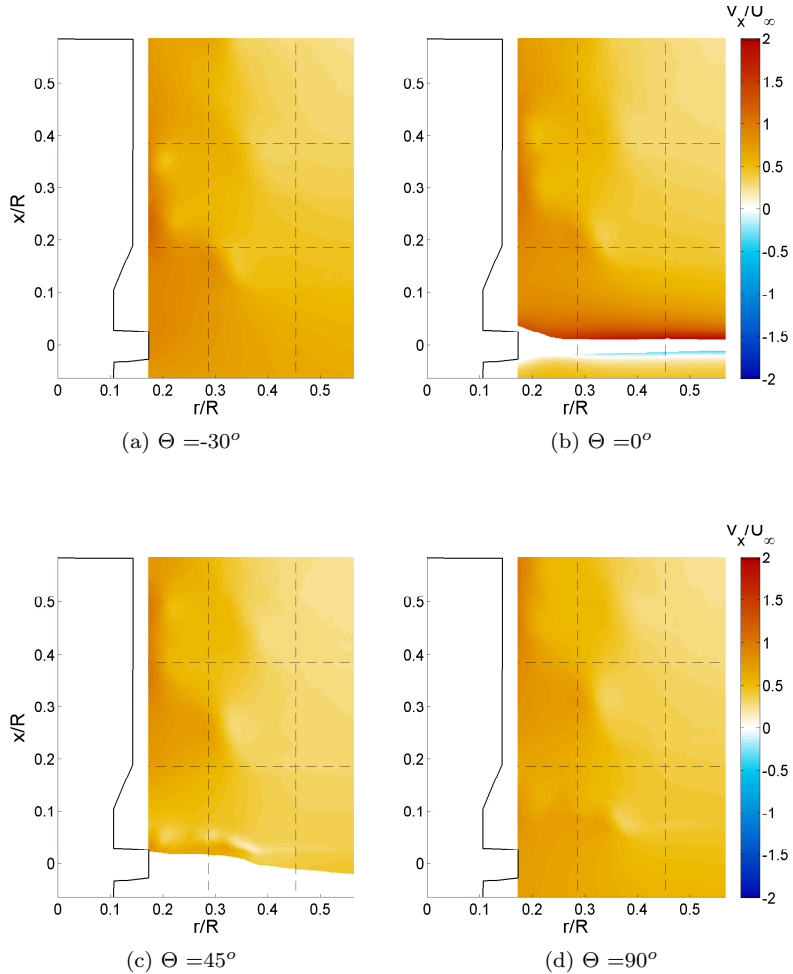


Figure 3.2: Dimensionless axial velocity distributions at four blade azimuth angles from stereoscopic PIV measurements. Inflow is in $+x/R$ direction.

Another important observation from the azimuthal velocity distributions (see Figure 3.3) is the zero or negative azimuthal velocity stripes at some wake positions, e.g., at $\Theta = -30^\circ$ at $x/R = 0.1$ and $x/R = 0.3$, at $\Theta = 45^\circ$ at $x/R = 0.05$, $x/R = 0.2$ and $x/R = 0.35$, and finally at $\Theta = 90^\circ$ at $x/R = 0.08$, $x/R = 0.25$ and $x/R = 0.38$. These velocity stripes are the “scars” of the current and of the previous blade wakes. Boundary layer material is shed from the blade into the wake area and since this flow is dragged by the blade, it has obtained a negative azimuthal velocity component. As can be seen this negative azimuthal velocity is most prominent directly after the passage of the blade and smoothens out further downstream in the wake region. Moreover, these negative velocity stripes visualize the position of the vortex sheets which will be discussed later in more detail.

The marks of the vortex sheets, observed in the azimuthal velocity distributions (see Figure 3.3), have an inner limits of extent which are clearly visible as blobs. For example, in Figure 3.3-d, the first blob in the inner edge of the vortex sheet is positioned at $x/R = 0.12$ and $r/R = 0.3$, the second blob is at $x/R = 0.34$ and $r/R = 0.32$, and the third one, which seems blurred in the image, is at $x/R = 0.46$ and $r/R = 0.36$. When the locations of these blobs are followed, the axial and the radial displacements of the blobs are clearly visible. The conveying of the wake sheets in the downstream with the axial velocity is also observed from Figure 3.3-a to Figure 3.3-d. Moreover, the position of these blobs mark the position of what can be defined as the “*root vortex*”.

3.1.3 Radial velocity in the near wake region

Figure 3.4 presents the radial velocity distributions at four blade azimuth angles around the blade and in the near wake region. In this figure, the locations of the root vortex, which were mentioned previously in the azimuthal velocity distribution, become visible as regions / spots where the radial velocity changes sign. On top of that, there are also other regions (at $r/R = 0.18 - 0.20$) where the radial velocity changes sign. In the flow region along the nacelle, where the flow is accelerated in the axial direction, there is another strong vortex (as already observed in Figure 3.2). This vortex seems to be wrapped around the nacelle in a helical fashion, a behavior which was already remarked in Figure 3.1.

In Figure 3.4, at $\Theta = 0^\circ$, a weak outboard motion is observed from $r/R = 0.18$ up to $r/R = 0.25$ which extends in the axial direction up to $x/R = 0.2$. Contrarily, in the range $r/R = 0.25 - 0.35$, corresponding around the maximum blade chord position ($r/R \cong 0.3$), the flow motion is directed inboard. Further outboard the expected wake expansion behind the rotor plane is substantiated

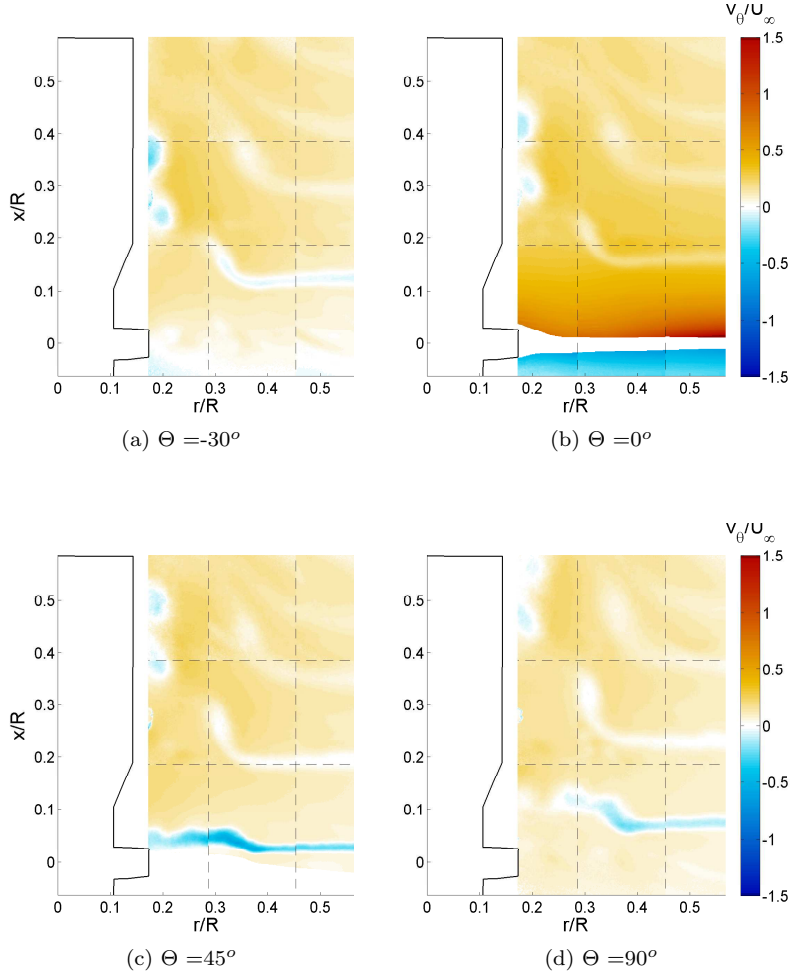


Figure 3.3: Dimensionless azimuthal velocity distributions at four blade azimuth angles from stereoscopic PIV measurements. Inflow is in $+x/R$ direction.

by the outboard motion of the wake beyond $r/R = 0.4$ in Figure 3.4.

It is also noticed that the region where the radial flow has a layer of minus and plus velocity distributions just behind the blade in Figure 3.4-c coincides with the inboard delineation of the blade wake sheet, which was already ob-

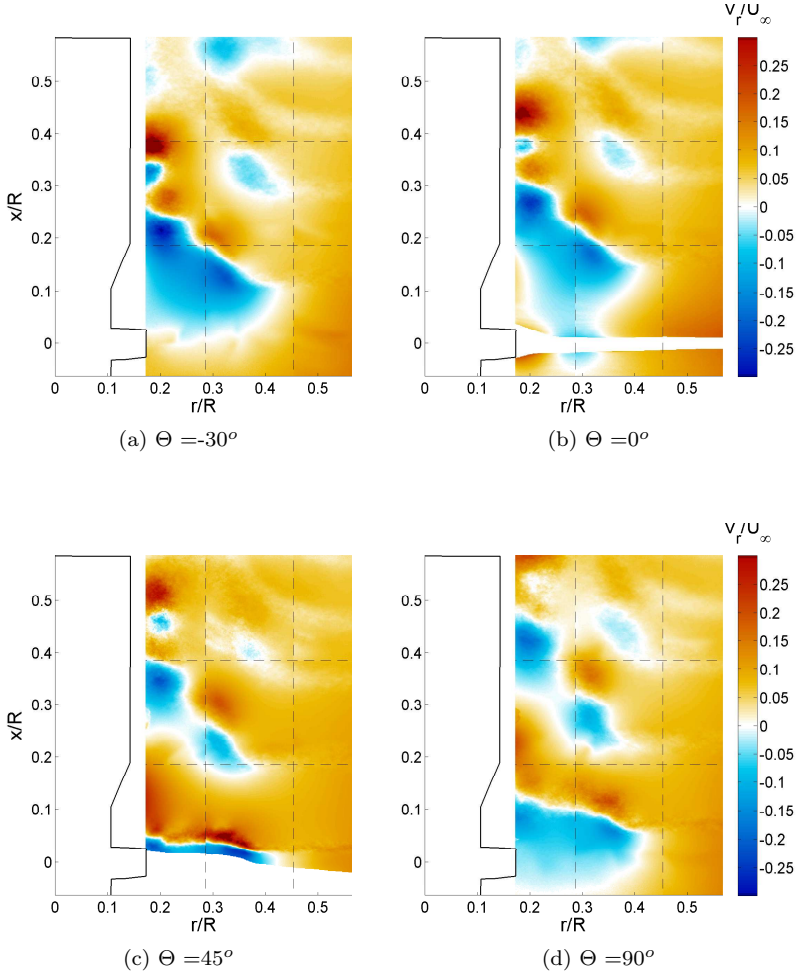


Figure 3.4: Dimensionless radial velocity distributions at four blade azimuth angles from stereoscopic PIV measurements. Inflow is in $+x/R$ direction.

served in Figure 3.3-c with negative azimuthal velocity at $x/R = 0.05$. Minus and plus radial velocity distributions (see Figure 3.4-c) can be due to the induced effect of the trailing vorticity in the root region.

3.1.4 Tangential velocity around the blade

Dimensionless tangential velocity distributions at four radial positions from chordwise PIV measurements are presented in Figure 3.5.

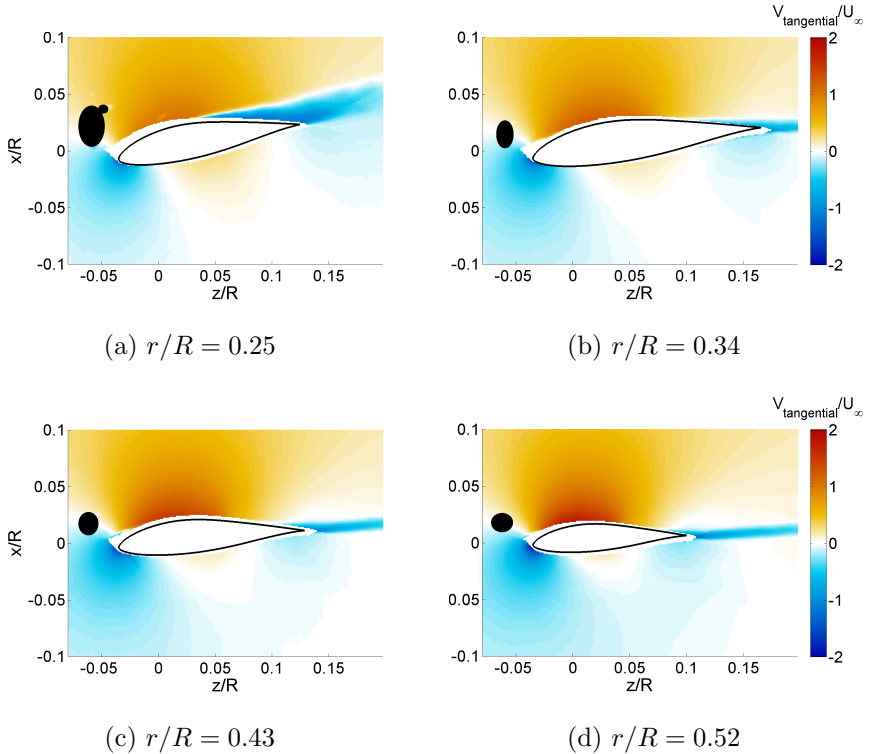


Figure 3.5: Dimensionless tangential velocity distributions at four radial positions from root (a) $r/R = 0.25$ to mid-board (d) $r/R = 0.52$, from stereoscopic PIV measurements in chordwise direction. Inflow is in $+x/R$ direction. Note that the data at $z/R = -0.05$ and $x/R = 0.025$ was masked due to reflection.

The velocity information in the regions around $z/R = -0.05$ and $x/R = 0.025$ positions are corrupted by the laser light reflections. Masking is applied in those regions which is visible as black spots having no velocity information. First of all, it is noted that the tangential velocities around the airfoil are of the same magnitude with the freestream velocity at every radial location

presented here. And the tangential velocity at the suction side is increasing from root to mid-span which is because of the increase in lift. The considerable magnitude of tangential velocities around the airfoil at radial positions $r/R = 0.25$ and $r/R = 0.34$ can be the manifestation of the high circulation in the root region. Furthermore, the reverse flow regions near the stagnation point and the boundary layer material detaches from the trailing edge are clearly visible in these tangential velocity distributions at all radial positions.

3.2 Vorticity distributions

3.2.1 3D vorticity in the root region

Vorticity is derived from the combination of the planar velocity fields as already explained in Appendix A.4.1. Vorticity as represented here is non-dimensionalized by the maximum chord and the freestream velocity. Figure 3.6 presents the three-dimensional visualization of the vorticity magnitude. Figure 3.6 b-c are different views of the situation depicted in Figure 3.6-a. The existence of the root vortex can clearly be seen in this figure. Two strong vortex tubes created in the previous and in the present blade passages are observed. These vortex tubes are released from the maximum chord position ($c_{max} : c/R \cong 0.2$ at $r/R \cong 0.3$) of the blade. Other relatively smaller vortical structures are visible close to the nacelle, corresponding to the vortices released from the hub-blade connection part (between $r/R \cong 0.11$ and $r/R \cong 0.15$) and from the circular cross section of the blade (between $r/R \cong 0.15$ and $r/R \cong 0.2$). Unlike the vortices released from the inner part of the blade root (hub-blade connection part and circular cross section of the blade: from $r/R \cong 0.11$ to $r/R \cong 0.2$), root vortex released from c_{max} does not show an interaction with the nacelle. To obtain a better understanding of the vorticity distribution in the root region, the vorticity will be decomposed into components in azimuthal, axial and radial directions.

Equation 3.1 presents the Helmholtz vorticity equation for an incompressible homogenous flow (see Morton (1984)):

$$\frac{\partial \omega}{\partial t} = (\omega \cdot \nabla) \mathbf{v} - (\mathbf{v} \cdot \nabla) \omega + \nu \nabla^2 \omega \quad (3.1)$$

where the first two terms on the right hand side express the vorticity amplification due to stretching/squeezing and tilting of vortex tubes, the last term represents the spread of vorticity due to viscosity. A physical interpretation of Equation 3.1 can be obtained looking to the vorticity distributions around

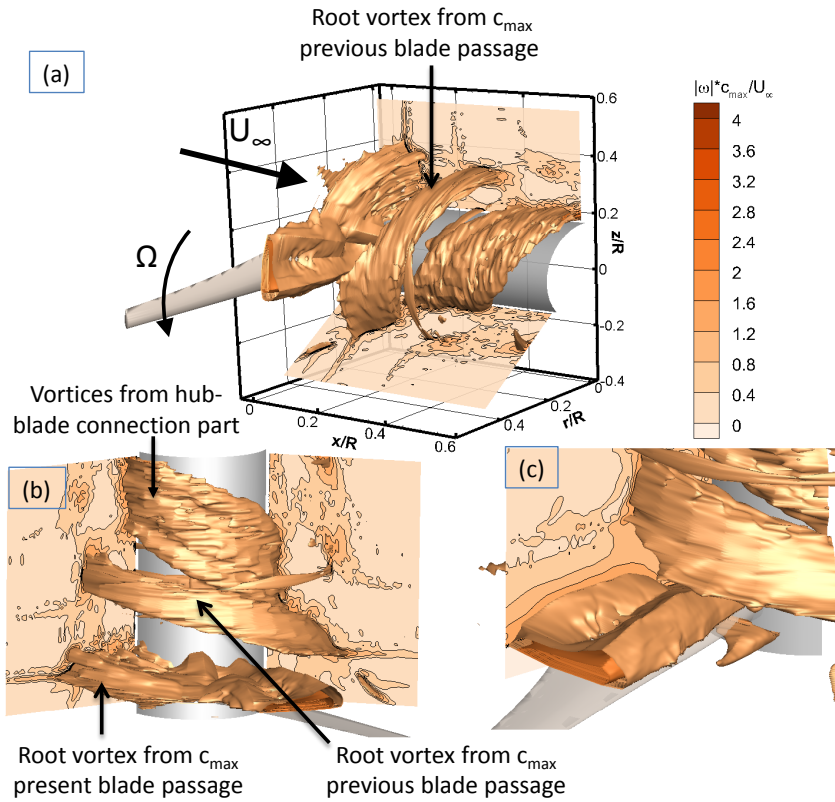


Figure 3.6: 3D visualization of dimensionless vorticity magnitude. Vorticity iso-surfaces at $\frac{|\omega|c_{\max}}{U_{\infty}} = 2.1$, and 1.5. (a) Side view (b) Top view (c) Zoomed-in to the root flow.

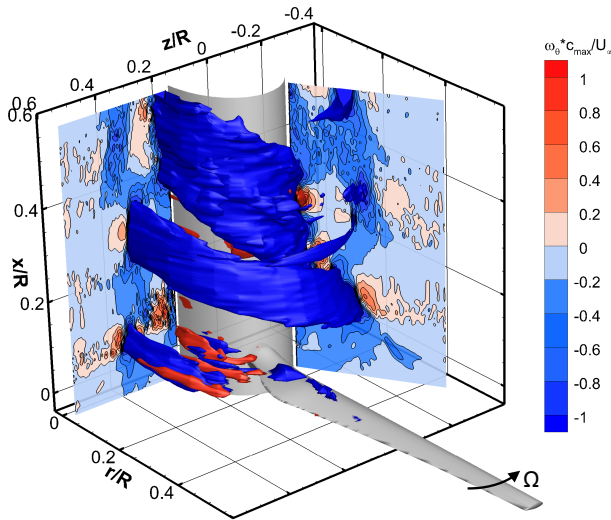
the present blade. In Figure 3.7, vorticity is presented in azimuthal, axial and radial directions.

Expected trailing vorticity can be observed in the azimuthal vorticity distribution (see Figure 3.7-a). The vorticity which is observed in the axial direction (see Figure 3.7-b) can be due to tilting of the vortex tubes, expressed in the first two terms on the right hand side of Equation 3.1. In Figure 3.7-c large areas of positive and negative radial vorticity are observed near the blade suction surface. This may be due to detachment of the vorticity from a separated

boundary layer in the root region of the blade. The negative radial vorticity is also observed in the chordwise measurements (see Figure 3.8).

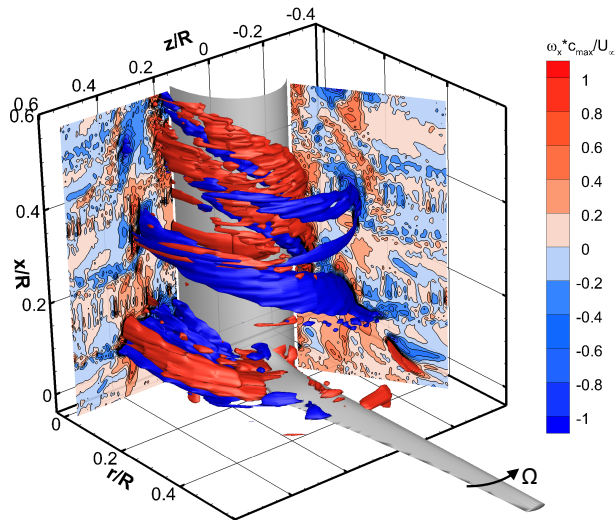
From the comparison of the three components of vorticity (see Figures 3.7-a, b, c), it can be seen that the radial vorticity component “dies out” when moving away from the blade in the axial direction. In other words, the trailing vorticity loses its radial component after around one revolution. This can be because the vorticity is redirected into azimuthal and axial directions. Thus, the radial component of the trailing vorticity sheet at the inboard part of the blade gradually decays in strength.

The azimuthal and axial vortices are more persistent. This certainly holds for the vorticity generated in the inner part of the blade root, that is from $r/R \cong 0.11$ to $r/R \cong 0.2$. The vorticity which is emanated from the blade maximum chord position ($r/R \cong 0.3$) is stretched in the axial direction. This can be observed best in Figure 3.7-a. Here, it may be useful to recall Figure 3.6 which shows the total vorticity.

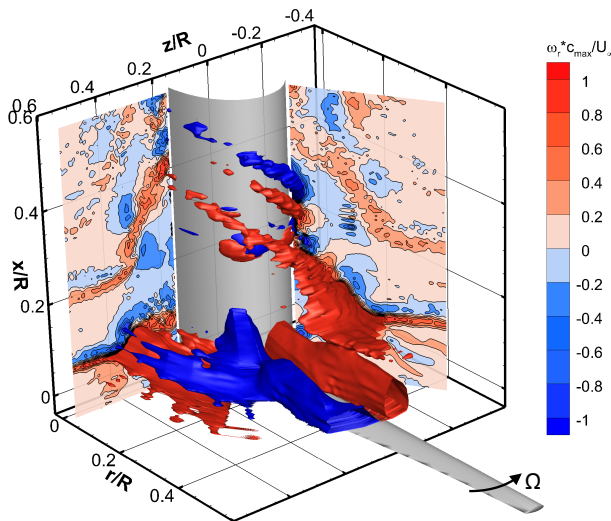


(a) Dimensionless azimuthal vorticity iso-surfaces at $\frac{\omega_{\theta} c_{max}}{U_{\infty}} = -1$, and 1.

Figure 3.7: 3D visualization of dimensionless vorticity components from stereoscopic PIV measurements.



(b) Dimensionless axial vorticity iso-surfaces at $\frac{\omega_x c_{max}}{U_\infty} = -1$, and 1.



(c) Dimensionless radial vorticity iso-surfaces at $\frac{\omega_r c_{max}}{U_\infty} = -1$, and 1.

Figure 3.7: (continued) 3D visualization of dimensionless vorticity components from stereoscopic PIV measurements.

3.2.2 2D spanwise vorticity around the blade

Returning to Figure 3.7-c, large areas of positive and negative radial vorticity are observed near the blade suction side. This may be because a large amount of vorticity detaches from a significantly separated boundary layer in the root region of the blade. Spanwise vorticity distributions at four radial positions from chordwise PIV measurements are presented in Figure 3.8. The negative radial vorticity is also observed in the chordwise measurements. Reverse flow regions which can clearly be seen in azimuthal velocity distributions (see Figure 3.5) coincide with the position of the negative spanwise vorticity distribution in Figure 3.8.

The positive vorticity along the leading edge in the root, which is seen in the dimensionless radial vorticity iso-surface (see Figure 3.7-c), is not observed in the spanwise vorticity distributions (see Figure 3.8). The velocity fields used to obtain dimensionless radial vorticity iso-surface (see Figure 3.7-c) is not the chordwise velocity measurements, which are used to obtain Figure 3.8. Therefore, the masked area in these fields, which are affected by reflections, are not the source of the positive vorticity along the leading edge in Figure 3.7-c. The positive vorticity along the leading edge in the root can not be explained with a physical meaning. Although, it can not also be proven that it is due to noise in the measurements, it may be caused by experimental and numerical treatment of the spanwise PIV fields while obtaining the three dimensional vorticity components. Moreover, it may be seen very dominant due to the vorticity scale of Figure 3.7-c.

3.2.3 2D azimuthal vorticity in the near wake region

To better understand the vorticity generation and evolution in the blade wake region near the root, it helps to analyze the vorticity distributions at different blade azimuth angles in 2D planes. Azimuthal vorticity distributions in the blade wake region are presented in Figure 3.8 in 2D planes, at eight different blade angles from $\Theta = -45^\circ$ until $\Theta = 90^\circ$ (see Figure 2.5 for the blade reference angle). To have a better visualization of vorticity contour, mean of the every 4 data points is plotted after the calculation of vorticity.

Two blobs of vorticity can be seen in the root region (see Figure 3.8). One vortex blob emanates from the circular cross section of the blade (from $r/R \cong 0.15$ to $r/R \cong 0.2$); the other one from the maximum chord position at $r/R \cong 0.3$. The outer vortex blob is connected to the vorticity sheet leaving the blade further outboard of the location of the maximum chord.

While the vortices released in the previous blade passages are seen in all the

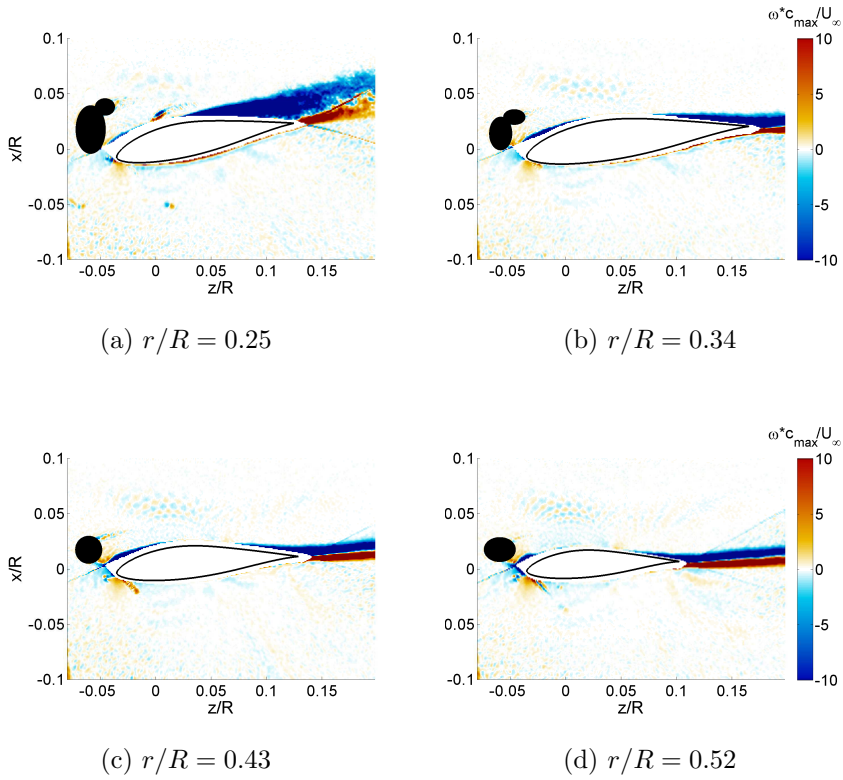


Figure 3.8: Dimensionless spanwise vorticity distributions at four radial positions from root (a) $r/R = 0.25$ to mid-board (d) $r/R = 0.52$, from stereoscopic PIV measurements in chordwise direction. Inflow is in $+x/R$ direction. Note that the data at $z/R = -0.05$ and $x/R = 0.025$ was masked due to reflection.

azimuth angles, one may see the newly generated positive vorticity at $\Theta = 20^\circ$ blade angle. In the later blade angles, there is a small amount of positive azimuthally directed vorticity together with a large amount of negative vorticity at a slightly different position. This flow property can be explained with the vorticity evolution around the blade.

Generation of a large amount of positive azimuthal vorticity can be clearly seen in Figure 3.8 at $\Theta = 35^\circ$ and $\Theta = 45^\circ$. Later on, this positive azimuthal vorticity is gradually disintegrated by the large negative one. Generation of this

large positive azimuthal vorticity can be physically explained by the initiation of the root vortex at the blade root surface. The root vortex may “creep” along the suction surface of the blade in the radial direction with a large amount of positive azimuthal vorticity. At the pressure surface this vorticity has a direction opposite to the vorticity at the suction surface. In the attached flow, the radial component of these vorticities should cancel each other to obtain Kutta condition. However, in azimuthal direction, it is not the case. And it results in the creation of trailing vorticity. This tube of vorticity, which has a diameter typically $0.05R$, persists in the separated flow in the trailing edge and moves radially outboard. In Figure 3.8-f, the vorticity tube, which is the root vortex, moves to the trailing edge and is then shed into the free flow around maximum chord position. In the wake, the vorticity tube changes direction such that mainly negative azimuthal vorticity remains (see Figure 3.8-h). This process can also be observed in the CFD simulations of the experiments.

In the boundary layer of a blade/wing (whatever) radial/spanwise vorticity is generated. At the suction side this vorticity has a direction opposite to the vorticity at the pressure side. In attached flow these radial components of these vortices should cancel each other (that is the Kutta condition) in azimuthal condition that is not the case (since this is how trailed vorticity is generated) So what we see here is the creation of trailing vorticity.

Comparison with observations from literature

Figure 3.8 presents also the evolution of the vortices in the blade wake region. While the vortices released from inner part of the blade root are conveying in the vicinity of the nacelle, the root vortex generated around c_{max} ($r/R \cong 0.3$) is expanding outboard. In the work of Sherry et al. (2010), a close interaction of the root vortex with the nacelle was observed which seems to be in conflict with the present results. Later study of Sherry et al. (2013) again showed the root trailing vortices in the vicinity of the nacelle. There are even more different observations from the root region, such as Whale et al. (2000). Whale et al. (2000) showed the hub vortices with the same direction of rotation merging with the tip vortex system. These kinds of differences may show the effects of the blade geometry, operating conditions, etc. Therefore, further analysis may be needed to reveal the effects of these parameters on the root flow structures.

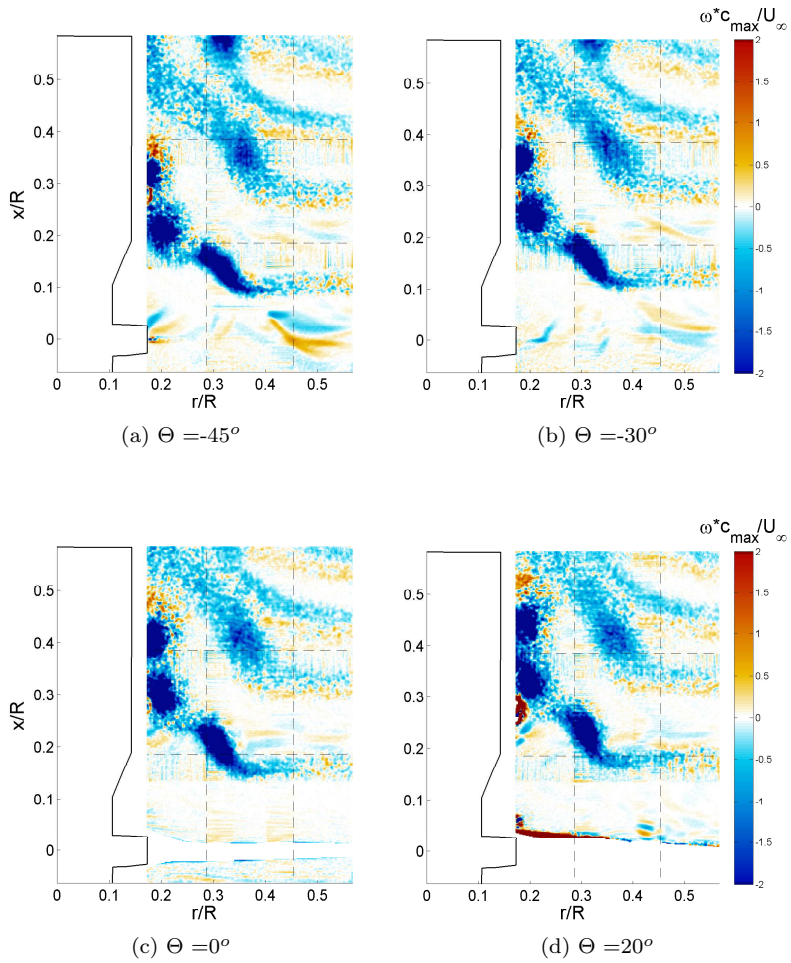


Figure 3.9: Dimensionless azimuthal vorticity distributions from stereoscopic PIV measurements.

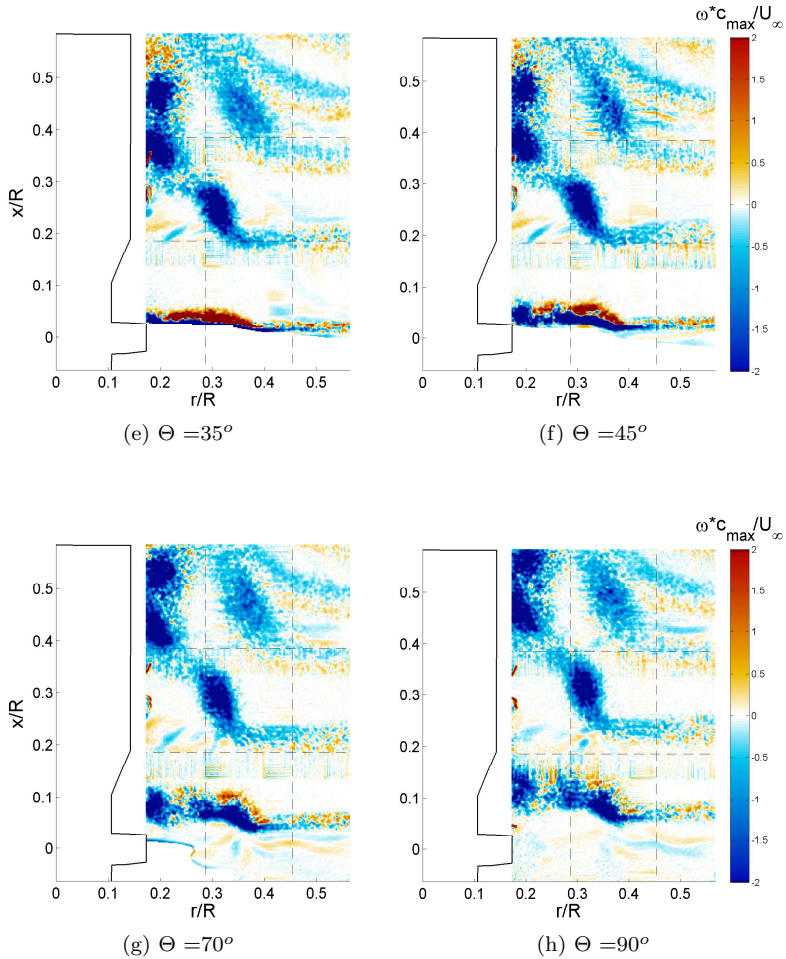


Figure 3.8: (continued) Dimensionless azimuthal vorticity distributions at eight blade azimuth angles from stereoscopic PIV measurements.

3.3 Pressure distribution in the near wake region

Visualizations of the pressure in 3D form and in 2D planes are numerical interpretations of the same information given in the vorticity distributions. Figure 3.9 presents the 3D pressure coefficient distribution. The pressure coefficient is calculated as in Equation 3.2.

$$c_p = \frac{p_{static} - p_\infty}{\frac{1}{2}\rho V^2} \quad (3.2)$$

where P_∞ is the ambient pressure, ρ is the air density and V is the measured velocity in the near wake region. The pressure can be obtained from integration of the pressure gradient inferred from the momentum equation in differential form. The three dimensional pressure distribution is obtained from the 3D calculation. It shows, as expected, how the blade determines a decrease in the static pressure on the suction surface of the blade which is stronger than the pressure drop due to the vortical flow structures in the blade near wake. Asymmetries on the pressure distribution are influenced by the previously mentioned vortical structures, which are difficult to perceive in the three-dimensional visualization.

In order to analyze the finer details, the vorticity magnitude ($|\omega|$) and pressure coefficient (c_p) are presented in 2D planes at two azimuth angles. In Figure 3.10 and Figure 3.11, the vorticity magnitude (left) and the pressure coefficient (right), calculated from the PIV velocity fields, are presented before ($\Theta = -20^\circ$) and after ($\Theta = 75^\circ$) the blade passage. The vortices observed in the vorticity distribution, already analyzed in Section 3.2, can be noted in C_p distributions with the highest values. However, there are some regions in the vorticity distributions, where the vortical structures are expected to be, decrease in the static pressure is not observed (e.g., Figure 3.10 at $x/R = 0.38$ and $r/R = 0.2$ and Figure 3.11 at $x/R = 0.1$ and $r/R = 0.2$). There may be three reasons to explain this behavior: (i) The core of the vortical structure can be outside of the field although a high vorticity is noted in the field. (ii) High vorticity level can only show a significant pressure drop. (iii) Due to uncertainties in the velocity gradients at the edge of the field.

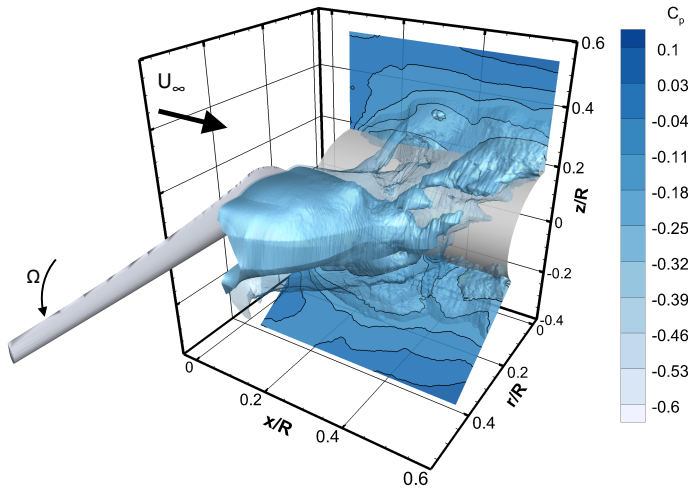


Figure 3.9: 3D visualization of pressure coefficient, iso-surfaces at $C_p = -0.14$, and -0.25 .

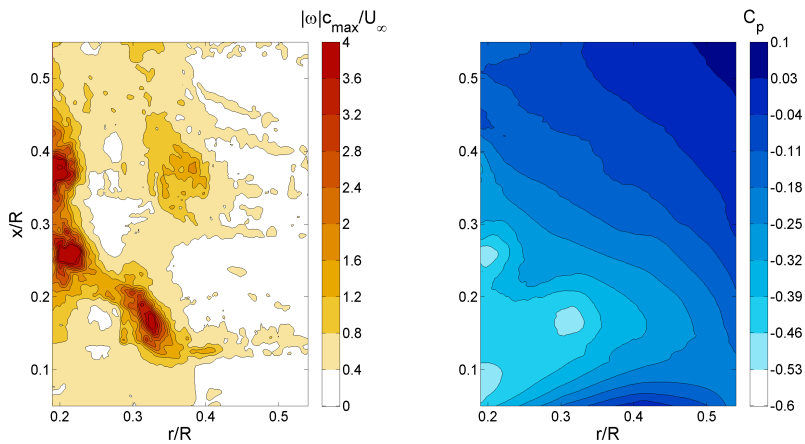


Figure 3.10: Dimensionless vorticity magnitude and pressure coefficient contour plots, blade azimuthal position $\Theta = -20^\circ$.

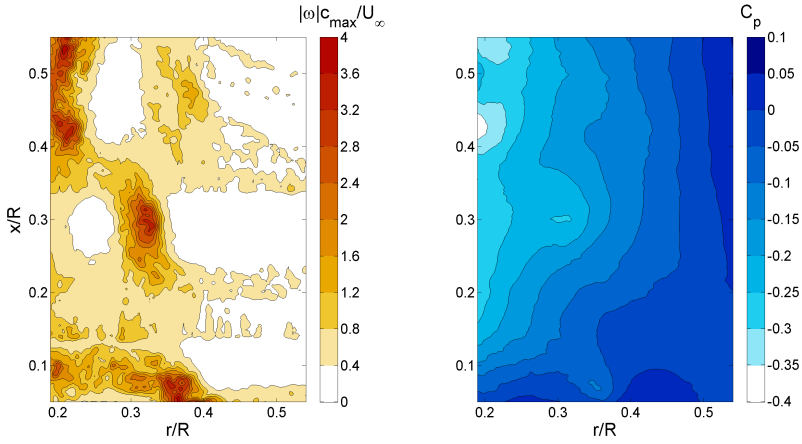


Figure 3.11: Dimensionless vorticity magnitude and pressure coefficient contour plots, blade azimuthal position $\Theta = 75^\circ$.

3.4 Summary and chapter conclusions

This chapter presented the evolution of the wake and the flow in the near wake region of a horizontal axis wind turbine blade root region. A deeper understanding of the flow behavior and the progression of the root vortex in the near wake of the blade root region is gained with the help of detailed analysis based upon the stereoscopic PIV experiments.

Higher axial velocities are observed in the inboard region along the nacelle. The velocity values approach around $1 \times U_\infty$ which is beyond the expected axial velocities based on the momentum theory.

The movement of the wake sheets in the axial direction, which can be seen with the traces of the blade passages in the near wake of the blade, is observed in the azimuthal velocity distributions.

The present study shows an outboard radial motion at the root region, with a complementary inboard one at the maximum chord region (at $r/R \cong 0.3$), due to a strong root vortex released from the maximum chord. Moreover, there is an increase in the axial velocity along the nacelle. While the velocity increase may be explained with the presence of the vortices in the root region, it might also be caused by the lack of aerodynamic thrust in this part of the rotor disc. This will lead to an increase of axial velocities.

Two blobs of vortex are released, one from the maximum chord and the other from the circular cross section of the blade. They are perceived in both the vorticity and pressure distributions. Furthermore, the evolution of these vortices in the blade wake region is analyzed from the different blade azimuth angle distributions. Unlike the observations in the literature, the root vortex emanating around the maximum chord position $r/R \cong 0.3$ does not interact with the nacelle, but expands in the outboard direction. Whereas the vorticity released from the inner part of the blade–hub connection is convected axially, staying in the vicinity of the nacelle.

Three-dimensional velocity, vorticity and pressure distributions help to improve understanding the 3D flow structures in the root region.

The vorticity in the radial direction shows boundary layer separation on the suction surface of the blade. This separated region is also observed in the tangential velocity and spanwise vorticity distributions from chordwise measurements.

This analysis reveals that there is a vorticity driven flow in the blade root region and shows the clear presence of the root vortex. Hence, the local effects of the root vortex cannot be ignored. In the following chapter, the effects of the blade geometry and the tip speed ratio on the formation of the root vortex will be investigated.

Chapter 4

Effects of geometry and tip speed ratio on the HAWT root flow

This chapter is based on the journal paper:

*Experimental analysis of the evolution of the HAWT root flow
B. Akay, D. Micallef, C.J. Simão Ferreira and G.J.W. van Bussel
Journal of Physics: Conference Series. IOP Science (2012).*

In Chapter 3, an extensive experimental analysis in the root region of a horizontal axis wind turbine (HAWT) blade was performed. Three dimensional behavior of the root vortex and the pressure distribution of the near wake were analyzed as well as the three components of velocity and vorticity distributions at different blade azimuth angles. Chapter 3 revealed the need for further investigations in the root region.

The effect of the parameters playing a role in the root flow behavior of HAWTs are only partly understood. To better reveal the root flow properties, this chapter presents the progression of HAWT blade root flow for two different

blade geometries and at two different tip speed ratios. The effects of the geometry and the tip speed ratio on the root flow behavior and on the evolution of the root flow features are investigated. This chapter aims at answering the following questions: (i) What are the effects of the blade geometry and tip speed ratio on the root flow behavior? (ii) How are the blade wake and the root vortex evolution affected by the change of these parameters?

Chapter outline

- Section 4.1.1 presents the three components of velocity distributions obtained from PIV experiments in 2D planes at three test cases.
- Section 4.1.2 analyzes the vorticity distributions computed using PIV velocity fields in 2D planes.
- Section 4.1.3 presents the circulation distribution along the span of Blade 1 and Blade 2 at $\lambda = 7$.
- Section 4.2 presents the key results of this chapter and the main conclusions.

4.1 Comparison of three test cases

4.1.1 Velocity distributions in the near wake region

In this section, the phase-locked average velocities are presented in the near wake region at different blade azimuth angles. The experimental results for three test cases are compared (the reader is referred to Table 2.1 for the measurement conditions of the tests). The velocities measured around Blade 1 at $\lambda = 7$ were presented earlier in Chapter 3 and are repeated here for comparison with the two other cases. It is important to note that the radial and axial extents of the figures are not the same in all three cases. Hence, the scale of the axis might differ from each other.

Figures 4.1, 4.2, and 4.3 present axial and azimuthal velocity distributions in the near wake region of the three test cases (Blade 1 at $\lambda = 7$, Blade 2 at $\lambda = 7$, Blade 2 at $\lambda = 5$) at $\Theta = 45^\circ$. From the comparison of axial and azimuthal velocity distributions of the three test cases, it can be seen that Blade 1 at $\lambda = 7$ has the lowest axial velocities in the near wake region and Blade 2 at $\lambda = 5$ has the highest velocities. In other words, Blade 1 at $\lambda = 7$ encounters the highest loads, whereas Blade 2 at $\lambda = 5$ has the lowest loads.

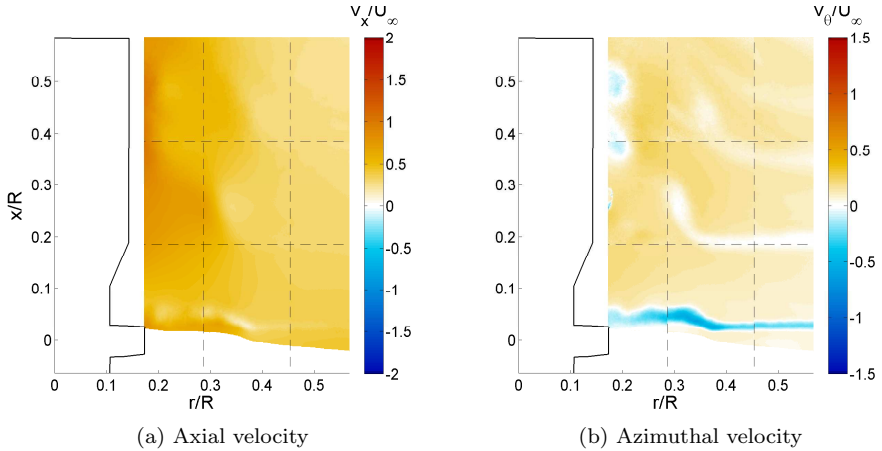


Figure 4.1: Blade 1 at $\lambda = 7$, dimensionless axial and azimuthal velocity distributions at $\Theta=45^\circ$ from stereoscopic PIV measurements. Inflow is in $+x/R$ direction.

The axial flow acceleration near the nacelle, which was already discussed in Section 3.1, is observed in all three test cases.

Positive azimuthal velocity areas show that the rotor wake region develops as expected with a rotation in the opposite direction of the blade rotation. Negative azimuthal velocities, which are moving in the same direction as the blade rotation (into the plane of observation), are also observed in the blade wake region of the three test cases. These regions are the manifestation of the presence of the viscous wake of the blades. The boundary layer material is shed from the blade and is subsequently conveyed in the downstream direction with the wake. The vortex wake is immersed into this viscous wake. It is noted that the thickness and the shape of the wake sheets (in axial direction) at three test cases differ from each other.

The axial movement of the wake sheets is best observed in the azimuthal velocity distribution of Blade 1 at $\lambda = 7$. It is about $r = 0.2R$ for half a revolution and it becomes $\sim 0.4R$ for a full revolution. In the second test case (Blade 2 at $\lambda = 7$), the axial translation of the wake sheets is observed only for half a revolution and it is about $r = 0.4R$. This is consistent with the lower induction (higher axial velocities and lower loads) on the second blade test at the same λ .

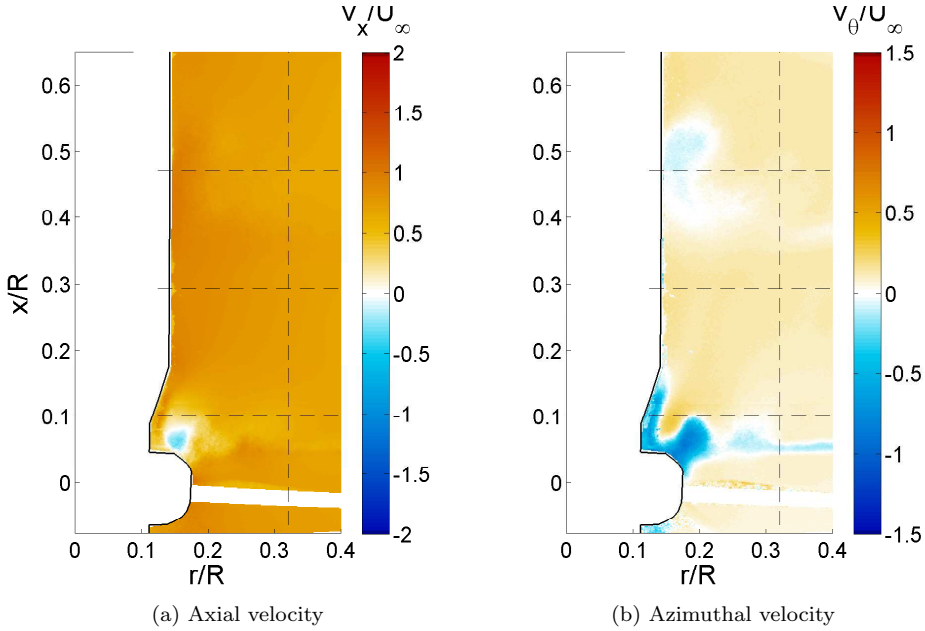


Figure 4.2: Blade 2 at $\lambda = 7$, dimensionless axial and azimuthal velocity distributions at $\Theta=45^\circ$ from stereoscopic PIV measurements. Inflow is in $+x/R$ direction.

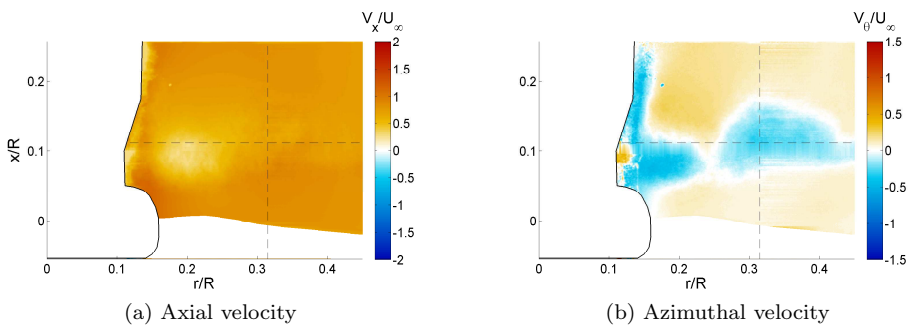


Figure 4.3: Blade 2 at $\lambda = 5$, dimensionless axial and azimuthal velocity distributions at $\Theta=45^\circ$ from stereoscopic PIV measurements. Inflow is in $+x/R$ direction.

Figures 4.4, 4.5, and 4.6 present radial velocity distributions in the near wake region of the blades at two blade azimuth angles for three test cases. While inboard radial flow is observed at around the maximum chord ($r/R \cong 0.3$) of Blade 1 in Figure 4.4-a, the flow is fully outboard in the wake region of Blade 2 at $\lambda = 7$ at $\Theta = 0^\circ$ (see Figure 4.5-a). For the same blade geometry (Blade 2) but at different λ , a small inboard flow motion is observed at around maximum chord ($r/R = 0.25$) (see Figure 4.6-a).

At $\Theta = 45^\circ$ azimuth angle, the boundary layer flow from the blade passage left in the wake region can be clearly seen with the inboard and outboard radial motion at three test cases. As expected the “scar” of the blade passage is observed further in the downstream for Blade 2 at $\lambda = 5$ than that for Blade 2 at $\lambda = 7$ due to higher freestream velocity. In radial velocity distributions for all three cases, the footprint of the vortical structures oriented in the azimuthal direction can also be observed just behind the blade and in the near wake region. The vortical structures just behind the blade coincide with the negative azimuthal velocities (wake sheets) noted in Figures 4.1-b, 4.2-b, 4.3-b.

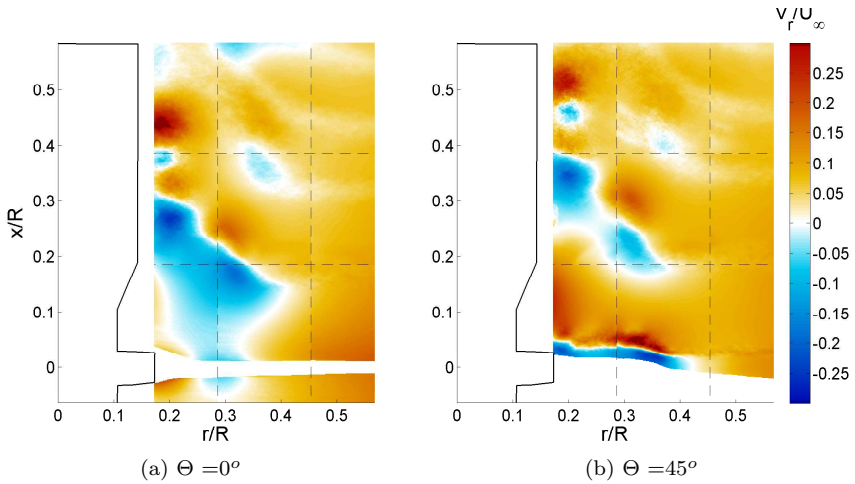


Figure 4.4: Blade 1 at $\lambda = 7$, dimensionless radial velocity distribution from stereoscopic PIV measurements. Inflow is in $+x/R$ direction.

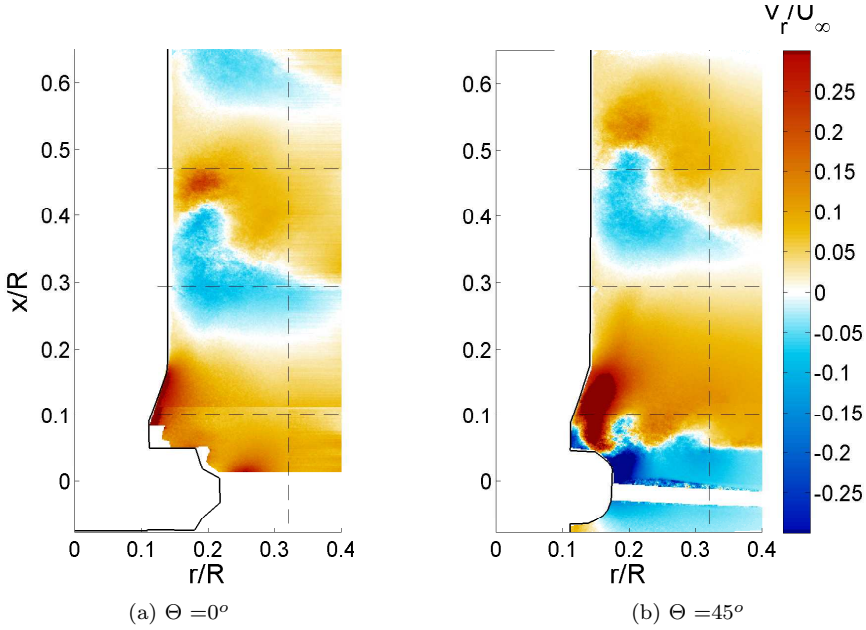


Figure 4.5: Blade 2 at $\lambda = 7$, dimensionless radial velocity distribution from stereoscopic PIV measurements. Inflow is in $+x/R$ direction.

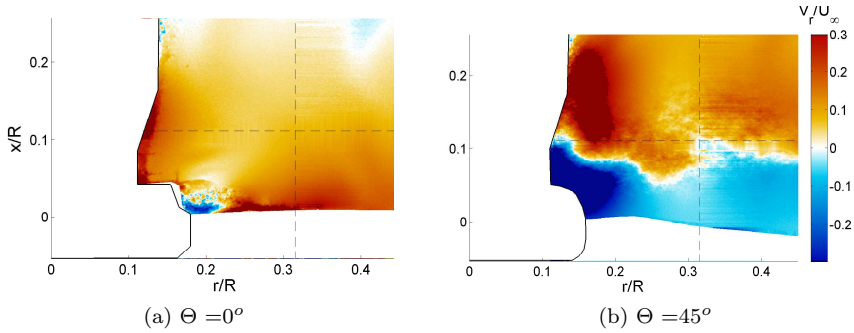


Figure 4.6: Blade 2 at $\lambda = 5$, dimensionless radial velocity distribution from stereoscopic PIV measurements. Inflow is in $+x/R$ direction.

Figures 4.7, 4.8 present the velocities extracted at $x/R = 0.05$ and $x/R = 0.1$ respectively from the velocity fields for three test cases. It is clearly seen that the velocities at $x/R = 0.05$ position are highly distorted by the presence of the blade. When radial velocities at $x/R = 0.1$ for the three test cases are compared, it is noted that Blade 1 at $\lambda = 7$ shows a different trend than the cases for Blade 2. The radial velocities for Blade 1 show negative values around maximum the chord position ($r/R \cong 0.3$). This demonstrates that the local geometry of the blade plays a role in the radial velocity distribution in close vicinity of the blade.

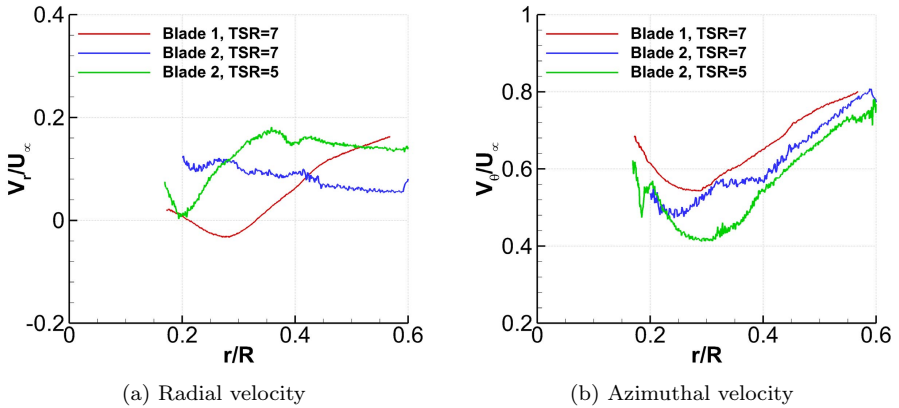


Figure 4.7: Dimensionless velocity plots at $\Theta=0^\circ$, $x/R = 0.05$ for three test cases, from stereoscopic PIV measurements.

It can be observed from the comparison of the azimuthal velocities extracted at two downstream positions ($x/R = 0.05$ and $x/R = 0.1$) that there is a sudden azimuthal velocity increase in the root region when going inboard from around maximum chord position ($r/R \cong 0.3$) towards the nacelle (see Figure 4.7-b). On the other hand, more constant velocity distributions are observed at $x/R = 0.1$. This is because at $x/R = 0.05$, the extracted azimuthal velocity coincides with the axial position of the wake sheets for the three test cases. The differences in the azimuthal velocity distributions between the test cases originate from both the differences in the geometries and also the differences in the flow separation from the blades.

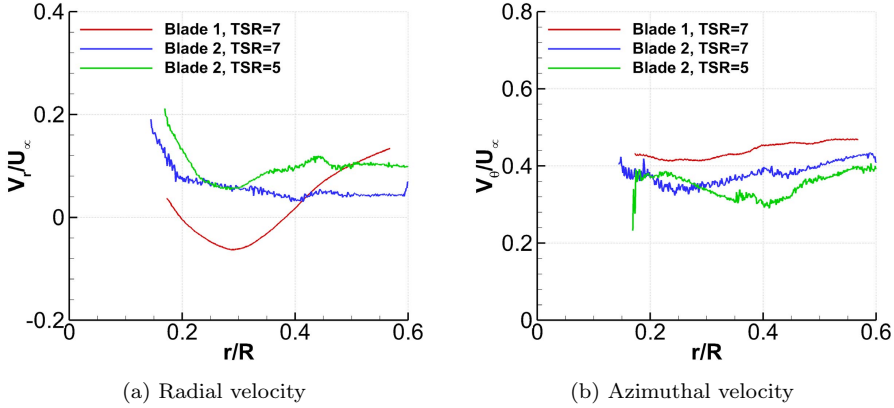


Figure 4.8: Dimensionless velocity plots at $\Theta=0^\circ$, $x/R = 0.1$ for three test cases, from stereoscopic PIV measurements.

4.1.2 Vorticity distributions in the near wake region

Azimuthal vorticity distributions are presented in Figures 4.9, 4.10 and 4.11 on 2D planes at two blade azimuth angles. It should be noted here that “vorticity creation” or “vorticity disappearance” may not be concluded by only analyzing the azimuthal vorticity distributions presented in this section. As it was already demonstrated in Section 3.2.1, vorticity may change direction and this may lead to a change in azimuthal vorticity while the total vorticity does not change.

Vorticity distributions for Blade 1 at $\lambda = 7$ were already presented in Section 3.2 and are repeated here for comparison with the other two test cases. The first point drawn from the comparison of vorticity distributions for Blade 1 and Blade 2 at $\lambda = 7$ is the number of vortices formed in the root region of the two blades. Two vorticity blobs are observed for Blade 1; one is emanated from the circular cross section of the blade (from $r/R \cong 0.15$ to $r/R \cong 0.2$) and the other one is around maximum chord position ($r/R \cong 0.3$). By contrast, only one vorticity blob is generated for Blade 2, emanated from the hub-blade connection part. For Blade 2, the vorticity is not as concentrated as for Blade 1. It is more diffused over a larger area which does not mean that there is no root vortex. The strength of the trailing vorticity will be analyzed in the following section which demonstrates whether there is an increase of vorticity strength over a smaller range of radial distance.

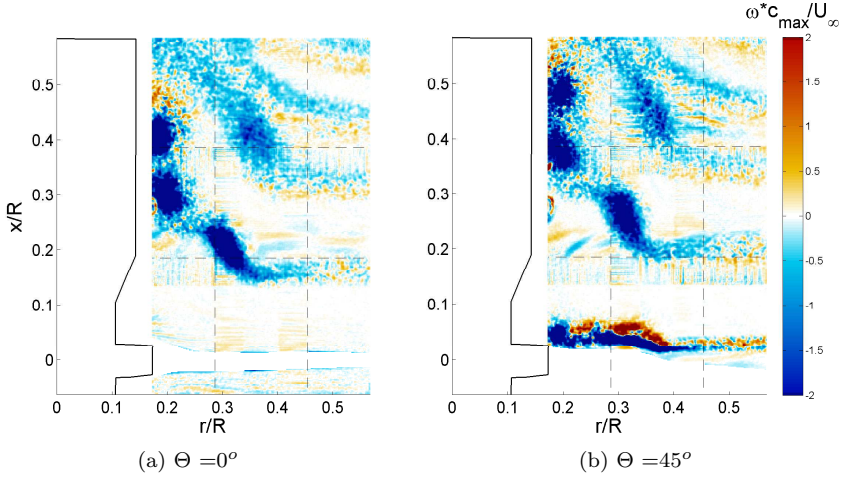


Figure 4.9: Blade 1 at $\lambda = 7$, dimensionless azimuthal vorticity distributions calculated from stereoscopic PIV measurements. Inflow is in $+x/R$ direction.

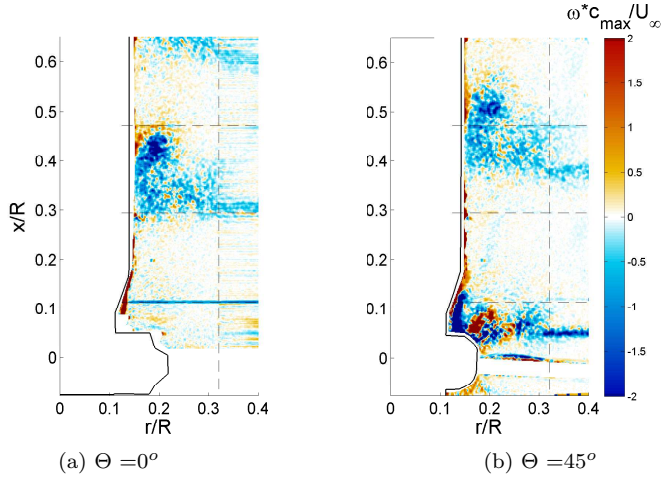


Figure 4.10: Blade 2 at $\lambda = 7$, dimensionless azimuthal vorticity distributions calculated from stereoscopic PIV measurements. Inflow is in $+x/R$ direction.

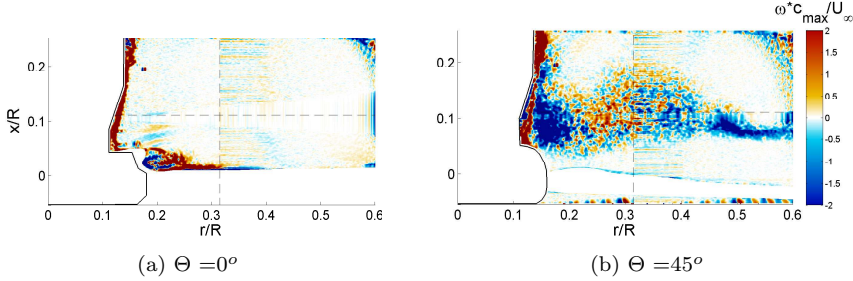


Figure 4.11: Blade 2 at $\lambda = 5$, dimensionless azimuthal vorticity distributions calculated from stereoscopic PIV measurements. Inflow is in $+x/R$ direction.

Positive and negative vorticity just behind Blade 2 at $\Theta = 45^\circ$ is similar in behavior to what was discussed previously for Blade 1. For both blades, there is a vorticity sheet at $x/R \cong 0.05$ extending in radial direction. The comparison of Blade 1 and Blade 2 at $\lambda = 7$ shows that the evolution of the root vortex highly depends on the blade geometry and the resulting circulation distribution.

From the comparison of vorticity distribution for Blade 2 at different λ and at $\Theta = 45^\circ$ (see Figures 4.10-b and 4.11-b), it can be noted that there is a more concentrated vortex blob for Blade 2 $\lambda = 5$ at around $x/R = 0.08$ and $r/R = 0.17$. However, the vorticity in the leeward side of the blade is distributed in a larger area with positive and negative values. There is again a vorticity sheet attached to the vortex blob extending outboard.

4.1.3 Spanwise bound vorticity and the strength of trailing vortex

It is possible to deduce the variation of the circulation along the blade radius by evaluating the velocity measurements at several spanwise positions of the blade. The circulation is calculated by integrating the velocities around a rectangular contour (see Figure 4.12) and it is defined by Equation 4.1.

$$\Gamma = \oint_C V \cdot ds \quad (4.1)$$

where V is the in-plane velocity and ds is the incremental length along the contour line. The calculations are performed for four different contour lengths

and it is seen that there is no significant effect of contour length on the calculation of circulation from the PIV velocity data used in this analysis. Also, the strength of each trailing vortex is calculated from the change in circulation along the blade span.

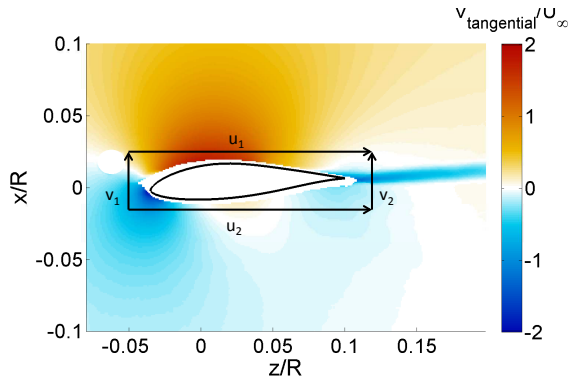


Figure 4.12: Representation of rectangular contour approach for circulation calculation. Non-dimensional tangential velocity contour at $r/R=0.52$.

Figure 4.13 presents the dimensionless spanwise bound vorticity at several radial locations for Blade 1 and Blade 2 at $\lambda = 7$. While the mid-board region shows an almost constant circulation distribution at Blade 1, Blade 2 has lower values but an increasing trend in this region. The sudden drop in the circulation at the root region of Blade 1 shows the position of the root vortex formed at around c_{max} ($r/R \cong 0.3$). The strength of the each trailing vortices is derived from the change in circulation and is presented in Figure 4.14. In Blade 1, a strong root vortex is observed with the higher strength values in the root region. While for Blade 1, the strength of the trailing vortices in the mid-board region is very close to zero, Blade 2 has higher values in this region. Here, it should be noted that Blade 2 has measurements starting from $r/R = 2.6$. Although there is a slight increase in the vorticity strength of Blade 2 between $r/R = 3.4$ and $r/R = 2.6$, due to lack of measurements beyond this region towards the hub, drawing a conclusion about the presence of a strong root vortex is difficult.

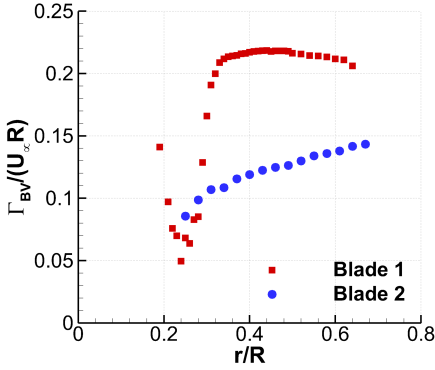


Figure 4.13: Blade 1 and Blade 2 at $\lambda = 7$, dimensionless spanwise bound vorticity obtained from the chordwise stereoscopic PIV experiments.

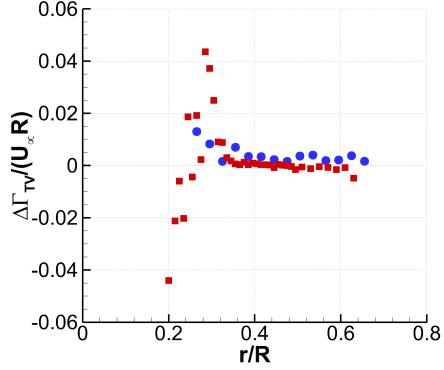


Figure 4.14: Dimensionless strength of trailing vortex derived from the bound circulation.

4.2 Summary and chapter conclusions

In this chapter, the evolution of HAWT blade root flow for different blade geometries and at different tip speed ratios has been analyzed. The velocity and vorticity fields in the near wake region at different blade azimuth angles for three test cases were analyzed. Furthermore, the bound vorticity and the strength of the trailing vorticity were compared for Blade 1 and Blade 2 at $\lambda = 7$. Following conclusions are drawn from the results presented in this chapter:

1. It is shown that the radial flow behavior changes with different blade geometries but a remarkable difference in the radial flow behavior is not observed with the change of tip speed ratio.
2. Wake vorticity sheets are clearly observed in the azimuthal velocity distributions with negative values in all the test cases. However, the formation of the wake is different for the three test cases because of the different loading that the blades encounter.
3. An increase in the axial velocity just behind the blade in the region very

close to the nacelle is observed for the three test cases.

4. The circulation distribution of Blade 1 at $\lambda = 7$ shows a strong root vortex with a sudden drop at the maximum chord ($r/R \cong 0.3$). The comparison of the circulation distributions of two blades shows that Blade 1 is a blade designed to perform according to optimal loading.
5. Based on the vorticity distributions and the strength of the trailing vorticity, it can be concluded that a clear root vortex is not observed for Blade 2 at $\lambda = 7$ and the bound vorticity builds up gradually when moving outboard.
6. Blade 2 at $\lambda = 5$, $\Theta = 45^\circ$ shows the vorticity distributed in a larger area in the leeward side of the blade. This may be caused by a very thick boundary layer close to flow separation.
7. This study demonstrates that the evolution and strength of the root vortex highly depends on the blade geometry and the distribution of circulation.

Chapter 5

Role of the root vortex in three dimensional flow

In Chapters 3 and 4, a mostly qualitative analysis of the horizontal axis wind turbine (HAWT) blade root flow was performed. The effects of the geometry and the tip speed ratio on the root flow behavior and on the evolution of the root flow features were investigated by using stereoscopic particle image velocimetry (PIV) measurements.

In the present chapter, we aim to elaborate the contribution of the root vortex in the blade flow behavior. For this purpose, first, the velocity induced by the root vortex is determined by applying the Biot-Savart law on a volume of the experimentally measured distribution of vorticity. Next, the three dimensional characteristics of the root flow are analyzed based upon, in particular the distribution of the spanwise flow in the inviscid flow region.

In this chapter, the results obtained from stereoscopic PIV measurements on Blade 1 at $\lambda = 7$ are used (the reader is referred to Table 2.1 for the measurement conditions).

Chapter outline

- Section 5.1 quantifies the strength of the root vortex.
- Section 5.2.1 investigates the root vortex strength in the near wake.
- Section 5.2.2 analyzes the distribution of induced velocities calculated from the experimental vorticity distribution.

- Section 5.3 analyzes the spanwise velocities in the inviscid flow region over the blade.
- Section 5.4 discusses the key results of this chapter and draws the main conclusions.

5.1 Bound vorticity of the root vortex

Bound vorticity and the trailing vorticity strength were calculated from the PIV velocity measurements and presented in Chapter 4, Section 4.1.3 for Blade 1 and Blade 2. Here, only Blade 1 at $\lambda = 7$ will be considered.

Figure 5.1 presents the dimensionless bound vorticity distribution along Blade 1. While the mid-board region shows an almost constant bound vorticity distribution, a drop from $\Gamma_{BV}/(U_\infty R) \cong 0.21$ to $\Gamma_{BV}/(U_\infty R) \cong 0.05$ in the bound vorticity is observed around maximum chord position (c_{max} , $r/R \cong 0.3$). This steep gradient of the bound vorticity around c_{max} indicates the generation of the root vortex at this radial position. At a more inboard position, the bound vorticity recovers from $\Gamma_{BV}/(U_\infty R) \cong 0.05$ to $\Gamma_{BV}/(U_\infty R) \cong 0.15$ at the circular cross section of the blade. In Figure 5.2 at $r/R \cong 0.2$, a secondary vorticity blob is observed near the blade. The presence of this vorticity blob may be related to the increase in the bound vorticity seen in this region in Figure 5.1.

Whale et al. (2000) stated that the change in bound vorticity is high at the tip of a HAWT blade, resulting in a strong trailing vortex in this region. However, at the blade root, they observed a weak diffused trailing vortex which may indicate smaller gradients in the bound vorticity in this region. Contrarily to what Whale et al. (2000) observed in their study, in the present research, a strong root vortex is observed for Blade 1, representing a steep gradient of bound vorticity (see Figure 5.1 between $r/R \cong 0.24$ and $r/R \cong 0.3$). Nevertheless, by applying other geometries in the root region, the gradient of the bound vorticity may be spread over a larger portion of the blade, instead of being concentrated in a small region. This can be seen for Blade 2, which also shows a much more gradual build up of bound vorticity in the inboard region. This shows the effect of the geometry on the bound vorticity distribution.

This section concludes the presence of a root vortex emanation around $r/R \cong 0.24$ with a strength of approximately $\Gamma_{BV}/(U_\infty R) \cong 0.15$. Hence, the following sections aim to investigate whether this root vortex strength is also present in the near wake directly behind the blade and what the role of this vortex is on the blade's flow distribution.

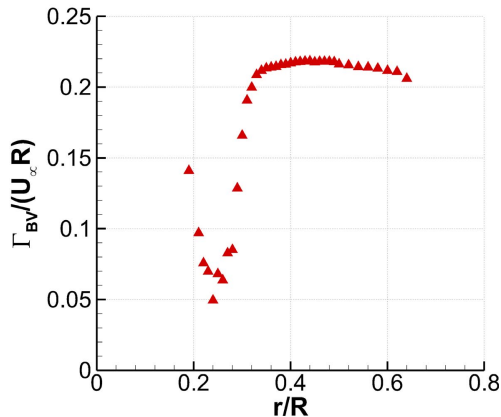


Figure 5.1: Dimensionless bound vorticity calculated from chordwise stereoscopic PIV measurements.

5.2 Velocity induced by the root vortex

This section aims to analyze quantitatively the role of the root vortex in the blade flow. For this purpose, the velocities induced by the volume distribution of measured root vorticity are calculated by using the Biot-Savart law. This enables to examine the contribution of the root vortex in the evolution of the velocities over the blade.

5.2.1 Root vortex strength in the near wake

The strength of the vortex tube is evaluated by the integral of the azimuthal vorticity, which is calculated by using the experimental data obtained from the PIV measurements for each azimuth angle at which measurements are available. Some examples of the PIV measurements can be seen in Figure 5.2. Although the total vorticity is not necessarily directed only in azimuthal direction, Stokes's theorem guarantees that the total circulation is the result of the calculation of circulation in the constant azimuthal plane by choosing the right path of integration. One may still discuss that this provides only a good estimate of the azimuthal vorticity strength, but in order to compare this with the bound vorticity change, three components of vorticity (azimuthal, axial

and radial) should be vectorially added to obtain total vorticity.

Figure 5.2 shows, there are two azimuthal vorticity blobs visible just behind the blade; one is released from the circular cross section of the blade and the other one is emanated from the maximum chord (c_{max}) position of the blade. There might be more vorticity “blobs” present in the vicinity of the hub, but those could not be visualized through the present PIV set-up. Further away in the wake the vortices generated in the previous blade passage can also be observed in Figure 5.2.

Here, it should be noted that from the present blade there are two vorticity blobs, one in the red ellipse and the other in the black circle (see Figure 5.2) at $\Theta = 75^\circ$. And all the vorticity found within the green circle can be attributed to the passage of the previous blade through the plane. This will be explained later in this section with the total strength of the vorticity in the near wake.

Bound vorticity can be obtained from the PIV measurements by integrating the vorticity over a defined area. It is important to note that this method of bound vorticity estimation may be dependent on the contour choice, as there is a continuous distribution of vorticity between the two vorticity blobs. So, the location of the contour will influence the calculated vorticity strength. The present experimental results imply an additional challenge in choosing the correct contour because the vortices are not distinct and concentrated in a small area but are instead distributed over a larger region. Hence, the strength of the total vorticity released from the previous blade passage (delimited with the green line in Figure 5.2 at $\Theta = 75^\circ$ by “From previous blade passage”) is calculated as $\Gamma/(U_\infty R) \cong 0.19$. And the total dimensionless vorticity strength at the leeward side of the blade (delimited with the red and black line in Figure 5.2 at $\Theta = 75^\circ$ by “From present blade passage”), which can be measured from the current PIV results, is $\Gamma/(U_\infty R) \cong 0.085$.

If we recall Figure 5.1, it can be seen that the dimensionless total bound vorticity strength in the region from hub to c_{max} is $\Gamma/(U_\infty R) \cong 0.2$. We are able to retrieve 95% of the total vorticity strength in the near wake by only adding the vorticity strength obtained from the “previous blade passage” to the one at the leeward side of the blade. This brings us to the conclusion that the PIV FOV miss the region very near to the blade. However, it should be noted that there may be other reasons for the missing vorticity strength which are listed as follows:

- The difference in the strength can be due to the result of the choice of the integration area.
- Three dimensionality of the root vortex tube may cause this difference.

- A missing vorticity blob in the area where the PIV field of view is not able to cover.

Note that there are no measurements in the region very close to the nacelle (see Figure 5.2). Therefore, the dimensionless vorticity strength may be expected to be higher than 0.19 as the current PIV measurements do not cover the region close to the nacelle in the previous blade passage. Hence, the smaller amount of vorticity strength calculated at the leeward side of the blade may be explained with another vorticity blob emanated from the hub-blade connection part (from $r/R \cong 0.11$ to $r/R \cong 0.15$) which cannot be seen in the current PIV results. This assumption also explains two vorticity blobs further downstream near the nacelle, which have been mentioned previously in this section.

Figure 5.3 schematically presents the distribution of the vortices just behind the blade emanated from the present blade, and further downstream, released from the previous blade passage. Vorticity indicated with an arrow may be the one which cannot be seen in the PIV results, but appears from the previous blade passage further downstream.

Similar flow details are also obtained with the OpenFoam CFD code as performed by Ivan Herraéz Hernandez ¹.

The vorticity distributions obtained from CFD are provided in Appendix A, Figure A.11. Details of the CFD simulations will be explained in Chapter 6.

The same study for the vorticity strength estimation is also applied to the results obtained from Blade 2 at $\lambda = 7$ experiments. It confirms that with the current PIV set-up it is impossible to retrieve information near the nacelle and in the behind of the blade due to reflections. And it affirms that, while the total vorticity strength can be estimated further downstream, it is difficult to retrieve the total vorticity strength just behind the blade. This analysis for Blade 2 at $\lambda = 7$ is presented in Appendix A.5.

5.2.2 Induced velocity from volume distribution of the root vorticity

In the 3D approach, a 45° slice of vorticity volume distribution in the vicinity of the blade obtained from the experiments is used to calculate the velocity induced by a volume distribution of vorticity (see Figure 5.4). The 3D flow is constructed from $\Theta = 45^\circ$ to $\Theta = 90^\circ$ azimuth angles, where the root vortices released from the present blade passage is visible in the measurements. The root

¹CFD simulations are performed by Ivan Herraéz Hernandez from the Carl von Ossietzky University of Oldenburg.

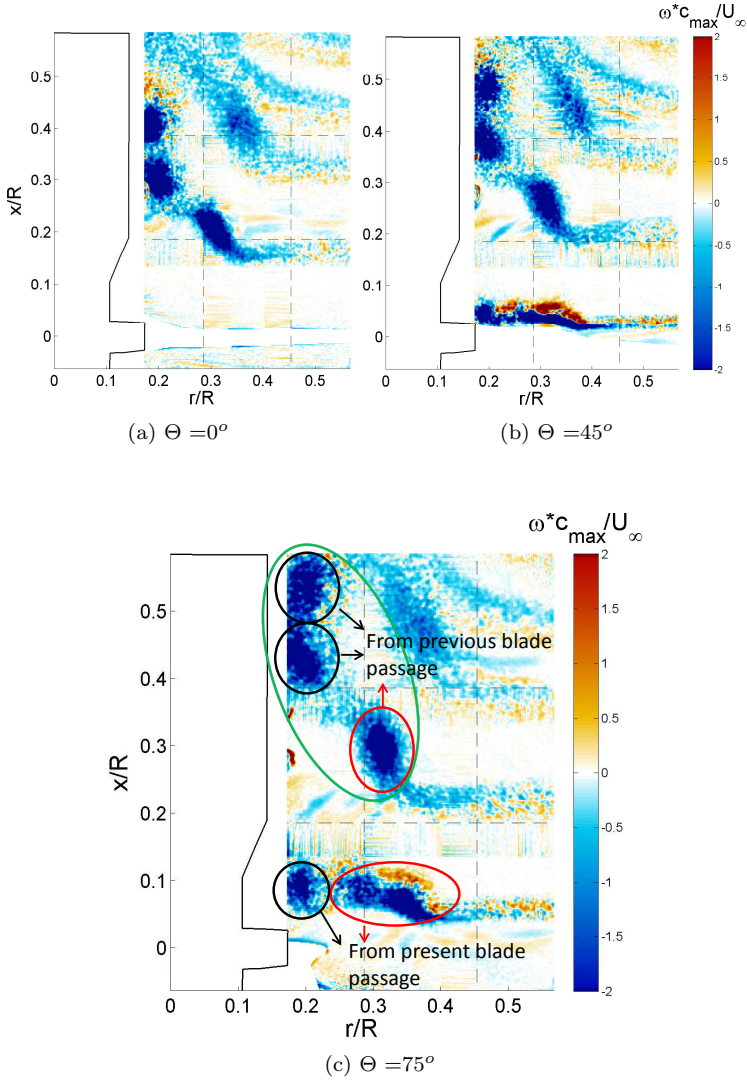


Figure 5.2: Dimensionless azimuthal vorticity contour at $\Theta = 0^\circ$, $\Theta = 45^\circ$, and $\Theta = 75^\circ$ from spanwise stereoscopic PIV measurements.

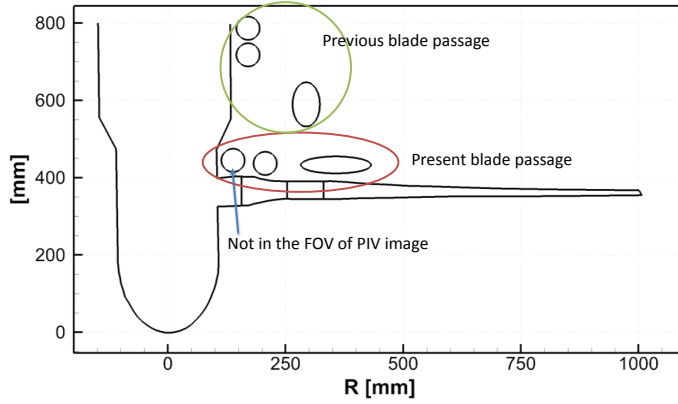


Figure 5.3: Schematic representation of the vortices in the near wake region. Note that the position of the vortices is taken from PIV measurements.

vortices generated in the previous blade passages are not taken into account in the calculations (see Figure 5.2).

The induced velocity due to a volume distribution of vorticity (see Katz and Plotkin (2001)) is given by

$$\mathbf{q} = \frac{1}{4\pi} \int_V \frac{\boldsymbol{\omega} \times (\mathbf{r}_0 - \mathbf{r}_1)}{|\mathbf{r}_0 - \mathbf{r}_1|^3} dV \quad (5.1)$$

where \mathbf{q} is the induced velocity, $\boldsymbol{\omega}$ is vorticity, $(\mathbf{r}_0 - \mathbf{r}_1)$ is the distance between the vorticity point and the point where the induced velocity is calculated. To simplify the computations, a discretization of volume integral is used and hence, Eq. 5.1 becomes

$$\mathbf{q} = \frac{1}{4\pi} \sum_{n=1}^{n_{points}} \frac{(\boldsymbol{\omega} * \Delta V) \times (\mathbf{r}_0 - \mathbf{r}_1)}{|\mathbf{r}_0 - \mathbf{r}_1|^3} \quad (5.2)$$

Induced velocities calculated by the volume distribution of vorticity method are presented in Figure 5.5. Directions in the Cartesian coordinate system are defined such as that $+x$ is in the direction from the pressure side to the suction side of the blade which is also the inflow direction, $+y$ is in the direction from root to tip of the blade, and finally $+z$ is in the direction from leading edge to trailing edge of the blade profile.

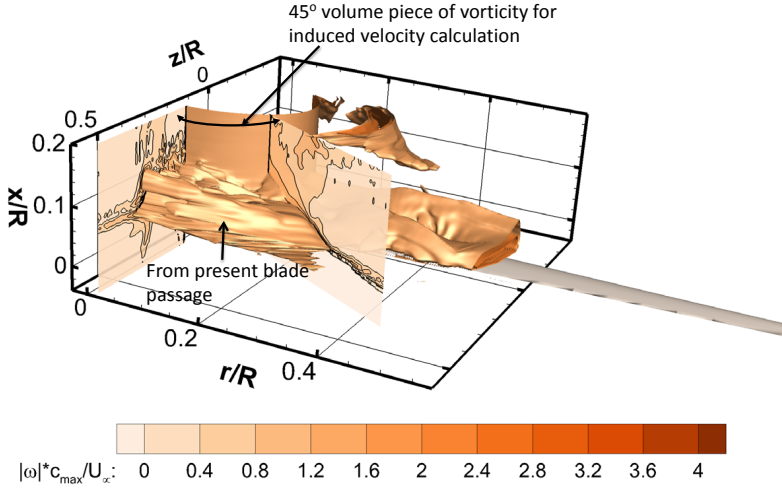
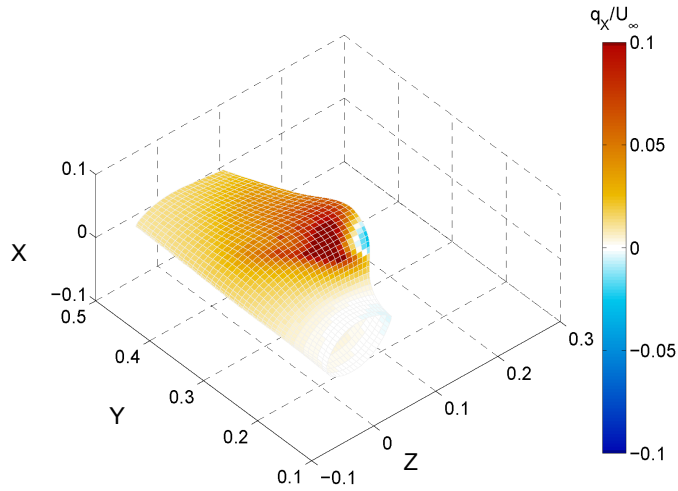


Figure 5.4: 45° slice of 3D visualization of dimensionless vorticity magnitude. Vorticity iso-surfaces at $\frac{|\omega|c_{max}}{U_\infty} = 2.1$, and 1.5.

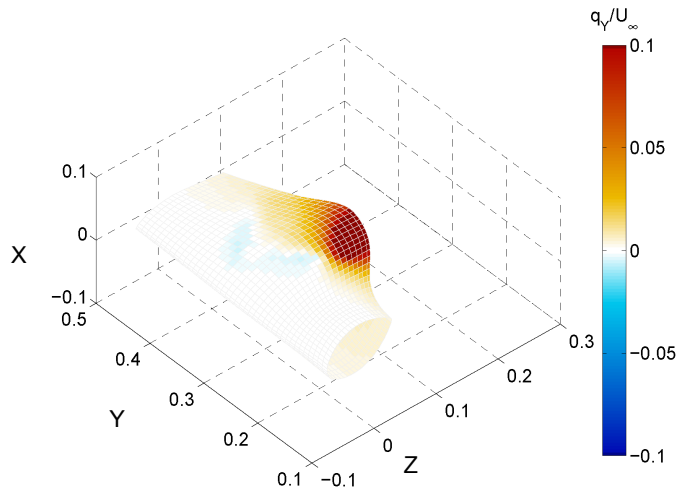
In Figures 5.5-b - 5.5-c, velocity directions on the blade suction surface carry the trace of the root vortex behavior. This can be noted with the changes in the velocity direction on the blade surface. In Figure 5.5-a, it is also observed that the velocity in the inflow direction is changing in chordwise direction due to the presence of the root vortex. This may cause some changes in the local airfoil characteristics.

Another important point related to the velocity induced by the root vortex is the magnitude of the velocity distributions on the suction surface of the blade, which reaches values around $0.1 \times U_\infty$. This proves that local airfoil characteristics are different from 2D characteristics. This led us to analyze the spanwise velocity in the inviscid-outer flow region.

It should be noted here that the following figures (Figure 5.5) show the induced velocities due to the vorticity present in a pie shaped part of the near wake directly behind the blade at the location of maximum chord (see Figure 5.4).

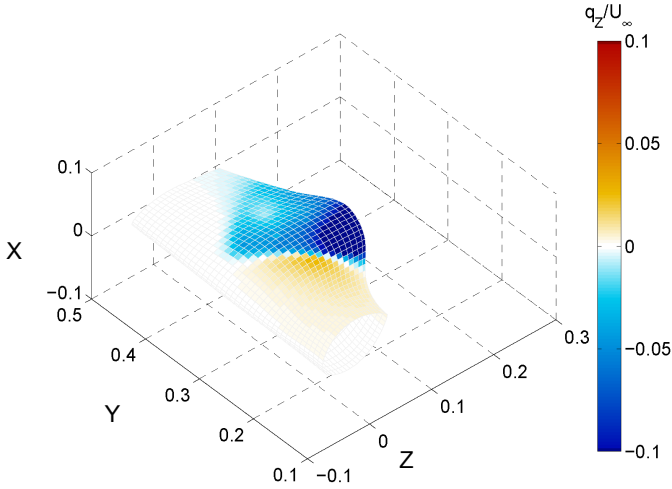


(a) Axial component.



(b) Spanwise component.

Figure 5.5: Three components of the dimensionless induced velocity distributions on the suction surface of the blade near the root.



(c) Chordwise component.

Figure 5.5: (continued) Three components of the dimensionless induced velocity distributions on the suction surface of the blade near the root.

5.3 Spanwise velocity in the inviscid-outer flow region

The analysis of the boundary layer of the blade of an HAWT has been performed by several researchers. Snel et al. (1994) performed an order of magnitude analysis of the terms in the boundary layer equations written for incompressible flow in cylindrical coordinates. They also discussed the inviscid outer flow region in their study and concluded that in this region, the scaling rules with respect to length and velocity are the same as in the attached flow region where $v = O(\Omega c)$, $\frac{v}{u} = O(\frac{c}{r})$. Moreover, the outer flow is assumed to be two dimensional for a high aspect ratio blade.

5.3.1 Spanwise velocity around the blade

In the present study, the velocity fields, obtained from the stereoscopic PIV measurements, are only available above the blade surface. The spanwise velo-

cities measured around Blade 1 at three different radial positions are presented in Figure 5.6. Looking to the spanwise velocity distributions around the blade, a very large outboard motion is observed in the trailing edge region especially at $r/R = 0.27$ and with smaller values at $r/R = 0.31$. This outboard directed flow is the boundary layer material emanated in the wake of the blade which also includes a trailing vorticity sheet. This flow behavior at these radial positions may be due to the result of rotation. It has already been mentioned in the previous studies that the radial flow in a rotating system has different characteristics than that in a stationary system (see Snel (1998), Du and Selig (2000), Hu et al. (2006)).

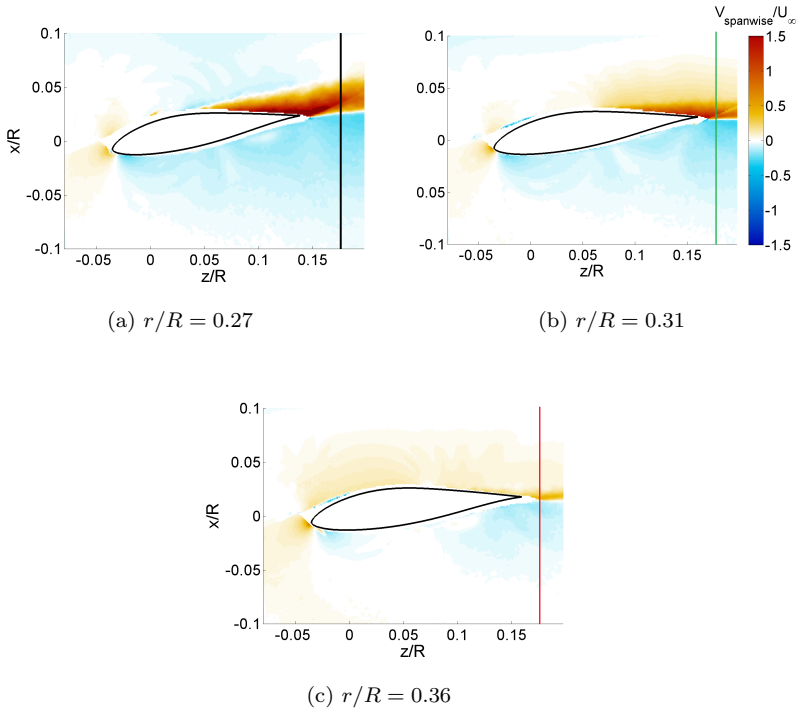


Figure 5.6: Dimensionless spanwise velocity distributions at three spanwise positions of **Blade 1**. Inflow is in $+x/R$ direction. Note that the data from PIV at $x/R = 0.025$ and $z/R = -0.05$ was masked due to reflection.

The separated flow in rotation does not move chordwise relative to the blade but has a radial motion. Lindenburg (2004) suggests that the radial flow in the separated flow region is mostly due to the centrifugal force and not due to the spanwise pressure gradient. He concludes that in the separated flow region the pressure near the trailing edge is close to the atmospheric pressure. This means that the chordwise pressure has a small spanwise gradient. Thus, the contribution of the small spanwise pressure gradient to the radial flow can be negligible compared to the effect of the centrifugal force. In the recent study of Herraes et al. (2016) also shows that the radial flow is due to centrifugal force but not due to pressure gradient. It is observed in Figure 5.7 that the surface pressure, presented by the limiting streamlines, does not show significant spanwise gradients.

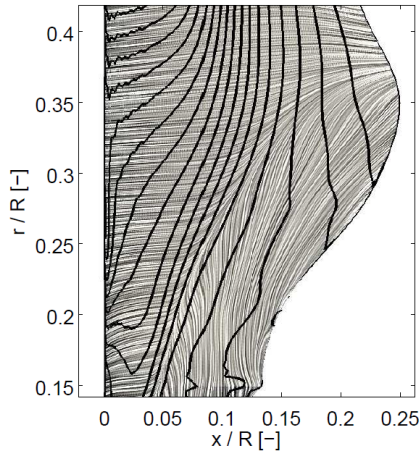


Figure 5.7: Isobars and limiting streamlines over the suction side of the blade root region. Figure is taken from Herraes et al. (2016).

Based on the previous observations, a study is performed to see whether the effects of rotation can also be determined above the blade surface. Spanwise velocities are plotted along the black line drawn at $z/R \cong 0.17$ as shown in Figure 5.6-a, at three different radial positions (see Figure 5.8).

In Figure 5.8, it is observed that there is an area with a large outboard oriented velocity behind the blade's trailing edge as seen at $r/R = 0.27$ and $r/R = 0.31$ and that the spanwise velocity area reduces furthermore outboard ($r/R = 0.36$). At more outboard radial positions (e.g. $r/R = 0.36$), it is

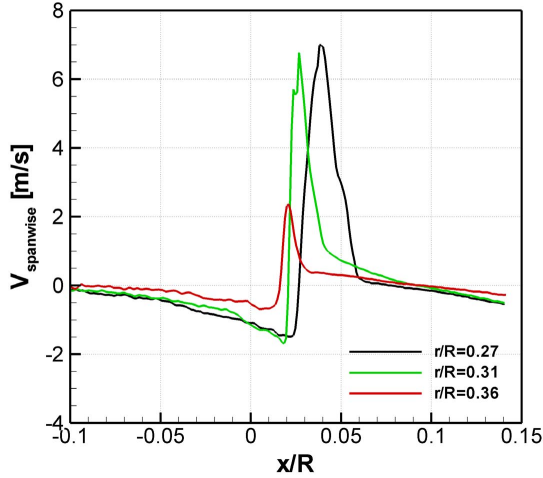


Figure 5.8: Spanwise velocity distributions along the lines shown in Figures 5.6, at $z/R \cong 0.17$ along x/R , at three radial positions.

observed that positive and negative spanwise velocities cancel each other. And finally starting from $r/R \cong 0.5$ to further outboard positions, the spanwise velocities in the upper and lower side of the airfoil become positive (outboard motion) which indicates the presence of the wake expansion, also close to the blade. However, further analysis may be required for better understanding of rotational effects in the outer flow region.

5.3.2 Spanwise velocity over the blade

To better analyze the spanwise velocity distribution over Blade 1, experimentally measured values of velocities are extracted above the blade surface at 39 spanwise positions (see Figure 5.9). In this way, the measured spanwise velocity distribution over the blade surface can be reconstructed. They are presented in Figure 5.10.

The experimental results show a positive spanwise velocity distribution in the region enclosed by $(Y, Z) = (0, 0)$; $(Y, Z) \cong (0.3, 0.01)$ and also in the trailing edge on the suction surface (see Figure 5.10-a). Besides, on the pressure surface, a negative spanwise velocity distribution is observed almost the

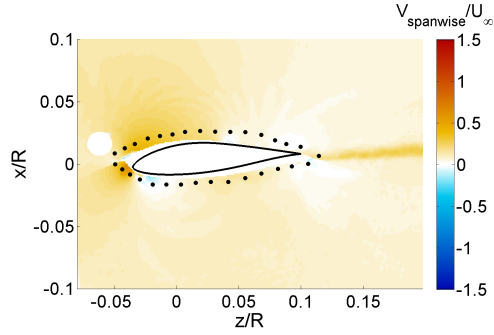


Figure 5.9: Extracted spanwise velocity points above the blade surface in the inertial frame of reference.

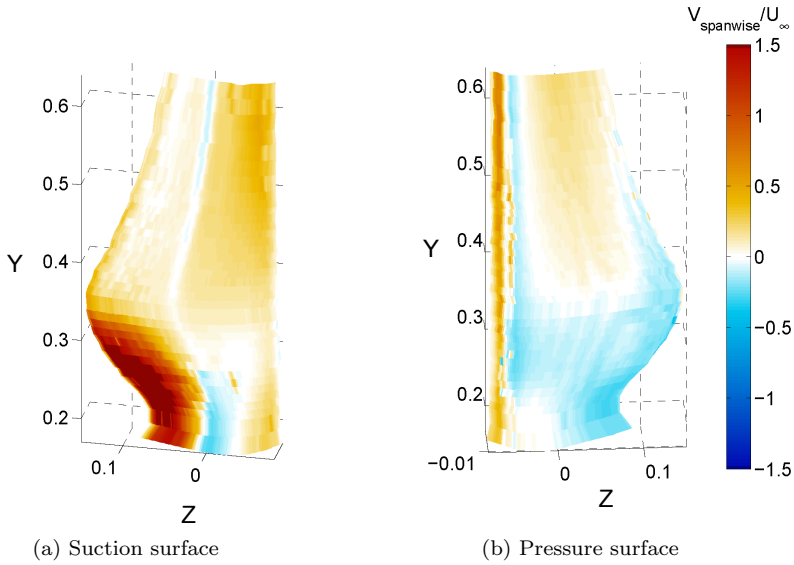


Figure 5.10: Dimensionless spanwise velocity component obtained above the blade surface from the PIV measurements in the inertial frame of reference.

complete blade root region up to $Y \cong 0.3$, except at the leading edge (see Figure 5.10-b). This flow behavior is due to the root vortex generated in this

region. Moreover, a line on the suction surface can be observed, which has zero velocity at around $Z \cong 0.01$ all along the blade surface (see Figure 5.10-a). The stagnation line on the pressure surface close to the leading edge ($Z \cong -0.0075$, along the span) is visible in Figure 5.10-b. It may be noted that near the stagnation line, the centrifugal effects will initiate a spanwise velocity at the blade surface which can be seen along the leading edge area in Figure 5.10-b. The outboard spanwise velocity enhanced after the maximum chord spanwise position (from $Y \cong 0.3$ towards the tip) on the suction and the pressure surfaces of the blade may be due to the flow expansion in the wake of the rotor.

5.4 Summary and chapter conclusions

This chapter focused on the role of the root vortex in the three dimensionality of the root flow, in particular the spanwise flow behavior in the inviscid flow region. For this purpose, stereoscopic PIV measurements on Blade 1 at $\lambda = 7$ were used as a base for the analysis.

First, an analysis is performed for the strength of the root vortex. The bound vorticity is calculated at several radial positions along Blade 1. The bound vorticity distribution along the blade radius shows a strong root vortex emanating from the maximum chord position of the blade.

After analyzing the bound vorticity distribution along the blade, the velocity induced by the root vortex over the suction surface of the blade is computed by using the Biot-Savart law. For this purpose, the velocity induced by a volume distribution of the root vorticity is calculated. This analysis shows that the computed induced velocities by the root vortex over the blade surface is rather low.

Furthermore, the spanwise velocity in the outer flow region is analyzed. The spanwise velocity distributions around the blade at $r/R = 0.27$ and $r/R = 0.31$ show significant (scale of U_∞) outboard velocities in the trailing edge which is the boundary layer material including the trailing vorticity sheet. This study shows the behaviour of the radial flow in the outer flow region.

The stagnation line on the pressure surface of the blade is visible from the spanwise velocity distribution in the outer flow region. Moreover, the effects of the root vortex are also visible through positive spanwise velocities on the suction surface and negative spanwise velocities on the pressure surface towards the trailing edge. Beyond the maximum chord spanwise position, there is an outboard spanwise velocity on both suction and pressure surfaces of the blade. The contribution of the spanwise flow on the blade loading will be analyzed in Chapter 6.

Based on the spanwise flow analysis on the blade, one may say that two-dimensional flow assumption applied in BEM method becomes more questionable for heavily loaded rotors since wake vorticity becomes stronger leading to increased spanwise flow and three-dimensionality.

Further analysis on the role of the root vortex in the blade flow is analyzed in the study of Herraes et al. (2016). In this study, the experimental results obtained by PIV are compared with more detailed CFD analysis. It is shown that the chordwise bound vorticity affects the radial flow distribution and the root vortex formation mechanism. Moreover, the formation of the two counter-rotating vortices in the trailing edge of the root region is believed to influence the wake evolution.

Chapter 6

Aerodynamic loads from PIV, BEM and CFD

In Chapter 5, the role of the root vortex and the resulting three dimensional flow are analyzed.

In the present chapter, we aim at answering two main questions: (i) Can CFD and BEM accurately predict the loads in the blade root region? (ii) What are the sources of discrepancies between the numerical and experimental results?

For this purpose, the experiments presented in Chapter 2 are simulated by both CFD and BEM methods. The loads along Blade 1 and Blade 2 obtained from CFD and BEM are compared with the experimental results. The results presented in this chapter are obtained through cooperation with other researchers.¹

1

CFD simulations were performed by Ivan Herraez Hernandez from the Carl von Ossietzky University of Oldenburg.

BEM calculations were performed by Ozlem Ceyhan from the Energy Research Center of the Netherlands.

Blade 1 load calculations were performed by Ye Zhang with the supervision of Daniele Ragni from TU Delft, Wind Energy Research Group.

Blade 2 load calculations were performed by Vanessa del Campo Gatell from the Universitat Politècnica de Catalunya with the supervision of Daniele Ragni from TU Delft, Wind Energy Research Group.

Chapter outline

- Section 6.1 describes the methodology for load calculation from PIV velocity fields.
- Section 6.2 provides the details of CFD simulations.
- Section 6.3 describes the BEM model including the corrections applied.
- Section 6.4 presents the load distributions along Blade 1 and Blade 2 obtained from PIV, CFD, and BEM. This section discusses the source of discrepancies in the load estimations. The 3C (three-components) velocity fields around the blade are also presented in this section.
- Section 6.5 discusses the key results of this chapter and draws the main conclusions.

6.1 Methodology for load calculation from PIV velocity fields

Determination of the correct rotor loads is an important step for an accurate structural and aerodynamic performance analysis of a wind turbine rotor. There are several methods experimentally estimate the aerodynamic loads. For example, in the NREL Unsteady Aerodynamic Experiment in the NASA-Ames wind tunnel, both strain gauges and surface pressures were used to obtain the loads along the blade (see Hand et al. (2001)). In the Model Experiments in Controlled Conditions (MEXICO), pressure sensors and strain gauges were used to measure loads (see Schepers and Snel (2007)).

In this section, an alternative approach to determine the loads along Blade 1 and Blade 2 is applied. This method builds a link between flow properties and load mechanisms by deriving the loads from the flow field information obtained by particle image velocimetry (PIV) (see Van Oudheusden et al. (2007)).

6.1.1 Estimation of forces by contour approach

The aerodynamic forces and moments on a body moving through a fluid are a result of the pressure and shear stress distributions on the surface of the body. The net effect of the pressure and the shear stress distributions over the complete surface of the body is the resultant force R , which can be split into components such as lift and drag or tangential and normal force components, and moment on the body (see Anderson Jr. (2001)).

In this section, a method is presented which estimates the loads on a body by calculating the momentum change in the fluid. The forces acting on an object can be calculated by using two different approaches. A common method is to use a stationary contour enclosing the moving object (see Figure 6.1-Left). An alternative approach is to use moving contour which has the same speed as the object velocity (see Figure 6.1-Right). This procedure allows for a statistical flow characterization where the flow can be assumed steady in the moving frame of reference. The force acting on a two-dimensional moving object is written as follows:

$$\mathbf{R} = - \oint\limits_{s(t)} \rho [(\mathbf{V} - \mathbf{V}_T) \cdot \mathbf{n}] (\mathbf{V} - \mathbf{V}_T) ds(t) + \oint\limits_{s(t)} (-p\mathbf{n} + \bar{\tau} \cdot \mathbf{n}) ds(t) \quad (6.1)$$

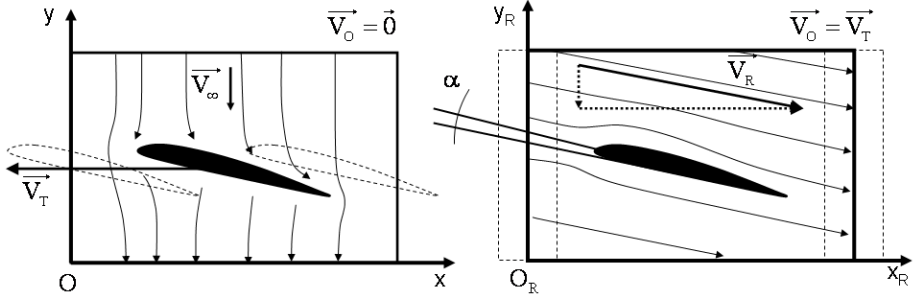


Figure 6.1: Velocity field representation. Stationary contour (Left) and moving contour (Right). Figure is taken from Ragni (2012).

In the case of a three dimensional rotating blade, the time derivative of the velocity fields can be eliminated if the flow is assumed quasi-steady in a moving frame of reference with a moving contour. The resultant force R can be evaluated as in Equation 6.2 with the contribution of Coriolis and centrifugal terms:

$$\begin{aligned} \mathbf{R} = & - \oint\limits_s \rho (\mathbf{V} \cdot \mathbf{n}) \mathbf{V} ds + \oint\limits_s (-p\mathbf{n} + \bar{\tau} \cdot \mathbf{n}) ds \\ & - \iiint\limits_v 2\rho (\boldsymbol{\Omega} \times \mathbf{V}) dv - \iiint\limits_v \rho (\boldsymbol{\Omega} \times (\boldsymbol{\Omega} \times \mathbf{r})) dv \end{aligned} \quad (6.2)$$

where v is the control volume and s its contour with the normal vector \mathbf{n} pointing outward, \mathbf{r} the distance from the center of rotation. The other variables are the relative velocity \mathbf{V} , the rotational velocity $\mathbf{\Omega}$, the pressure p , the flow density ρ , and the viscous stress $\boldsymbol{\tau}$.

The reader is referred to see Del Campo et al. (2013) and Ragni (2012) for a detailed explanation of the method used here.

6.1.2 Estimation of pressure

Van Oudheusden et al. (2007) presented two main approaches to obtain loads from PIV fields. The first one is the control volume approach which eliminates the pressure term (see Noca et al. (1999)). The second approach calculates the pressure term explicitly by using the momentum equation (see Unal et al. (1997)). The present study follows the second approach: the pressure gradient is derived from the momentum equation in its differential form by using the velocity field and its derivative. In the rotating frame of reference, the pressure gradient can be expressed by Equation 6.3 (see Del Campo et al. (2013)).

$$-\nabla p = \rho \frac{\partial \mathbf{V}}{\partial t} + \rho(\mathbf{V} \cdot \nabla) \mathbf{V} - \mu \nabla^2 \mathbf{V} - 2\rho(\mathbf{\Omega} \times \mathbf{V}) - \rho(\mathbf{\Omega} \times (\mathbf{\Omega} \times \mathbf{r})) \quad (6.3)$$

where \mathbf{V} is the relative velocity vector, $\mathbf{\Omega}$ is the rotational velocity, t is the time, μ is dynamic viscosity, ρ is the density and \mathbf{r} is the distance from the center of rotation.

The pressure can be evaluated from the spatial integration of the pressure gradient. For the evaluation of the integrated loads, obtaining the pressure on the selected contour suffices. Moreover, the pressure can be computed on the entire flow domain of interest by solving the Poisson equation as expressed in Equation 6.4 where g is a forcing function derived from the velocity field (Equations 6.5, 6.6) (see Ragni (2012)).

$$\nabla^2 p \approx p \cdot \mathbf{D} = g(u, v) \quad (6.4)$$

$$p = \mathbf{D}^{-1} g(u, v)$$

$$p \cdot \mathbf{D} = \left[\frac{p_{i,j+2} - 2p_{i,j} + p_{i,j-2}}{\Delta x^2} + \frac{p_{i+2,j} - 2p_{i,j} + p_{i-2,j}}{\Delta y^2} \right]_{i=1 \dots m, j=1 \dots n} \quad (6.5)$$

$$g(u, v)_{i,j} = \frac{\left[\frac{\partial p}{\partial x} \right]_{i,j+1} - \left[\frac{\partial p}{\partial x} \right]_{i,j-1}}{2\Delta x} + \frac{\left[\frac{\partial p}{\partial x} \right]_{i+1,j} - \left[\frac{\partial p}{\partial x} \right]_{i-1,j}}{2\Delta y} \quad (6.6)$$

Dirichlet and Neumann boundary conditions are applied in the present load computations at the boundaries of the measurement volume, including the region where the airfoil is masked (see Figure 6.2 labelled as *a*). A Neumann condition is used on the airfoil surface, imposing $\frac{\partial p}{\partial n} = 0$ where \vec{n} is the direction perpendicular to the airfoil surface. On the outer control volume (see Figure 6.2 labelled as *b*), in the regions where the flow can be considered irrotational, a Dirichlet condition is used, by obtaining the pressure from the Bernoulli theorem. In the wake region, a Neumann condition is imposed (see Figure 6.2 labelled as *c*).

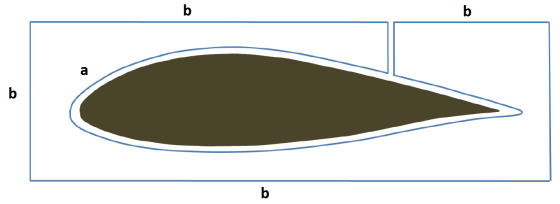


Figure 6.2: Boundary conditions of the measurement volume.

The effectiveness of the approach was affirmed in previous studies for different applications. Among others, Kurtulus et al. (2007) measured unsteady forces on a cylinder and Ragni et al. (2011) analyzed the aerodynamic loads on an aircraft propeller blade.

6.2 CFD Simulations

The open source CFD software package OpenFOAM is used to simulate the flow around the experimental wind turbine model in freestream using a steady-state RANS (Reynolds-Averaged Navier-Stokes) assumption. In RANS simulations, the governing equations are solved in ensemble-averaged form and the effect of turbulence on the average flow field is modeled with turbulence models. In this study, the Spalart-Allmaras turbulence model is used (see Spalart and Allmaras (1992)).

6.2.1 Numerical procedure

In the RANS simulations presented here, the discretization scheme for convective terms is a second order linear-upwind scheme. SIMPLE is used as the algorithm for the pressure-velocity coupling. This algorithm is an iterative procedure for solving equations for velocity and pressure for steady-state solutions (see OpenFOAM User Guide (2013)). Convergence is assumed to be reached when the residuals are stabilized and reach 10^{-5} . 240 cores are used for the computations.

6.2.2 Wall treatment and Boundary conditions

The standard wall functions are applied to the wall boundaries where the non-dimensional wall distance y^+ is 30 to 150.

Non-slip boundary conditions are applied for blades and nacelle. At the inlet, the Dirichlet boundary condition is applied for the inflow velocity and the Neumann boundary condition is applied for pressure. At the outlet, pressure is defined with the Dirichlet boundary condition as atmospheric pressure, and the Neumann boundary condition is applied for the outlet velocity.

6.2.3 Computational domain

The turbine geometry includes two blades and the nacelle. The tower is not meshed, since its influence on the rotor flow is assumed to be negligible. It is the case in the experiment that the tower is far from the rotor and hence from the field of interest. The shape of the domain is cylindrical, which has 34 m length and 22 m diameter, and contains a rounded square around the axis of rotation for achieving a homogeneous cell size in the region where the wind turbine is placed (see Figure 6.3).

The background mesh of the computational domain is created with a tool included in OpenFOAM called *blockMesh* (see OpenFOAM User Guide (2013)). The wind turbine itself is meshed with a tool called *FOAMproMESH* (see IconCFD (2013)). 5 layers of prism cells are added in the region of the boundary layer for obtaining high quality cells in that zone (see Figure 6.4). The first cell of the boundary layer has a height of 0.4 mm.

The total number of cells is 20 million, from which 99% are hexahedral and 1% are slip hexahedral. The quality of the mesh elements is checked by using the utility *checkMesh* in OpenFOAM before performing the simulations. The mesh is successively modified until all the quality criteria required by OpenFOAM are satisfied (see OpenFOAM User Guide (2013)).

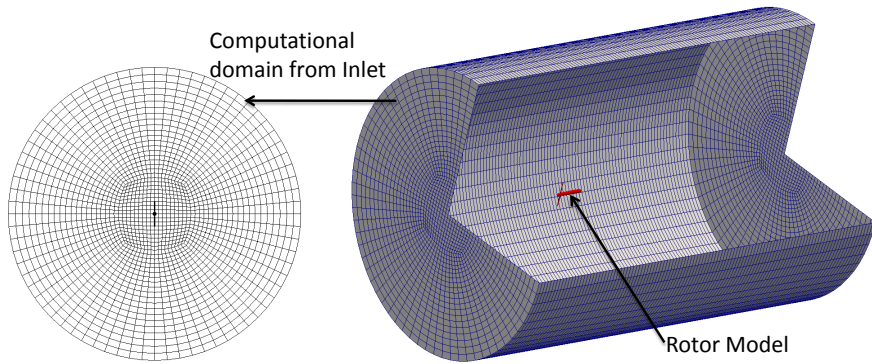


Figure 6.3: Computational domain with rotor model and a view from the Inlet.

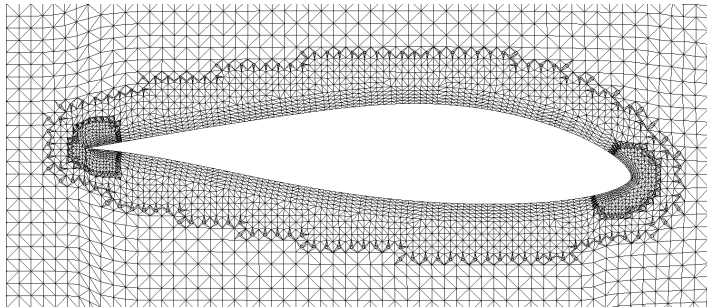


Figure 6.4: Computational domain close to the blade.

6.3 BEM calculations

The Blade Optimization Tool (BOT) of the Energy Research Center of the Netherlands (ECN) is used to model the experimental rotor (see Bot and Ceyhan (2011)). BOT can be used to calculate the stationary aerodynamic performance and loads of a wind turbine rotor using the blade element momentum (BEM) theory. An initial wind turbine blade design and 2D aerodynamic coefficients for the chosen airfoil are given as inputs.

6.3.1 Tip- and hub-loss corrections

There are two main elements for the accuracy of a BEM model applied in the root region of a blade. These are the hub-loss correction and the 3D correction (stall delay) model. While the stall delay model affects the three-dimensional aerodynamic performance of the airfoil, the hub-loss correction affects the induction distribution in the root region. Moreover, there is a tip-loss model which is applied in the tip region of the blade. In the BEM calculations presented here, corrections (stall delay and losses) are applied at the tip and at the root. A short description of these corrections in BOT will be given in the following paragraph.

The average pressure on the pressure surface of the blade is greater than that on the suction surface. Near the tip of the blade this pressure difference will cause some of the flow to attempt to migrate from pressure surface to the suction surface. At the same time, this flow is swept downstream, forming a trailing vortex from the tip and the root of each blade (see Munson et al. (2002)). The formation of a trailed vortex at the tip of each blade produces a high local inflow over the tip region and effectively reduces the lift and hence power production near the tip. This phenomenon is often called *tip loss* which is the effect of the finiteness of the blade. It presents a decrease in lift relative to the finite value of lift that would otherwise be produced without the influence of any tip vortices in the flow (i.e., a 2D flow assumption) (see Leishman (2000)). Several models have been introduced for including the effect of the tip loss. The most common one is the Prandtl tip-loss factor which does not take all the effects explained above into account, but only the effect of the limited number of blades.

In BOT, the Prandtl tip-loss factor (see Betz (1919)) is applied for both the induction factors as well as the mass flux through the annulus. When the maximum value of the induction factor at the blade is indicated by a , the average value can be defined as aF , with F the Prandtl tip correction factor, or loss factor (see Bot and Ceyhan (2011)).

A hub-loss factor is required at the root for the same reason as at the tip. Hence, in BOT, at the root a hub-loss factor, which is an identical implementation of the Prandtl tip-loss model, is used to describe the effect of the root vortex. Equation 6.7 presents the tip and hub-loss factor implemented in the present BEM calculations (see Bot and Ceyhan (2011)).

$$F = \frac{4}{\pi^2} \cos^{-1} \left[\exp \left(\frac{-N_b(R_{tip} - r)}{2r \sin \phi} \right) \right] \cdot \cos^{-1} \left[\exp \left(\frac{-N_b(r - R_{root})}{2r \sin \phi} \right) \right] \quad (6.7)$$

where N_b is the number of blades, r is the radial position, R_{tip} is the rotor tip radius, and R_{root} is the rotor root radius.

6.3.2 3D correction for rotational effects on the airfoil characteristics

As mentioned previously, one of the elements for improving the accuracy of a BEM model in the root region is the application of a 3D correction (stall delay) model. The 3D correction model applied in BOT is based on the work of Snel et al. (1993) (see Bot and Ceyhan (2011)). Snel et al. (1993) proposed a model by solving the simplified form of the 3D boundary layer equations in the rotating frame of reference. The simplified equations are obtained from an order of magnitude analysis of the boundary layer equations which enables the identification of the most relevant parameters. The equations are solved in an algorithm which imposes transition from laminar to turbulent flow. No correction was proposed for the drag coefficient. The correction model in BOT is applied only for the lift coefficient as in Equation 6.8.

$$Cl_{,3D} = Cl_{,2D} + \frac{3.1\lambda^2}{1+\lambda} G \left(\frac{c}{r}\right)^2 \left(\left. \frac{dCl}{d\alpha} \right|_{linear} \sin(\alpha - \alpha_0) - Cl_{,2D} \right) \quad (6.8)$$

where G is a factor that ensures a smooth transition to very high angles of attack where no correction is applied:

$$G = \left\{ \begin{array}{ll} 1 & , 0 < \alpha < 30 \\ \frac{1}{2} (1 + \cos(6\alpha - 180)) & , 30 < \alpha < 60 \\ 0 & , 60 < \alpha < 360 \end{array} \right\} \quad (6.9)$$

6.3.3 BEM simulations for the experimental rotors

The blade geometries used in BOT for BEM simulations are tabulated in Appendix A.6. They represent the geometries of Blade 1 and Blade 2 as used in the experiments. In all simulations, the hub radius is taken as 0.147 m which is the actual hub radius of the experimental rotors. As it can be seen in these tables, there is a cylindrical region (hub-blade connection part) and a transitional part to the DU96-W-180 airfoil. The airfoil starts at the radial

position $r/R = 0.2494$ in the simulations for Blade 1 and at $r/R = 0.2475$ in the simulations for Blade 2.

A modification had to be applied to the thickness distribution of Blade 2 in the hub-blade connection part. At the first six stations on Blade 2 (see Figure A.9), the thickness had to be modified from the real thickness distribution. If 18% thickness had been used for those sections, there would be a decreasing absolute thickness distribution at the root which is not desirable in BOT. Hence, this modification was performed in the input file of the geometry for Blade 2, to be able to run the BEM code (BOT).

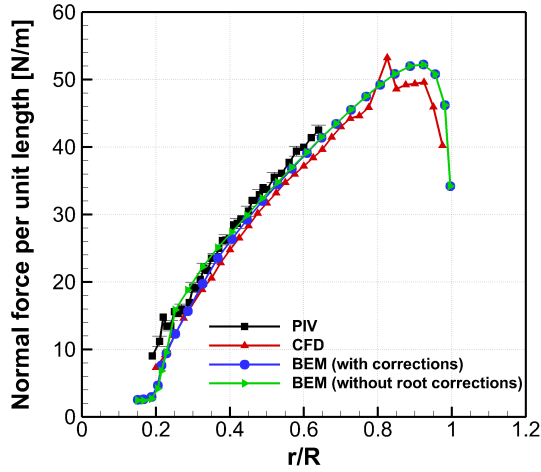
BEM simulations were performed with and without the corrections explained in BOT. The simulations are presented with two different titles. The calculations, which are performed by applying the Prandtl tip-loss correction, hub-loss correction and 3D boundary layer correction, are denoted as “BEM with corrections”. The presented results, which are called “BEM without root corrections”, are obtained by only including the Prandtl tip-loss correction.

6.4 Validation of CFD and BEM results with experimental loads

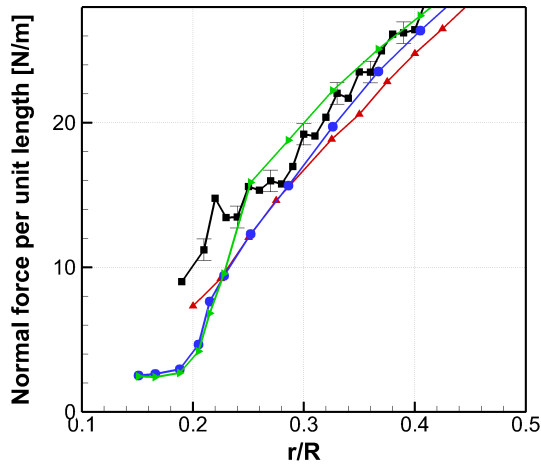
In this section, normal and tangential forces calculated by CFD and BEM are compared with the loads obtained from the analysis of the PIV data. First, the results for Blade 1 are analyzed by discussing the source of errors in predicting the loads. Next, three-component velocity fields around the airfoil obtained from PIV are presented and compared with the CFD results. Finally, experimental results for Blade 2 are also presented and compared with the simulations.

6.4.1 Blade 1: Normal force distribution

Figure 6.5 presents the normal force distributions along Blade 1. Here, normal force represents the direction perpendicular to the plane of rotation. Figure 6.5-b presents a close-up view of the normal force distributions in the root region of Blade 1. From the comparison of the normal force predictions, it can be noted that the experiments and the theoretical predictions match quite well although each method has its own inaccuracies. It is also observed that CFD deviates from the experiments all along the blade. This tendency is not observed for the BEM results. While CFD underestimates the normal force distribution along the blade, BEM predicts very close values to the PIV results.



(a) Normal force per unit length along the blade span.



(b) Zoomed-in at the root.

Figure 6.5: Normal force calculations for **Blade 1** obtained by different methods.

Uncertainties in BEM

The discrepancies between PIV and BEM load predictions can be due to errors in 2D airfoil data which are used as input in BEM calculations. Experimental 2D airfoil data at low Reynolds number are limited. Therefore, RFOIL is used to obtain 2D airfoil data for DU96-W-180 at the desired Reynolds numbers to be used as input in BEM calculations.

To have an idea about the performance of RFOIL in predicting airfoil data at low Reynolds number, we compare $C_l - \alpha$ (airfoil lift coefficient–angle of attack) distribution obtained from RFOIL with experimental data at $Re = 5 \times 10^5$ (see Figure A.10 in Appendix A.7).

The operating angle of attack range of the blade's sections shows that the blade experiences attached flow beyond $r/R = 0.25$. Hence, using RFOIL data in BEM calculations may not be an important source of error in load predictions from BEM. Still, it is important to note that Reynolds number distribution along the root region of Blade 1 is around $Re = 2.22 \times 10^5$ where the accuracy of RFOIL may be questionable.

The correction methods employed in the root region may be the reason of discrepancy. The corrections in BEM applied in the root region may not be suitable to reflect the real flow behavior in this region (see Breton et al. (2008) for the performance of 3D correction models). For example, using symmetric tip and hub loss distribution along the blade may not be entirely correct. This is because the losses at the tip and at the root depend on the blade circulation distribution which depends on the blade geometry and varies with operating conditions.

Uncertainties in CFD

Besides the sources of uncertainty that CFD holds as a numerical approach, there may be some other uncertainties while obtaining the loads from CFD simulations. A jump in the normal force distribution at Blade 1 at $r/R = 0.8$ is clearly seen in Figure 6.5-a. The reason of such a result can be due to interpolation errors while calculating the pressure from the unstructured grid. This may be called a method error while obtaining the loads from CFD simulations, rather than an error in the CFD simulation itself.

When BEM and CFD are compared (see Figure 6.6), it can be observed that CFD underestimates the normal force all along the blade compared to BEM without root corrections. Nevertheless, BEM with root corrections matches with CFD in the root region. This result may indicate that the root corrections (3D and hub-loss corrections) applied in BEM are tuned by CFD results.

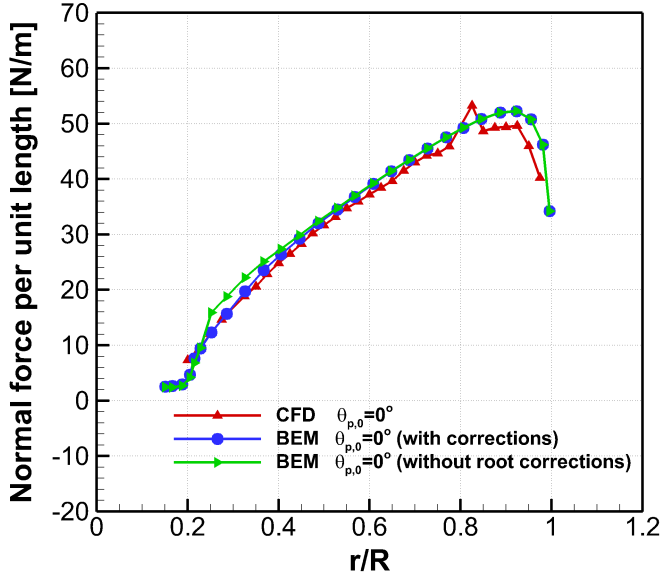


Figure 6.6: Normal force calculations for **Blade 1** predicted by **BEM** and **CFD**.

Experimental uncertainties in PIV measurements

The experiments are performed at freestream velocity $U_\infty = 6$ m/s, blade rotational speed $\Omega = 400$ RPM and the fixed pitch position of the blade is set to zero (chord perpendicular to axial direction) at the blade tip.

Sources of experimental uncertainties may cause higher/lower normal force distribution along the blade. These sources can be listed as follows:

1. inaccuracies in the freestream velocity of the wind tunnel,
2. inaccuracies in the rotational velocity,
3. movement of the traverse system (inaccuracies in the position of the PIV field of view),
4. inaccuracies in the blade pitch setting angle.

The uncertainty in the actual freestream velocity is estimated to be 0.5% of

the designated wind tunnel freestream velocity (private communication Timmer (2013)).

Rotational velocity of the rotor may be counted as one of the important sources of the uncertainty in the normal force distribution from PIV. However, it is observed that the uncertainty of the rotational speed amount 0.25% of the rotational speed ($\Omega = 400RPM$) during the experiments.

An uncertainty in the movement of the traverse system may cause a shift in the measurements. The accuracy of the traverse system was tested and found to be in between 0.01 and 0.03 mm (private communication Bernardy (2013)).

Moreover, one may see a summary of the most relevant uncertainties and their estimated effects on the spanwise PIV velocity fields in Table A.4 and Table A.5.

As mentioned in Section 2.6, it was noted during the experiment that there may be an uncertainty in the pitch angle of the blade due to the procedure to set the pitch angle. Therefore, to further evaluate whether there might be a pitch angle error in the measurements or not, we performed BEM calculations at different pitch angles and compared the results with the PIV results (see Figure 6.7). From this comparison, it is observed that PIV results seem to be most closest to the BEM results for $\theta_{p,0} = -1^\circ$. However, it should also be noted that the distributions at $\theta_{p,0} = 0^\circ$, $\theta_{p,0} = -1^\circ$ and $\theta_{p,0} = -2^\circ$ are not very different. Therefore, it is difficult to conclude that PIV data has a pitch angle error. A first tentative conclusion may be drawn at this point that a slight deviation up to -1% might explain observed differences in the normal force distribution. Moreover, it is also important to mention again that in this evaluation, we are using BEM computations which have their own uncertainties.

6.4.2 Blade 1: Tangential force distribution

Figure 6.8 presents the tangential force distributions along Blade 1. Generally, it is difficult to measure and correctly estimate the tangential force. High experimental accuracy is required to evaluate drag.

The tangential force distribution on Blade 1 obtained from PIV measurements shows large fluctuations which can be attributed to noise included in the PIV data. This may be due to rounded geometry in the root region of this blade.

A bump in both the CFD-predicted normal and tangential force distributions at $r/R = 0.8$ is noted. This observation supports the hypothesis about the error in the method to obtain the loads from CFD simulations, mentioned in the previous section.

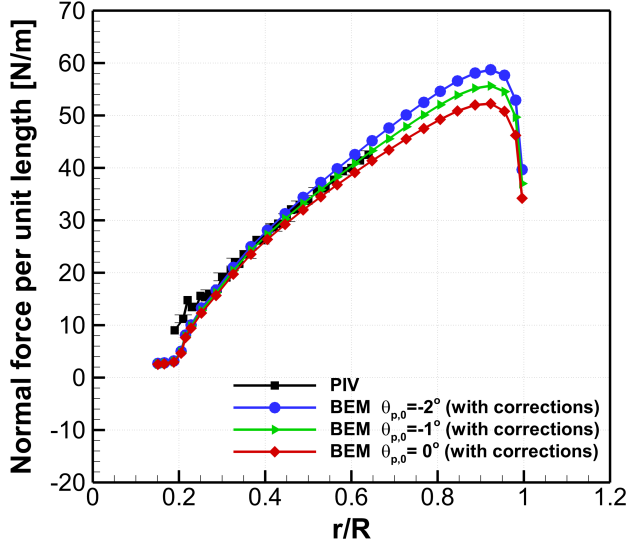


Figure 6.7: Normal force calculations for **Blade 1** at different blade pitch angles, $\theta_{p,0}$.

The chord distribution of Blade 1 is also shown in Figure 6.9 as a reference for the blade shape.

It seems that the tangential forces derived from experimental results show a more pronounced pattern than the numerical methods. Hence, a firm conclusion can not be drawn due to the inaccuracies in the experimental tangential forces.

6.4.3 Flow field around Blade 1: PIV vs. CFD

In this section, the PIV results are compared with the CFD results at $\theta_{p,0} = 0^\circ$ blade pitch angle.

Figures 6.10, 6.11, and 6.12 present velocity distributions around the blade sections in axial, tangential and spanwise directions. PIV velocity fields are obtained from chordwise measurements. As it can be seen in the PIV results, at some regions close to the airfoil, velocity data cannot be retrieved due to

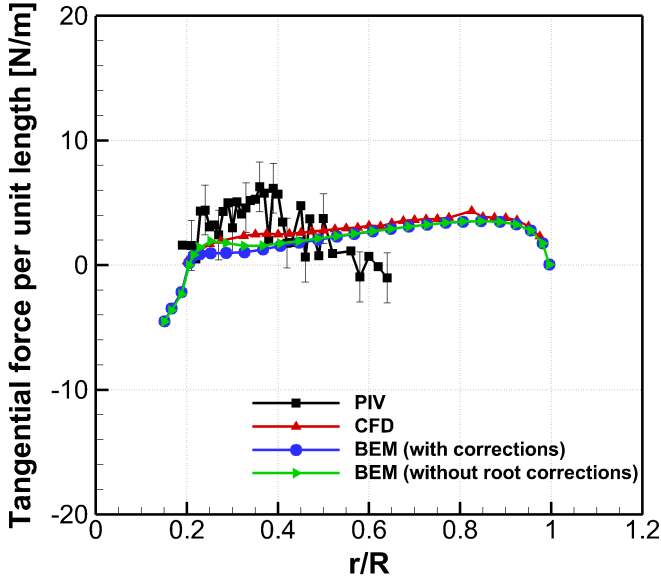


Figure 6.8: Tangential force calculations for **Blade 1** predicted by different methods.

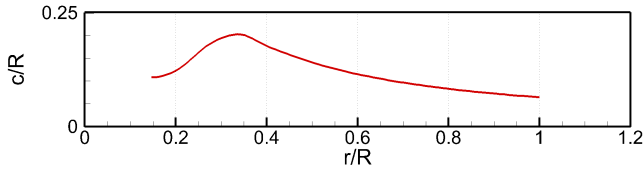


Figure 6.9: Chord distribution of **Blade 1**.

reflections from the surfaces. This is more visible in the leading edge where the regions are masked around $x/R = 0.025$ and $z/R = -0.05$. Because of this reason, at some radial positions it is impossible to observe the flow behaviour on the blade surface.

The Reynolds number of the sections presented here varies from $Re =$

1.44×10^5 to $Re = 2.22 \times 10^5$.

Axial velocity

Figure 6.10 presents the axial velocity distributions around the blade at three different spanwise positions. As expected from the axial velocity distributions, higher velocity areas on the leading edge decrease from mid-board ($r/R = 0.52$) to root sections ($r/R = 0.25$). Lower velocity areas are seen on the pressure side (windward side) of the blade.

Despite the overall good agreement between PIV and CFD axial velocity distributions, some higher axial velocity values are observed in the CFD results. This can be seen in Figure 6.10-f with the smaller negative axial velocity region on the suction surface towards trailing edge ($z/R \cong 0.025 - 0.1$). This discrepancy is first attributed to the uncertainty in the setting of the pitch angle of the blades which might have occurred in the experiments. To verify this hypothesis, additional CFD and BEM simulations were performed. BEM simulations with different blade pitch angles have already been shown in Section 6.7. Similar to the previous evaluation, additional CFD simulations were performed at the blade pitch angles $\theta_{p,0} = -1^\circ$ and $\theta_{p,0} = +1^\circ$. The velocities and the vorticity distributions of these three blade pitch angles ($\theta_{p,0} = -1^\circ, 0^\circ, -1^\circ$) were compared and showed similar flow properties (see Figure A.12). Hence, it can be concluded that such a small uncertainty in the pitch angle does not result in different flow phenomena.

Tangential velocity

Figure 6.11 presents tangential velocities around the blade at three spanwise positions ($r/R = 0.25$, $r/R = 0.34$ and $r/R = 0.52$). Tangential velocities around the airfoil at all the spanwise positions presented here also reach the value of freestream velocity and even amount beyond freestream velocity at $r/R = 0.52$. High tangential velocities are found in the root region. Rather high negative tangential velocity areas are noted at the trailing edge of the airfoil which represents the boundary layer material. This is initially dragged by the airfoil and afterwards shed in the free flow of the trailing edge. The trailing vorticity sheets are hidden in this boundary layer material. The negative tangential velocities on the suction side of the airfoil towards the trailing edge may be an indication of separated flow regions. Moreover, the tangential velocity on the suction side is increasing from root ($r/R = 0.25$) to outboard ($r/R = 0.52$) sections of the blade. This shows the increase of lift towards the outboard portion of the blade.

The comparison of PIV and CFD tangential velocity distributions shows very good agreement.

Spanwise velocity

Figure 6.12 presents spanwise velocity distributions around the blade at three spanwise positions ($r/R = 0.25$, $r/R = 0.34$ and $r/R = 0.52$). At $r/R = 0.25$ and $r/R = 0.34$, on the pressure side, an inboard spanwise velocity is observed with a maximum $0.3 \times U_\infty$ at $r/R = 0.25$, and $0.1 \times U_\infty$ at $r/R = 0.34$. By contrast, on the suction side of the airfoil at $r/R = 0.34$ and $r/R = 0.52$, the spanwise flow is directed outboards. This may be an indication of flow expansion.

Rotation has two main effects on the behaviour of the flow around the blade. First, it causes centrifugal and Coriolis forces. Second, it results in dynamic pressure along the blade which increases towards the tip of the blade due to an increase in relative velocity. A radial velocity component is expected to be seen in the flow which is a result of centrifugal forces and the varying dynamic pressure along the blade. As a result of varying dynamic pressure a spanwise pressure gradient occurs and accelerates the flow to the lower pressure and thus higher radial positions (see Lindenburg (2004)). Moreover, as it was already shown in Section 5.3.2 (see Figure 5.10), the root vortex may cause a spanwise velocity component over the blade in the root region.

Based on the explanation mentioned above, it is seen that the boundary layer flow, which also includes trailing vorticity sheet, has a fairly large outboard spanwise component at $r/R = 0.25$. The region where higher outboard spanwise velocities are observed coincides with the boundary layer flow already shown in the tangential velocity distributions which can be an indication of flow separation. The interaction between the separated boundary layer flow and the outer flow can clearly be observed. It can be concluded that the development of the boundary layer is hence different from a boundary layer on an airfoil at the same Reynolds number.

Although only the flow above the blade surface can be presented in this study, as was mentioned in the previous paragraph, the boundary layer flow can also be observed at $r/R = 0.25$. The radial motion of the separated flow in this region is expected to contribute to an increase of the lift force and also to affect the behavior of the boundary layer (see Breton (2008)). In the inviscid flow region, the spanwise flow, which is a result of the spanwise pressure gradient, can contribute to the blade loading. From the PIV results in the root region, it is observed that the spanwise velocities are relatively high close to the trailing edge region on the suction surface. This can also be observed in the

reconstructed spanwise velocity distribution presented in the previous chapter (see Figure 5.10). Hence, high spanwise velocities in this region may cause a high dynamic pressure distribution along the blade, and may contribute to the blade loading.

The comparison of CFD with experimental results shows better agreement at $r/R = 0.34$ and $r/R = 0.52$ than at $r/R = 0.25$. Especially on the suction side of the airfoil at $r/R = 0.25$, CFD estimates outboard spanwise flow, while PIV shows some inboard motion. It is known that CFD has some difficulties to correctly simulate the separated flow regions. Hence, at this position $r/R = 0.25$, it is expected to see that the simulations may have difficulties to accurately capture radial flows.

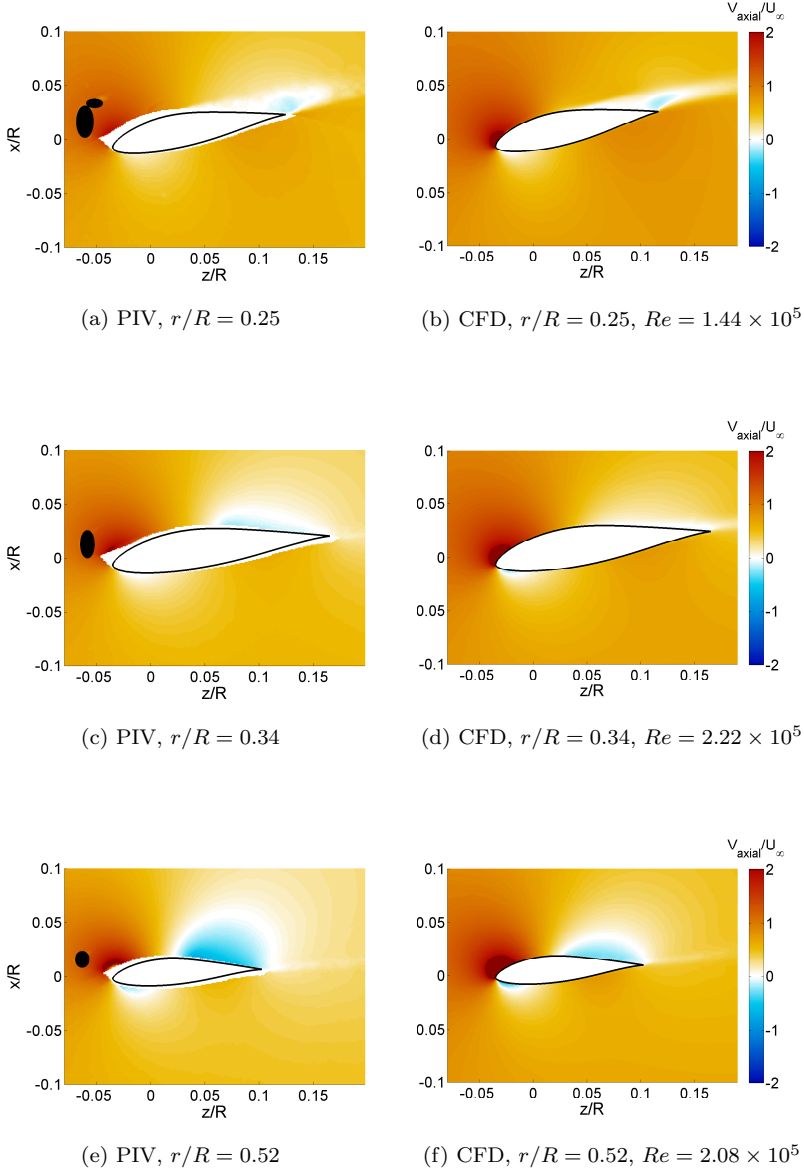


Figure 6.10: Dimensionless **axial** velocity distributions for **Blade 1** at three spanwise positions. Left column PIV, right column CFD. Inflow is in $+x/R$ direction. Note that the area at $x/R = 0.025$ and $z/R = -0.05$ in PIV data was masked due to reflection.

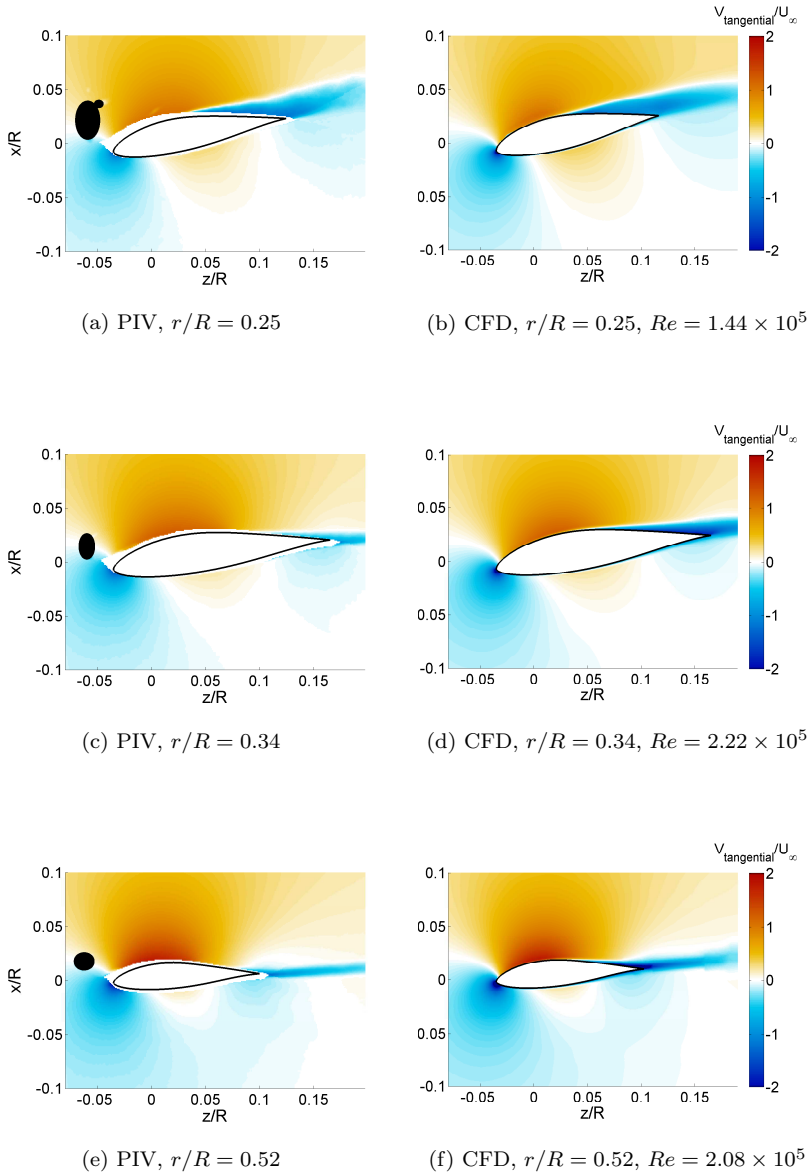


Figure 6.11: Dimensionless **tangential** velocity distributions for **Blade 1** at three spanwise positions. Left column PIV, right column CFD. Inflow is in $+x/R$ direction. Note that the area at $x/R = 0.025$ and $z/R = -0.05$ in PIV data was masked due to reflection.

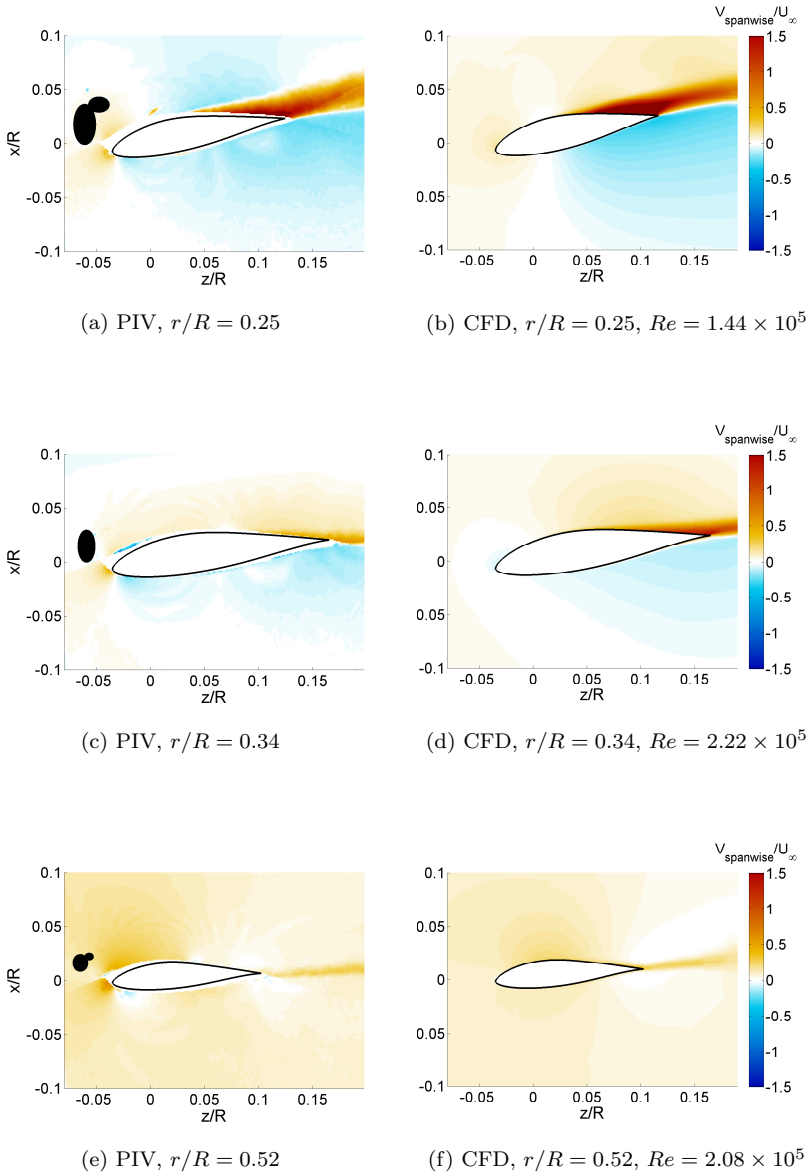


Figure 6.12: Dimensionless **spanwise** velocity distributions for **Blade 1** at three spanwise positions. Left column PIV, right column CFD. Inflow is in $+x/R$ direction. Note that the area at $x/R = 0.025$ and $z/R = -0.05$ in PIV data was masked due to reflection.

6.4.4 Blade 2: Normal force distribution

Figure 6.13 presents the normal force distributions along Blade 2 obtained from PIV, CFD and BEM. Figure 6.13-b presents a close view of the normal force distribution in the root region of Blade 2. There is a very good agreement between the numerical simulations and PIV in the mid-board region ($r/R \cong 0.4 - r/R \cong 0.8$) of the blade.

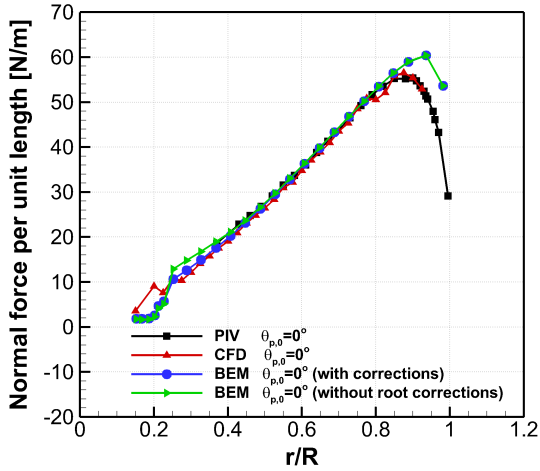
In Figure 6.13-b, it is observed that CFD underestimates the normal force distribution between $r/R \cong 2.25$ and $r/R \cong 0.4$. The jump at $r/R \cong 0.8$ seen in the normal and tangential force distributions for Blade 1 is also visible in the CFD results as a drop (see Figure 6.13-a). There is a jump at $r/R \cong 0.2$ which can also be due to interpolation errors while calculating the pressure on the unstructured grid. When the shear stress over the blade is analyzed, there is no indication which may cause such a force distribution at those radial positions ($r/R \cong 0.2$ and $r/R \cong 0.8$).

Similarly to the normal force distribution for Blade 1 obtained from BEM and CFD (see Figure 6.6), it is observed between $r/R = 0.25$ and $r/R = 0.4$ that BEM with corrections matches better with CFD than BEM without root corrections (see Figure 6.13-b). This result supports the previously mentioned assumption in the load analysis for Blade 1, that BEM root corrections are calibrated by CFD results.

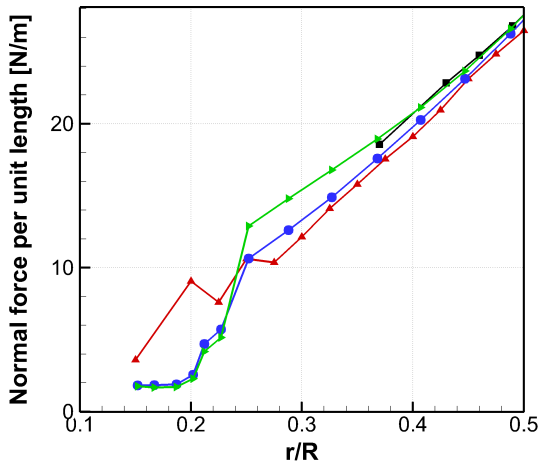
6.4.5 Blade 2: Tangential force distribution

Figure 6.14 presents the tangential force distributions along Blade 2. The chord distribution of Blade 2 is also shown in Figure 6.15 as reference for the blade shape.

From the comparison of the tangential force distributions of the numerical simulations and the experiments, it is observed that PIV results show a higher tangential force distribution along the blade until $r/R = 0.8$ from the root. This may be because the procedure to obtain the forces from the PIV velocity measurements does not explicitly take into account the wall shear stresses on the blade surface (refer to Section 6.1.1). However, in BEM and OpenFoam simulations wall shear stresses as well as the pressure drag due to separation are taken into account. Hence, this leads to a lower values of the tangential force.



(a) Normal force per unit length along the blade span.



(b) Zoomed-in to the root.

Figure 6.13: Normal force calculations for **Blade 2** obtained by different methods.

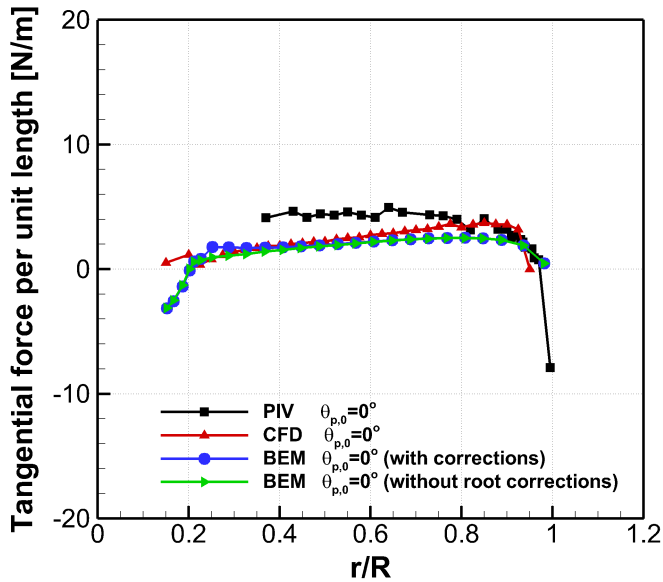


Figure 6.14: Tangential force calculations for **Blade 2** obtained by different methods.

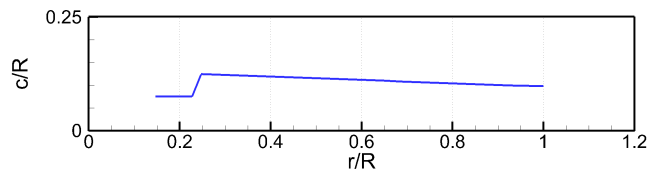


Figure 6.15: Chord distribution **Blade 2**.

6.4.6 Comparisons of load predictions: Blade 1 and 2

From the aerodynamic load comparisons, it was observed that PIV results differ from the numerical simulations more for Blade 1 than for Blade 2. This may be because of the pitch angle difference between the numerical simulations and the PIV measurements for Blade 1.

In Figures 6.9, and 6.15, the chord distributions along Blade 1 and Blade 2 are presented. A high c/r distribution is noted in the root region of Blade 1. It has already been mentioned that c/r can be the triggering parameter for the three dimensionality of the flow in the root region. On the contrary, Blade 2 has a more rectangular shape which results in attached flow over the blade. Hence, different flow characteristics occur around Blade 1 and Blade 2 due to different design aims. Therefore, the performance of the numerical simulations for predicting the loads may differ for each blade. For example, it is well known that the BEM method is based on 2D airfoil data which has to be corrected for three dimensionality of the flow. While it is expected to see more deviation of BEM simulations for the load distributions on Blade 1, BEM may result in better predictions for the load distributions on Blade 2.

Moreover, there are some simulation challenges in CFD which may affect the prediction of loads from CFD. For example, it is easier to mesh Blade 2 than Blade 1 when the computational domain is created by a structured mesh approach. In the present study, to overcome this problem for Blade 1, an unstructured mesh domain is used which may lead to some difficulties when computing the pressure from the unstructured grid. Furthermore, RANS simulations have some difficulties to accurately capture the separated flow region. Hence, the effect of radial flow on the loading of Blade 1 may not be accurately predicted by CFD. And thus it is more challenging to calculate the loads on Blade 1.

A detailed comparison of the normal force predictions for Blade 1 (see Figure 6.6) and Blade 2 (see Figure 6.13), obtained from BEM and CFD, shows that between $r/R \cong 0.35 - r/R \cong 0.75$ the numerical simulations differ from each other more for Blade 1 than for Blade 2. This is also noted in the tangential force distributions of Blade 1 (see Figure 6.8) and Blade 2 (see Figure 6.14). While the tangential force predictions using BEM and CFD are very close to each other between $r/R \cong 0.3$ and $r/R \cong 0.5$ along Blade 2, they deviate from each other at the most in that region for Blade 1. This is the region where Blade 1 has the largest c/r distribution which may be the triggering parameter for three dimensional flow.

6.5 Summary and chapter conclusions

In this chapter, the aerodynamic loads along Blade 1 and Blade 2 are predicted by BEM and CFD and are validated with the experimental loads. Additionally, the experimental (PIV) velocity distributions for Blade 1 are presented and compared with CFD results.

The experimental normal force distribution for Blade 1 is very close to the BEM and CFD results. From the analysis of BEM simulations with different blade pitch angles, of raw PIV images, and of velocity distributions around the blade sections, it may be concluded that the pitch angle in the experiment might be closer to $\theta_{p,0} \cong -1^\circ$. This would then also be a probable reason for the fact the forces obtained from PIV are slightly higher than the BEM and the CFD results.

The corrections (hub-loss and 3D corrections) in BEM applied in the root region may not be suitable to reflect the real flow physics in this region. For example, the hub-loss factor is a similar application of the Prandtl tip loss factor which gives a symmetric tip and hub loss factor distribution along the blade. This may not be correct because the losses depend on the blade geometry and the operating conditions.

Although it is mentioned in some previous studies that BEM method are not based on the detailed knowledge of rotor blade flow, in this study, the load predictions obtained by BEM calculations are fairly accurate in the region from mid-board to transition part (from a circular to an airfoil) of the blades. This shows that a BEM code validated with several different experimental results may accurately predict the loads.

Comparison between BEM (with and without root correction model) and CFD shows that, between $r/R = 0.25$ and $r/R = 0.4$, BEM with a root correction model matches better with CFD than BEM without root correction model. This suggests that BEM root corrections are tuned by the CFD results.

There are some unexpected jumps and drops in the CFD load predictions at radial positions around $r/R \cong 0.2$ and $r/R \cong 0.8$. This may come from the method to calculate the pressure on the unstructured grid rather than the CFD simulation itself.

When only the numerical simulations' predictions are compared for Blade 1 and Blade 2, it is observed that between $r/R \cong 0.35$ and $r/R \cong 0.75$, the numerical simulations differ from each other more for Blade 1 than for Blade 2. This is attributed to the geometrical differences of the blades.

The velocity fields comparisons between CFD and PIV show a very good agreement. Furthermore, more detailed comparison is performed in the recent CFD study of Herraes et al. (2016), shows an excellent agreement with the measurements.

Chapter 7

Conclusions and recommendations

7.1 Thesis Conclusions

In this thesis, the stereoscopic particle image velocimetry (PIV) technique has been chosen to investigate the aerodynamics of the root region of a horizontal axis wind turbine (HAWT).

The experimental results provide three components of velocity fields (i) in the near wake at different blade azimuth angles, (ii) in the cross-section of the blade at different radial positions. The experiments were performed for two blade geometries at different tip speed ratios. Moreover, the experimental results were also compared with the numerical results obtained from BEM and CFD simulations.

The key results and conclusions presented in this thesis are summarized by answering the research questions mentioned in the introduction.

How does the flow behave in the root region of a HAWT?

The analysis of the PIV results obtained from Blade 1 at $\lambda = 7$ showed:

- The presence of the root vortex and its evolution in the near wake region.
- A strong effect of the root vortex on the flow behavior in the blade's root region.
- High axial velocities in the inboard region along the nacelle.

- Axial velocities approaching the freestream value (beyond the expected axial velocities).
- Strong outboard and inboard radial motions in the near wake region as a consequence of the vorticity in the root region.
- Flow separation on the suction surface of the blade.

Two concentrated trailing vorticity regions were observed in the maximum chord and in the circular cross section of the blade. Unlike the observations in the literature, the root vortex emanating around the maximum chord position do not interact with the nacelle, but expanded in the outboard direction. However, the vorticity released from the inner part of the blade–hub connection is convected axially, staying in the vicinity of the nacelle.

Again, it should be noted that these conclusions are based on the analysis of Blade 1 at $\lambda = 7$, and may not be generally valid. Additional experiments were performed in an attempt to answer the following research questions.

Does the radial flow exist in the inviscid–outer flow region of a HAWT blade root?

PIV data were used to obtain the spanwise flow distribution over the blade. The analysis of the flow in the inviscid-outer flow region showed:

- Outboard spanwise velocities on the suction surface in the blade’s root region and inboard motion on the pressure surface. (This flow behavior may be due to the root vortex but the present analysis did not determine whether this hypothesis is correct or not.)
- Outboard spanwise velocities on both suction and pressure surfaces beyond the maximum chord position of the blade which can be attributed to the wake expansion.
- The influence of spanwise flow outside of the boundary layer.
- Very large outboard velocities at the trailing edge of the root region, which can be contributed to the rotational effects observed in the inviscid-outer flow part.

Moreover, based on this analysis, one may say that two–dimensional flow assumption applied in BEM method becomes more questionable for heavily loaded rotors since wake vorticity becomes stronger and leading to increased spanwise flow and three-dimensionality.

How are the blade wake, root vorticity and radial flow affected by the change of blade geometry and the tip speed ratio?

The experimental results from the measurements for Blade 1 at $\lambda = 7$, Blade 2 at $\lambda = 7$, and Blade 2 at $\lambda = 5$ showed:

- Changes in the radial flow behavior with different blade geometries.
- No remarkable difference in the radial flow behavior with change of tip speed ratio for the same blade geometry.
- Different wake formation for the three test cases.
- The dependency of the evolution and strength of the root vortex on the blade geometry and on the distribution of the circulation.

How well can CFD and BEM models simulate the observed flow phenomena around the blade root?

What are the sources of discrepancy between CFD and BEM simulation results and experimental results in predicting the blade aerodynamic loading?

The aerodynamic loads along Blade 1 and Blade 2 were predicted by BEM and CFD and validated with experimental results. Additionally, the experimental (PIV) velocity distributions for Blade 1 were compared with CFD results.

A very good agreement in the load predictions for blades was observed between measurements and the numerical methods. While CFD slightly underestimated the normal forces along the blades, BEM provided very good agreement with PIV. BEM predictions in the root region until the transition to a circular cross section were reasonably good.

The comparison between BEM and CFD results showed that, between $r/R = 0.25$ and $r/R = 0.4$, the root correction model (implemented in BOT) improves the agreement between BEM and CFD.

The flow field comparison between CFD and PIV results show a fairly good match.

The experimental measurement errors, the methods to retrieve the forces from the CFD and PIV data, and the correction models implemented in the BEM code can be counted as the main source of discrepancies of the methods used to predict the loads in this study.

7.2 Suggestions for future work

The present analysis on the horizontal axis wind turbine blade's root flow reveals more topics for further research. The scope of the present work may be extended by the following future work suggestions:

- Further analysis can be performed on the hub-loss model application in BEM codes. The application of the hub-loss factor which is a very similar implementation of the tip-loss factor may not be totally accurate in the root region. This is due to the geometrical shape in the root region which is different compared to the tip region, and causes a different circulation distribution.
- From the experimental point of view, the use of methods to extend the measurements to the regions where velocity could not be measured in the present set up (e.g. region close to the surface) already exist for 2D, stationary flows. The efforts can be made to extend this approach to 3D and rotational flows.

Appendix A

Appendix

A.1 Performed Experiments

The experiments performed during this study and the publications which employ the experimental results are presented in Table A.1

Table A.1: HAWT stereoscopic PIV experiments

Date	Operating condition	Publications
August 2009	Blade 1, $\lambda = 7$	Akay et al. (2010a), Akay et al. (2010b)
April 2010	Blade 1, $\lambda = 7$	Micallef et al. (2011), Akay et al. (2011), Micallef et al. (2012b), Micallef (2012)
April 2011	Blade 1, $\lambda = 7$	Akay et al. (2012a), Akay et al. (2012b), Akay et al. (2013), present thesis
February 2012	Blade 2, $\lambda = 7, 5$	Akay et al. (2012b), Micallef et al. (2012a), Micallef (2012), Del Campo et al. (2013), present thesis

A.2 Open jet facility (OJF)

OJF is a closed circuit wind tunnel which has 2.85m diameter octagonal jet exit. This wind tunnel has a test section $6\text{m} \times 6\text{m} \times 11\text{m}$ (width \times height \times length). The inflow velocity in the test section can reach up to 35m/s and the turbulence intensity of the tunnel in the inflow direction is relatively low, around 0.28%, and may vary depending on the operating speed. A schematic representation of the wind tunnel can be seen in Figure A.1

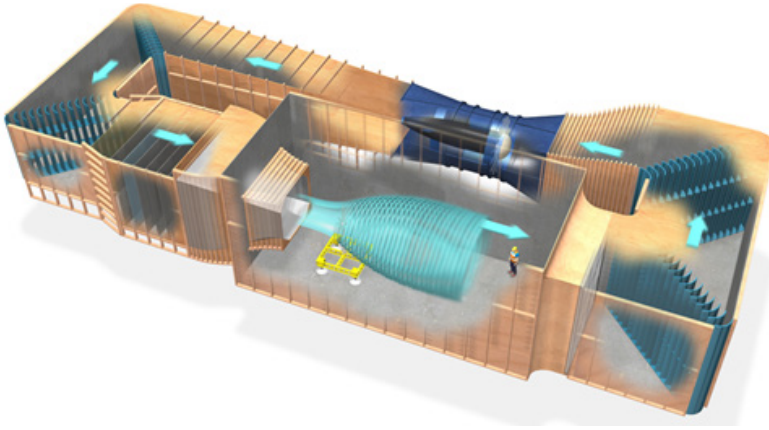


Figure A.1: Schematic representation of open jet facility at TU Delft.

A.3 Rotor Model

The wind turbine model is an advanced multi-functional measuring instrument which enables various types of studies. The design and manufacturing were carried out by DEMO, the University in house “workshop”. One of the aim of this wind turbine model design is to measure different types of blades. In the design of the wind turbine model, both measurements with 2 blades or 3 blades are considered. A close-view to the hub is given in Figure A.2. In Figure A.3, a schematic representation of the wind turbine model with two blades is shown.

The rotational speed of the rotor shaft is variable (from 0 – 20 Hz) and it can be set through the measurement program.

The following measurements are performed from the rotor axis:

- Axial force exerted on the rotor shaft through the rotor blades,
- Tangential torque exerted on the rotor shaft through the rotor blades,
- Position of the rotor blades,
- Azimuthal position of the rotor,
- Zero position of the rotor.

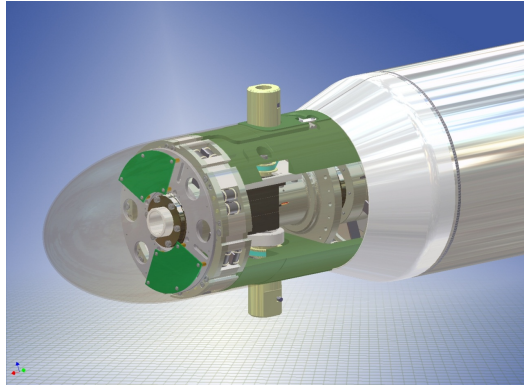


Figure A.2: Close view to the hub.

A.3.1 Force measurements

An essential component of the wind tunnel model is the "torque-axial" forces meter. This unit measures both the axial force and torque acting on the rotor shaft. In total, there are two force gauge units mounted in series (one after the other on the end of the rotor axis, space in the nose cone). Important to note that there is no interaction between the axial and radial loads. This is called cross-talk between the two load components. The measurement of these two components is carried out by means of strain gauges which are arranged on measuring springs. There are 4 radial and 4 axial measuring springs are used. Both the axial and radial components can be measured, the maximum deflection (mechanically) is 2.5 mm in both directions (this is against the spring force). A close view of the measuring springs where the strain gauges are arranged can be seen in Figure A.4.

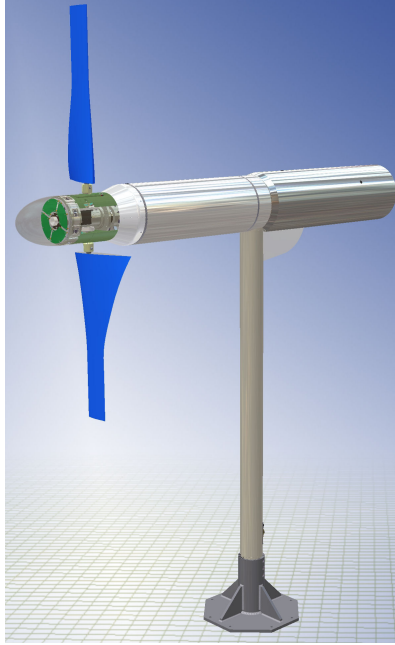


Figure A.3: Schematic representation of rotor model with another set of blades.

A.4 PIV system apparatus

After the measurement setup is built, the PIV system needs to be calibrated for the 3D PIV measurements. Cameras are calibrated by using a calibration plate and the LaVision DaVis[®] software wizard.

The magnification factor needs to be identified through the calibration. A common approach to calibrating a stereo PIV imaging setup relies on images of planar calibration targets which are placed coincident with the light sheet plane. These calibration targets typically consist of a precise grid of markers (dots, crosses, line grid, checker board) that are easily detected with simple image processing techniques. A single image of planar calibration marks is then sufficient to calculate adequate mappings between image space and object space, but it generally does not provide information on the camera viewing angles that are essential for reconstruction of the three-component displacement vector. This important parameter can only be calculated from a set of image-

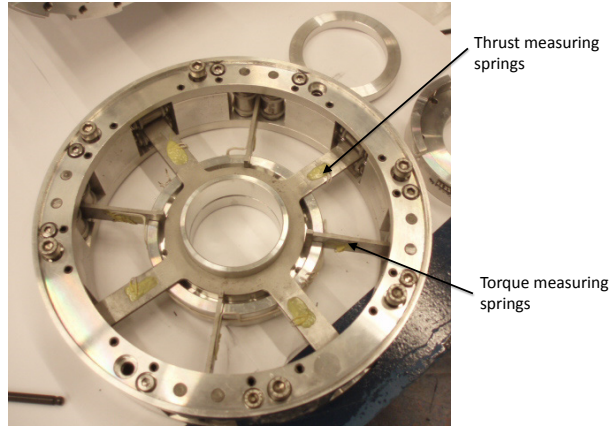


Figure A.4: Measuring springs where the strain gauges are fixed.

to-object correspondence points that are not coplanar. A method is to use multi-level calibration targets that have reference markers at different heights (Figure A.5, see Raffel et al. (2007)).

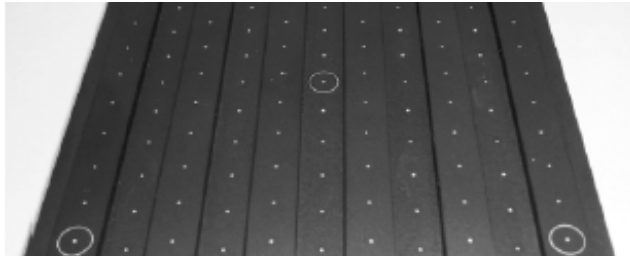


Figure A.5: Precision-machined twin level calibration target with dot pattern for stereo PIV calibration. Levels are separated by 2mm, dots are equally spaced on a 10mm grid. Figure is taken from Raffel et al. (2007).

After using the software wizard for the calibration, the field of view in the tests was found to be $290\text{mm} \times 199\text{mm}$.

Moreover, self-calibration is also performed after the data acquisition by means of another LaVision DaVis[®] software wizard. The purpose of the self-calibration process is to eliminate any misalignment between the calibration

plate and the laser sheet.

The flow was seeded with fog particles generated by a SAFEX Twin Fog generator using the SAFEX-Inside-Nebel fluid, a water soluble fog fluid, producing seeding particles with approximately 1 micron median diameter. Seeding was given in the downstream of the measurement area. Hence, a homogenous mixture of the seeding in the flow was obtained in the test room.

The field of view (FOV) was illuminated by double cavity pulsed Nd:YAG laser. The laser sheet had $\sim 3\text{mm}$ thickness at the FOV. Two 16 MPix cameras with 180mm lenses were used to capture the FOV at an aperture $f\#$ of 5.6 with tilt-lens Scheimpflug and Solidor adaptors at approximately 1.2 m, with a relative angle of about 40° . To obtain phase-locked measurements, the timing of the laser and cameras is controlled by a trigger signal which is set by the user at the required position of the blade.

The PIV data were acquired with LaVision Davis[®] 7.2 and evaluated with LaVision Davis[®] 7.4 software. The PIV apparatus are summarized in Table A.2 and measurement details are presented in Table A.3.

Table A.2: PIV apparatus

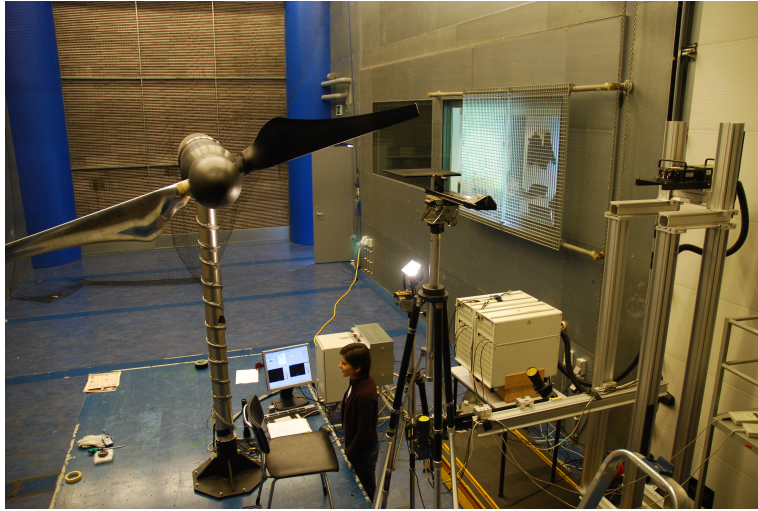
Seeding	SAFEX-Inside-Nebelfluid
Particle size	1 micron median diameter
Laser	Nd-Yag
Laser sheet thickness	3mm
Camera	Lavision Image Pro LX
Camera resolution	16 Mega pixel
Lens	Nikon
focal length 180 mm	$f\#$ 5.6

Table A.3: PIV setup parameters for spanwise measurements.

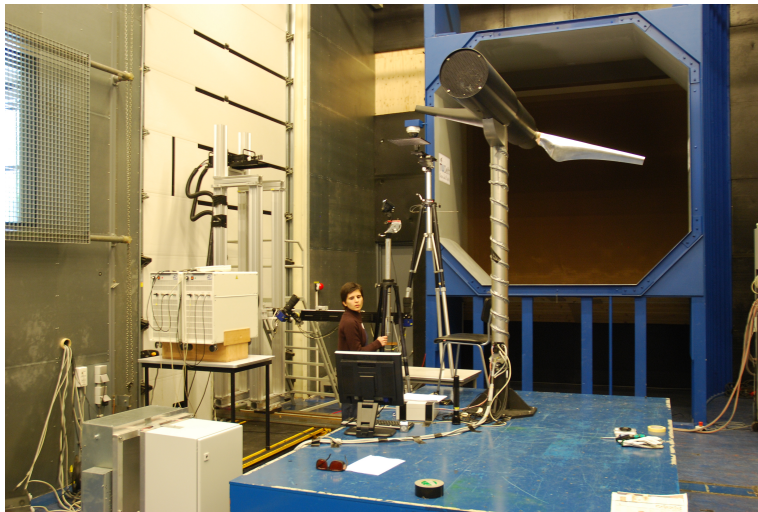
<i>Imaging, acquisition and processing</i>	
FOV [mm^2]	251 x 168
Number of PIV images	200 at <i>around blade</i> , 100 at <i>near wake</i>
Separation time [μs]	100
Post-processing software	Davis [®] 7.4
Window size [pix^2]	From 64 x 64 to 16 x 16
Final vector spacing [mm]	0.605

An overview of the PIV system in the wind tunnel can be seen in Figure A.6.

These pictures were taken during the preparation of the experimental set-up.



(a) Front view



(b) Back view

Figure A.6: An overview of the experimental set-up preparation in OJF.

A.4.1 Post-processing of PIV data

PIV images are processed in PIV system software, LaVision Davis[®] 7.4. After processing the data, instantaneous velocity fields are obtained. Instantaneous velocity fields are post-processed in the same software to get the phase-locked averaged velocity and velocity RMS vector fields. Averaged velocity fields include three components of absolute velocities. The velocity RMS is calculated as in Equations A.1 (see LaVision Product Manual (2009)):

$$\begin{aligned}
 U_{rms} &= \sqrt{\frac{1}{N-1} \sum_{i=1}^N (U_i - U_{median})^2} \\
 V_{rms} &= \sqrt{\frac{1}{N-1} \sum_{i=1}^N (V_i - V_{median})^2} \\
 W_{rms} &= \sqrt{\frac{1}{N-1} \sum_{i=1}^N (W_i - W_{median})^2}
 \end{aligned} \tag{A.1}$$

To be able to perform further analysis, vorticity is calculated. Three components of vorticity is calculated by using the velocity fields in the near wake region at different blade azimuth angles. Vorticity in cylindrical coordinates is calculated as follows:

$$\begin{aligned}
 \omega_r &= \frac{1}{r} \frac{\partial V_x}{\partial \theta} - \frac{\partial V_\theta}{\partial x} \\
 \omega_\theta &= \frac{\partial V_r}{\partial x} - \frac{\partial V_x}{\partial r} \\
 \omega_x &= \frac{1}{r} \frac{\partial}{\partial r} (r V_\theta) - \frac{1}{r} \frac{\partial V_r}{\partial \theta}
 \end{aligned} \tag{A.2}$$

A.4.2 Uncertainties in the measurements

A summary of the most relevant uncertainties and their estimated effects on the spanwise PIV velocity fields are summarized in Table A.4.

The truncation errors and the uncertainty in the velocity measurement that the velocity gradients include are calculated for an upstream position of a

PIV velocity field in the axial, radial and azimuthal directions and given in Table A.5.

Table A.4: Uncertainty in the PIV measurements

Sources	Upstream [m/s]	[%]	Wake [m/s]	[%]
σ_r	0.11	1.9	0.29	4.8
σ_x	0.08	1.3	0.44	7.3
σ_θ	0.29	4.8	0.35	5.8
$\varepsilon_{\sigma,r}$	0.02	16.2	0.07	23.3
$\varepsilon_{\sigma,x}$	0.01	16.44	0.10	22.7
$\varepsilon_{\sigma,z}$	0.05	16.43	0.08	22.8
ε_t (timing, [pix])	0.02			
$\lambda/2$ [mm]	1.44			
$PLRMS,max$ (V_r, V_x, V_θ)	0.07	0.1	0.08	
$PLRMS,mean$ (V_r, V_x, V_θ)	0.046	0.06	0.05	

Table A.5: Uncertainty in the measurements.

Quantity			
$\Delta r^2, \Delta x^2, \Delta \theta^2$ [m^2]	10^{-8}	10^{-8}	$7.62x10^{-3}$
$\varepsilon_r/\Delta r, \varepsilon_r/\Delta x, \varepsilon_r/\Delta \theta$ [1/s]	1110	1110	1.2714
$\varepsilon_x/\Delta r, \varepsilon_x/\Delta x, \varepsilon_x/\Delta \theta$ [1/s]	760	760	0.87
$\varepsilon_\theta/\Delta r, \varepsilon_\theta/\Delta x, \varepsilon_\theta/\Delta \theta$ [1/s]	2860	2860	3.276

A.5 Circulation: Blade 2

Circulation is estimated by integrating the vorticity, released from the present and previous blades passage, over the defined regions (see Figure A.7). Note that the presented contours in this figure are only schematic representation of the areas. The dimensionless total circulation just in the behind of the blade amounts to $\Gamma/(U_\infty R) \cong 0.065$ and in the further downstream released from the previous blade passage it reaches $\Gamma/(U_\infty R) \cong 0.078$. This is consistent with the total bound circulation already shown in Figure 4.13 for Blade 2 at $\lambda = 7$.

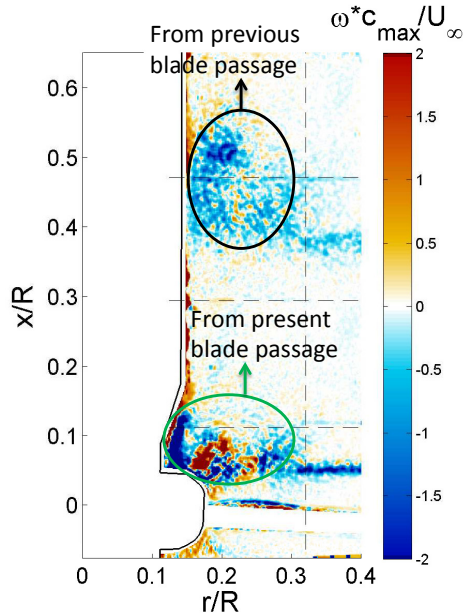


Figure A.7: Dimensionless azimuthal vorticity contour at $\Theta = 45^\circ$ from spanwise stereoscopic PIV measurements for Blade 2.

A.6 Input data in BOT

Blade geometry used in BOT for BEM simulations are tabulated for Blade 1 and 2 respectively in Figures A.8 and A.9. At the first six stations in Blade 2 (marked with the red paint), the thickness value had to be modified by looking at the real thickness distribution. If 18% thickness had been used for those sections, there would be a decreasing thickness distribution at the root. Therefore, this modification was performed in the input file of the Blade 2 geometry.

Blade geometry			<input type="checkbox"/> Airfoil distribution fix		
r [m]	c [m]	ε [°]	t [m]	t/c [-]	oil distribu
0.147	0.108	16.31	0.108	1.000	Cylinder (90.5%); TRANSIT (9.5%)
0.1641	0.110	15.72	0.093	0.850	Cylinder (59.2%); TRANSIT (40.8%)
0.1896	0.118	14.65	0.082	0.700	TRANSIT (72.1%); Cylinder (27.9%)
0.2067	0.127	13.89	0.063	0.500	TRANSIT (81.8%); DU18% (18.2%)
0.2152	0.133	13.51	0.046	0.350	DU18% (59.6%); TRANSIT (40.4%)
0.2238	0.139	13.14	0.042	0.300	DU18% (76.8%); TRANSIT (23.2%)
0.2494	0.162	12.03	0.029	0.180	DU18% (100%)
0.2835	0.186	10.66	0.034	0.180	DU18% (100%)
0.3261	0.202	9.15	0.036	0.180	DU18% (100%)
0.3688	0.193	7.84	0.035	0.180	DU18% (100%)
0.4029	0.176	6.94	0.032	0.180	DU18% (100%)
0.4456	0.160	5.94	0.029	0.180	DU18% (100%)
0.4882	0.145	5.09	0.026	0.180	DU18% (100%)
0.5308	0.132	4.34	0.024	0.180	DU18% (100%)
0.565	0.123	3.82	0.022	0.180	DU18% (100%)
0.6076	0.114	3.23	0.020	0.180	DU18% (100%)
0.6503	0.105	2.71	0.019	0.180	DU18% (100%)
0.6844	0.099	2.33	0.018	0.180	DU18% (100%)
0.727	0.093	1.91	0.017	0.180	DU18% (100%)
0.7697	0.087	1.53	0.016	0.180	DU18% (100%)
0.8038	0.083	1.25	0.015	0.180	DU18% (100%)
0.8465	0.078	0.93	0.014	0.180	DU18% (100%)
0.8891	0.074	0.64	0.013	0.180	DU18% (100%)
0.9232	0.071	0.43	0.013	0.180	DU18% (100%)
0.9574	0.068	0.23	0.012	0.180	DU18% (100%)
0.9829	0.066	0.09	0.012	0.180	DU18% (100%)
1	0.064	0.00	0.012	0.180	DU18% (100%)

Figure A.8: Blade geometry input in BOT for Blade 1.

A.7 Lift coefficient distribution

To have an idea about the performance of RFOIL in predicting the airfoil data at low Reynolds number, $Cl - \alpha$ (airfoil lift coefficient–angle of attack) distribution obtained from RFOIL is compared with the experiment for DU96-W-180 airfoil at $Re = 0.5 \times 10^{-6}$. Figure A.10 presents this comparison. It is observed that RFOIL prediction is very good between $\alpha = -4^\circ$ to $\alpha = 11^\circ$, but it starts to deviate from the experimental results beyond $\alpha = 11^\circ$.

Blade geometry			<input type="checkbox"/> Airfoil distribution fixe		
r [m]	c [m]	ε [°]	t [m]	t/c [-]	oil distribut
0.147	0.075	15.25	0.075	1.000	Cylinder (90.6%); TRANSIT (9.4%)
0.167	0.075	15.05	0.064	0.850	Cylinder (62.5%); TRANSIT (37.5%)
0.187	0.075	14.85	0.053	0.700	TRANSIT (75%); Cylinder (25%)
0.207	0.075	14.45	0.038	0.500	TRANSIT (87.8%); DU18% (12.2%)
0.2075	0.075	14.45	0.026	0.350	DU18% (62.4%); TRANSIT (37.6%)
0.2275	0.075	13.95	0.023	0.300	DU18% (71.4%); TRANSIT (28.6%)
0.2475	0.125	13.38	0.023	0.180	DU18% (100%)
0.2875	0.124	12.13	0.022	0.180	DU18% (100%)
0.3275	0.122	10.87	0.022	0.180	DU18% (100%)
0.3675	0.121	9.66	0.022	0.180	DU18% (100%)
0.4075	0.119	8.55	0.021	0.180	DU18% (100%)
0.4475	0.118	7.54	0.021	0.180	DU18% (100%)
0.4875	0.116	6.62	0.021	0.180	DU18% (100%)
0.5275	0.115	5.80	0.021	0.180	DU18% (100%)
0.5675	0.113	5.05	0.020	0.180	DU18% (100%)
0.6075	0.112	4.38	0.020	0.180	DU18% (100%)
0.6475	0.110	3.77	0.020	0.180	DU18% (100%)
0.6875	0.109	3.21	0.020	0.180	DU18% (100%)
0.7275	0.107	2.71	0.019	0.180	DU18% (100%)
0.7675	0.106	2.24	0.019	0.180	DU18% (100%)
0.8075	0.104	1.82	0.019	0.180	DU18% (100%)
0.8475	0.103	1.43	0.018	0.180	DU18% (100%)
0.8875	0.101	1.08	0.018	0.180	DU18% (100%)
0.9275	0.100	0.75	0.018	0.180	DU18% (100%)
1	0.098	0.21	0.018	0.180	DU18% (100%)

Figure A.9: Blade geometry input in BOT for Blade 2.

A.8 Additional CFD results

To be able to see the vorticity distribution in the vicinity of the nacelle, CFD results are analysed in detail. In Figure A.11, azimuthal vorticity distribution is presented.

CFD simulations are also performed at the blade pitch angles $\theta_{p,0} = -1^\circ$ and $\theta_{p,0} = +1^\circ$ to see the effect of it on the blade flow. Figure A.12 presents the axial and radial velocity distributions at different pitch angles. It is clearly seen that the distributions look very similar for the three cases.

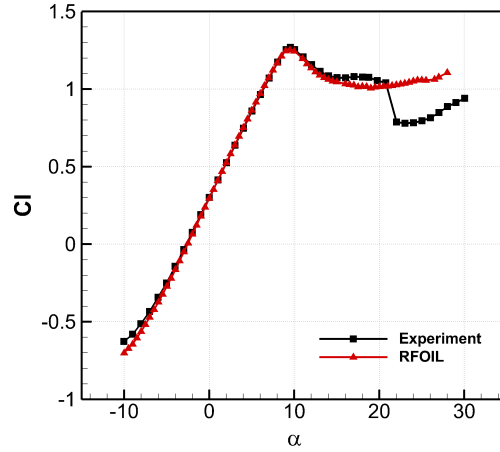


Figure A.10: $C_l - \alpha$ distributions obtained from experiment and RFOIL at $Re = 5 \times 10^5$ for DU96-W-180.

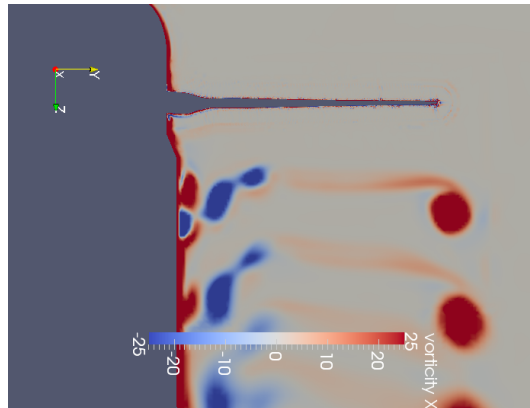
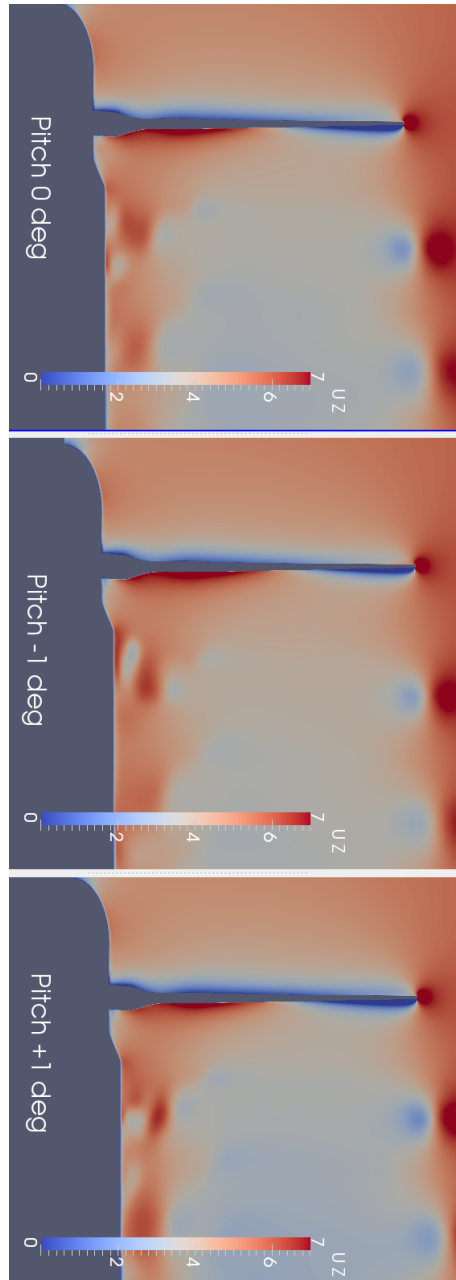
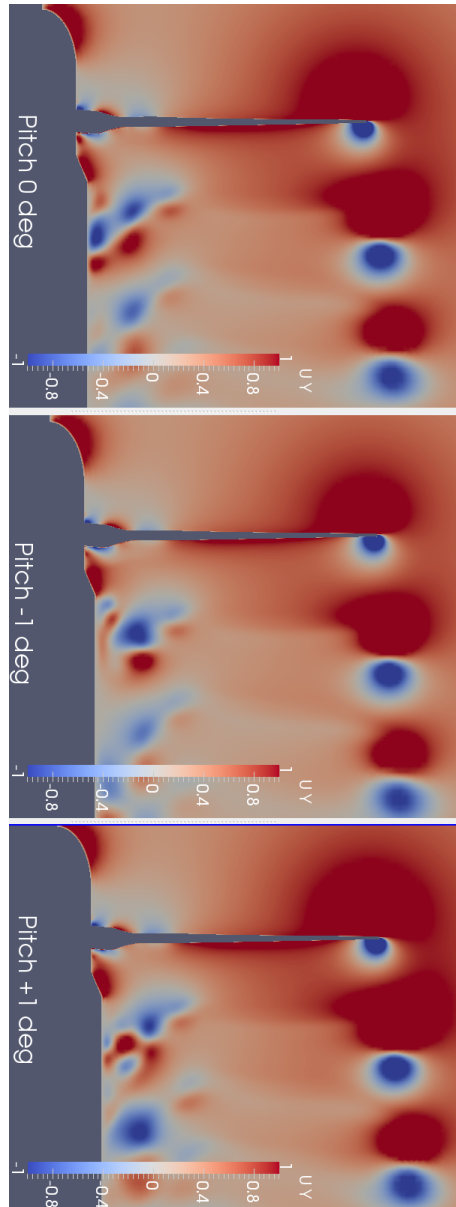


Figure A.11: Azimuthal vorticity distribution obtained by CFD for Blade 1 at $\theta_{p,0} = 0^\circ$.



(a) Axial velocity distributions.

Figure A.12: Velocity distributions obtained by CFD at three different blade pitch angles.



(b) Radial velocity distributions.

Figure A.12: (continued) Velocity distributions obtained by CFD at three different blade pitch angles.

Bibliography

- Akay, B., Ferreira, C., van Bussel, G., and Herraez, I. (2012a). Experimental and numerical quantification of radial flow in the root region of a hawt. *50th AIAA Aerospace Sciences Meeting - 30th ASME wind Energy Symposium, Nashville, Tennessee.*
- Akay, B., Micallef, D., Ferreira, C., and van Bussel, G. (2011). Stereo PIV experiments on Horizontal Axis Wind Turbine Rotor. In *46th Applied Aerodynamics Symposium, Orleans, France.*
- Akay, B., Micallef, D., Ferreira, C., and van Bussel, G. (9-11 October 2012b). Experimental analysis of the evolution of the hawt root flow. In *The Science of making torque from wind Conference, Oldenburg, Germany.*
- Akay, B., Ragni, D., Ferreira, C., and van Bussel, G. (2013). Experimental investigation of the root flow in a horizontal axis wind turbine. *Wind Energy*, DOI: 10.1002/we.1620.
- Akay, B., Tescione, G., Ferreira, C., and van Bussel, G. (28-20 June 2010a). Experimental and numerical investigation of the effect of rotor blockage on wake expansion. In *The Science of making torque from wind Conference, Crete, Greece.*
- Akay, B., Tescione, G., Ferreira, C., and van Bussel, G. (4-7 January 2010b). Experimental investigation of the wind turbine blade root flow. In *48th AIAA Aerospace Sciences Meeting Including the New Horizons Forum and Aerospace Exposition, Orlando, Florida.*
- Anderson Jr., J. (2001). *Incompressible flow over finite wings, Fundamentals of Aerodynamics.* McGRAW-HILL.
- Bernardy, S. (2013). *Private communication.* Wind Energy Group, Delft University of Technology.
- Betz, A. (1919). *Schraubenpropeller mit geringstem Energieverlust.* PhD thesis,

- Gottingen.
- Bot, E. and Ceyhan, O. (March 2011). Blade optimization tool (bot). Technical report, ECN.
- Breton, S. (2008). *Study of the stall delay phenomenon and of wind turbine blade dynamics using numerical approaches and NRELS wind tunnel tests*. PhD thesis, Norwegian University of Science and Technology.
- Breton, S., Coton, F., and Moe, G. (2008). A study on rotational effects and different stall delay models using a prescribed wake vortex scheme and NREL Phase VI experiment data. *Wind Energy*, 11:459–482.
- Bruun, H. (1995). *Hot-Wire Anemometry: Principles and signal analysis*. Oxford University Press.
- Chaviaropoulos, P. and Hansen, M. (2000). Investigating Three-Dimensional and rotational effects on wind turbine blades by means of a quasi-3d Navier-Stokes solver. *Journal of Fluids Engineering*, 122:330–336.
- Cotroni, A., Felice, F. D., Romano, G., and Elefante, M. (2000). Investigation of the near wake of a propeller using Particle Image Velocimetry. *Experiments in Fluids [Suppl.]*, pages S227–S236.
- Del Campo, V., Ragni, D., Micaleff, D., Akay, B., Diez, F., and C.S., F. (2013). 3D load calculation on a horizontal axis wind turbine using PIV. *Wind Energy*, (Accepted).
- Du, Z. and Selig, M. (2000). The effect of rotation on the boundary layer of a wind turbine blade. *Renewable Energy*, 20:167–181.
- Dumitrescu, H. and Cardos, V. (2003). Rotational effects on the boundary-layer flow in wind turbines. Technical report, AIAA Journal-Technical Notes.
- Dumitrescu, H., Cardos, V., and Dumitrache, A. (2007). Modeling of inboard stall delay due to rotation. *Journal of Physics: Conference Series 012022*, 75.
- Ebert, P. and Wood, D. (1997). The near wake of a model horizontal-axis wind turbine-I: Experimental arrangements and initial results. *Renewable Energy*, 12:225–243.
- Ebert, P. and Wood, D. (1999). The near wake of a model horizontal-axis wind turbine-II: General features of the three-dimensional flowfield. *Renewable Energy*, 18:513–534.
- Ebert, P. and Wood, D. (2001). The near wake of a model horizontal-axis wind turbine, Part 3: Properties of the tip and hub vortices. *Renewable Energy*,

- 22:461–472.
- Ferrer, E. and Munduate, X. (2007). Wind turbine blade tip comparison using CFD. *Journal of Physics: Conference series 012005*, 75.
- Fogarty, L. (1951). The laminar boundary layer on a rotating blade. *J. Aero. Sci.*, 18:247–252.
- Gousseau, P. (2012). *Numerical modeling of micro-scale wind-induced pollutant dispersion in the built environment*. PhD thesis, Eindhoven University of Technology.
- Hand, M., Simms, D., Fingersh, L., Jager, D., Cotrell, J., Schreck, S., and Larwood, S. (December 2001). Unsteady aerodynamics experiment phase vi: Wind tunnel test configurations and available data campaigns. Technical report, NREL.
- Heinzelmann, B., Gollnick, B., Thamsen, P., Petsche, M., and Christiansen, J. (2008). Investigations into boundary layer fences in the hub area of wind turbine blades. In *European Wind Energy Conference (EWEC)*.
- Herraez, I., Akay, B., van Bussel, G., Peinke, J., and Stoevesandt, B. (doi:10.5194/wes-2015-1, 2016). On the flow over the blade root of a horizontal axis wind turbine. *journal Wind Energ. Sci.*
- Himmelskamp, H. (1947). Profile investigations on a rotating airscrew. Technical report, MAP Volkenrode, Reports and Translation. No:832.
- Hu, D., Hua, O., and Du, Z. (2006). A study on stall-delay for horizontal axis wind turbine. *Renewable Energy*, 31:821–836.
- IconCFD (Last visit: 28 October 2013). <http://iconcfd.com/services/iconcfd>.
- Ivanell, S., Sørensen, J. N., Mikkelsen, R., and Henningson, D. (2007). Numerical analysis of the tip and root vortex position in the wake of a wind turbine. *Journal of Physics: Conference Series 012035*, 75.
- Joukowsky, N. (1912). Vortex theory of a rowing screw. *Tr. Otd. Fiz. Nauk Obshchestva Lubitelei Estestvozn.*, 16:1.
- Katz, J. and Plotkin, A. (Second Edition, 2001). *Low-Speed Aerodynamics*. Cambridge University Press.
- Kurtulus, D., Scarano, F., and David, L. (2007). Unsteady aerodynamic forces estimation on a square cylinder by TR-PIV. *Experiments in Fluids*, 42:185–196.
- LaVision Product Manual (January 8, 2009). FlowMaster. Technical report,

- Manual No:1003005.
- Leishman, J. G. (2000). *Principles of Helicopter Aerodynamics*. Cambridge University Press.
- Lindenburg, C. (22-25 November, 2004). Modelling of rotational augmentation based on engineering considerations and measurements. In *European Wind Energy Conference (EWEC), London*.
- Lourenco, L. and Krothapalli, A. (1995). On the accuracy of velocity and vorticity measurements with PIV. *Experiments in fluids*, 18:421–428.
- Manwell, J., McGowan, J., and Rogers, A. (2002). *Wind Energy Explained - Theory, Design and Application*. John Wiley & Sons Ltd.
- Massouh, F. and Dobrev, I. (2007). Exploration of the vortex wake behind of wind turbine rotor. *Journal of Physics: Conference Series 012036*, 75.
- Mast, E., Vermeer, L., and van Bussel, G. (2004). Estimation of the circulation distribution on a rotor blade from detailed near wake velocities. *Wind Energy*, 7 (3) C35-00:189–209.
- Medici, D. and Alfredsson, P. (2006). Measurements on a wind turbine wake: 3D effects and bluff body vortex shedding. *Wind Energy*, 9:219–236.
- Micallef, D., a. A. B. F. C., Sant, T., and van Bussel, G. (9-11 October 2012a). The origins of a wind turbine tip vortex. In *The Science of making torque from wind Conference, Oldenburg, Germany*.
- Micallef, D. (2012). *3D flows near a HAWT rotor: A dissection of blade and wake contribution*. PhD thesis, Delft University of Technology.
- Micallef, D., Akay, B., Sant, T., Ferreira, C., and van Bussel, G. (2011). Experimental and numerical study of radial flow and its contribution to wake development of a HAWT. In *European Wind Energy Conference and Exhibition-EWEC, Brussels*.
- Micallef, D., Akay, B., Sant, T., Ferreira, C., and van Bussel, G. (2012b). Flow three-dimensionality near the wind turbine blade. *Solar Energy*, Accepted.
- Milborrow, D. (1985). Changes in aerofoil characteristics due to radial flow on rotating blades. In *Proceedings of the 7th BWEA conference, Oxford*.
- Moriarty, P. and Hansen, A. (2005). Aerodyn theory manual. Technical report, National Renewable Energy Laboratory.
- Morton, B. (1984). The generation and decay of vorticity. *Geophys. Astrophys. Fluid Dynamics*, 28:277–308.

- Munson, B., Young, D., and Okiishi, T. (2002). *Fundamentals of Fluid Mechanics, Fourth Edition*. John Wiley & Sons Ltd.
- Noca, F., Shields, D., and Jeon, D. (1999). A comparison of methods for evaluating time-dependent fluid dynamic forces on bodies, using only velocity fields and their derivatives. *Journal of Fluids and Structures*, 13:551–578.
- OpenFOAM User Guide (17 June 2013). *Version 2.2.1*.
- Raffel, M., Willert, C., Wereley, S. T., and Kompenhans, J. (2007). *Particle Image Velocimetry, A Practical Guide*. Springer-Verlag Berlin Heidelberg.
- Ragni, D. (2012). *PIV-based load determination in aircraft propellers*. PhD thesis, Delft University of Technology.
- Ragni, D., van Oudheusden, B., and Scarano, F. (2011). 3D pressure imaging of an aircraft propeller blade-tip flow by phase-locked stereoscopic PIV. *Experiments in fluids*, pages 463–477.
- Saffman, P. and Baker, G. (1979). Vortex interactions. *Ann. Rev. Fluid Mech.*, 11:95–122.
- Schepers, G. and Snel, H. (2007). Model experiments in controlled conditions (MEXICO). Technical report, ECN-E-07-042.
- Schreck, S., Sørensen, N., and Robinson, M. (2007). Aerodynamic structures and processes in rotationally augmented flow fields. *Wind Energy*, 10:159–178.
- Schrijer, F. and Scarano, F. (2008). Effect of predictor-corrector filtering on the stability and spatial resolution of iterative PIV interrogation. *Exp Fluids*, 45:927–941.
- Shen, W., Mikkelsen, R., Sørensen, N., and Bak, C. (2005). Tip loss corrections for wind turbine computations. *Wind energy*, 8:457–475.
- Sherry, M., Nemes, A., Jacono, D. L., Blackburn, H. M., and Sheridan, J. (2013). The interaction of helical tip and root vortices in a wind turbine wake. *Physics of Fluids* 25.
- Sherry, M., Sheridan, J., and Jacono, D. L. (2010). Horizontal axis wind turbine tip and root vortex measurements. In *15th Int Symp on Applications of Laser Techniques to Fluid Mechanics*.
- Snel, H. (1998). Review of the present status of rotor aerodynamics. *Wind Energy*, 1:46–69.
- Snel, H. (2003). Review of aerodynamics for wind turbines. *Wind Energy*,

- 6:203–211.
- Snel, H., Houwink, R., and Bosschers, J. (December 1994). Sectional prediction of lift coefficient on rotating wind turbine blades in stall. Technical report, ECN.
- Snel, H., Houwink, R., van Bussel, G., and Bruining, A. (1993). Sectional prediction of 3D effects for stalled flow on rotating blades and comparison with measurements. In *1993 European Community Wind Energy Conference Proceedings, Lubeck-Travemunde, Germany*.
- Sørensen, J. N. (1986). Prediction of three-dimensional stall on wind turbine blade using three-level, viscous-inviscid interaction model. *European Wind Energy Association Conference and Exhibition*, pages 429–435.
- Sørensen, J. N. (2011). Aerodynamic aspects of wind energy conversion. *Annu. Rev. Fluid Mech.*, 43:427–448.
- Sørensen, N., Bechmann, A., and Zahle, F. (2011). 3D CFD computations of transitional flows using DES and a correlation based transition model. *Wind Energy*, 14:77–90.
- Spalart, P. R. and Allmaras, S. R. (1992). A one-equation turbulence model for aerodynamic flows. In *Aerospace Sciences Meetings*, pages –. American Institute of Aeronautics and Astronautics.
- Timmer, N. (2013). *Private communication*. Wind Energy Group, Delft University of Technology.
- Unal, M., Lin, J., and Rockwell, D. (1997). Force prediction by PIV imaging: a momentum-based approach. *Journal of Fluids and Structures*, 11:965–971.
- van Bussel, G. (1995). *The aerodynamics of horizontal axis wind turbine rotors explored with asymptotic expansion methods*. PhD thesis, Delft University of Technology.
- Van Oudheusden, B., Scarano, F., Roosenboom, E., Casimiri, E., and Souverein, L. (2007). Evaluation of integral forces and pressure fields from planar velocimetry data for incompressible and compressible flows. *Exp Fluids*, 43:153–162.
- Vermeer, L., Sørensen, J., and Crespo, A. (2003). Wind turbine wake aerodynamics. *Progress in Aerospace Sciences*, 39:467–510.
- Westerweel, J. (1993). *Digital particle image velocimetry, Theory and application*. PhD thesis, Delft University of Technology.
- Westerweel, J. (1998). Effect of sensor geometry on the performance of piv

- interrogation. *9th International Symposium Laser Techniques applied to fluid mechanics, Lisbon, Portugal.*, pages 37–56.
- Whale, J., Anderson, C., Bareiss, R., and Wagner, S. (2000). An experimental and numerical study of the vortex structure in the wake of a wind turbine. *Journal of Wind Engineering and Industrial Aerodynamics*, 84:1–21.
- Wood, D. (1991). A three-dimensional analysis of stall-delay on a horizontal-axis wind turbine. *Journal of Wind Engineering and Industrial Aerodynamics*, 37 (1991) 1-14, 37:1–14.

Nomenclature

Abbreviations

2D	Two-dimensional
3D	Three-dimensional
BEM	Blade Element Momentum
BOT	Blade Optimization Tool
CFD	Computational Fluid Dynamics
DNS	Direct Numerical Simulation
ECN	Energy Research Center of the Netherlands
FOV	Field of view
HAWT	Horizontal axis wind turbine
HAWTDAWG	Name of a prescribed wake model
MEXICO	Model Rotor Experiments under Controlled Conditions
NREL	National Renewable Energy Laboratory
OJF	Open jet facility
PIV	Particle image velocimetry
PL	Peak locking
RANS	Reynolds-Averaged Navier-Stokes
RMS	Root mean square

RPM	Revolution per minute
TI	Turbulence intensity

Symbols

α	Angle of attack, [$^{\circ}$]
ϵ_{bias}	Bias error
ϵ_{rms}	Random/measurement error
ϵ_{tot}	Absolute measurement error
Γ	Circulation, [$m^2 s^{-1}$]
$\lambda/2$	Minimum size of flow structure
λ	Tip speed ratio
μ	Dynamic viscosity, [$kgm^{-1}s^{-1}$]
ν	Kinematic viscosity, [$m^2 s^{-1}$]
Ω	Rotational velocity, [$rads^{-1}$]
ω	Vorticity, [s^{-1}]
ω_{θ}	Azimuthal vorticity component, [s^{-1}]
ω_r	Radial vorticity component, [s^{-1}]
ω_x	Axial vorticity component, [s^{-1}]
ω_y	Spanwise vorticity component, [s^{-1}]
ρ_{∞}	Ambient air density, [kgm^{-3}]
σ	Standard deviation
Θ	Blade azimuth angle, [$^{\circ}$]
θ	Azimuthal direction, [$^{\circ}$]
$\theta_{p,0}$	Blade pitch angle, [$^{\circ}$]

ε_μ	Uncertainty in the mean velocity
ε_σ	Uncertainty in the velocity fluctuations
ε_t	Uncertainty due to jitter of the timing
c/r	Local solidity
C_l	Lift force coefficient
c_{max}	Maximum chord, [m]
C_P	Power coefficient
C_p	Pressure coefficient
C_T	Thrust coefficient
N_b	Number of blades
U_∞	Freestream velocity, [ms^{-1}]
V_θ	Azimuthal velocity component, [ms^{-1}]
V_r	Radial velocity component, [ms^{-1}]
V_x	Axial velocity component, [ms^{-1}]
V_y	Spanwise velocity component, [ms^{-1}]
V_z	Tangential velocity component, [ms^{-1}]
y^+	Non-dimensional wall distance
$Z_{\alpha/2}$	Coefficient of confidence
c	Chord, [m]
F	Force, [N]
N	Number of PIV images
q	Induced velocity, [ms^{-1}]
R	Blade radius, [m]
r	Radial direction, [m]

Re	Reynolds number
t	Time, [s]
V	Velocity, [ms^{-1}]
X,x	Axial direction, [m]
Y,y	Spanwise direction, [m]
Z,z	Tangential direction, [m]

List of Figures

1.1	Schematic lifting line representation of a blade.	4
1.2	Schematic representation of the present rotor model's parts (Blade 1).	10
1.3	An example of a wind turbine blade without transition part (Enercon E 82). The figure is taken from http://www.wind-energy-the-facts.org/large-commercial-wind-turbines.html . . .	10
1.4	Sketch of the vortex system corresponding to lifting line theory of the ideal propeller of (a) Joukowsky and (b) Prandtl & Betz. Figure is taken from Sørensen (2011).	11
1.5	Streamlines at local angle of attack $\alpha = 24.588^\circ$. Figures are taken from Hu et al. (2006). The radial position is not mentioned.	14
1.6	Measured power as a function of incoming wind speed compared with power predicted from a prescribed wake model (HAWTDAWG) with and without different stall delay models. Figure is taken from Breton et al. (2008).	16
2.1	Geometrical representation of the blades used in the wind tunnel experiments.	20
2.2	Chord and twist distributions of the two model rotor blades. . .	21
2.3	Schematic representation of stereoscopic PIV setup.	23
2.4	Schematic representation of the spanwise measurement set-up in the OJF.	25
2.5	(a) Measurement plane location at $\Theta = 0^\circ$ (reference angle). (b) Combined fields of views (FOVs) in the blade flow, the "s" panels, and in the near wake, the "w" panels.	26
2.6	Schematic representation of the chordwise measurement set-up in the OJF.	27

2.7	An example of PIV image for pressure side measurement. . . .	28
2.8	Measured radial velocity fields at some blade azimuth angles with iso-surfaces at $V_r = 0.15, 0$, and -0.2	29
3.1	3D visualization of radial velocity from stereoscopic PIV measurements. Iso-surfaces at $V_r = 0.15, 0$, and -0.2	35
3.2	Dimensionless axial velocity distributions at four blade azimuth angles from stereoscopic PIV measurements. Inflow is in $+x/R$ direction.	37
3.3	Dimensionless azimuthal velocity distributions at four blade azimuth angles from stereoscopic PIV measurements. Inflow is in $+x/R$ direction.	39
3.4	Dimensionless radial velocity distributions at four blade azimuth angles from stereoscopic PIV measurements. Inflow is in $+x/R$ direction.	40
3.5	Dimensionless tangential velocity distributions at four radial positions from root (a) $r/R = 0.25$ to mid-board (d) $r/R = 0.52$, from stereoscopic PIV measurements in chordwise direction. Inflow is in $+x/R$ direction. Note that the data at $z/R = -0.05$ and $x/R = 0.025$ was masked due to reflection.	41
3.6	3D visualization of dimensionless vorticity magnitude. Vorticity iso-surfaces at $\frac{ \omega c_{max}}{U_\infty} = 2.1$, and 1.5 . (a) Side view (b) Top view (c) Zoomed-in to the root flow.	43
3.7	3D visualization of dimensionless vorticity components from stereoscopic PIV measurements.	44
3.7	(continued) 3D visualization of dimensionless vorticity components from stereoscopic PIV measurements.	45
3.8	Dimensionless spanwise vorticity distributions at four radial positions from root (a) $r/R = 0.25$ to mid-board (d) $r/R = 0.52$, from stereoscopic PIV measurements in chordwise direction. Inflow is in $+x/R$ direction. Note that the data at $z/R = -0.05$ and $x/R = 0.025$ was masked due to reflection.	47
3.9	Dimensionless azimuthal vorticity distributions from stereoscopic PIV measurements.	49
3.8	(continued) Dimensionless azimuthal vorticity distributions at eight blade azimuth angles from stereoscopic PIV measurements.	50
3.9	3D visualization of pressure coefficient, iso-surfaces at $C_p = -0.14$, and -0.25	52
3.10	Dimensionless vorticity magnitude and pressure coefficient contour plots, blade azimuthal position $\Theta = -20^\circ$	52

3.11	Dimensionless vorticity magnitude and pressure coefficient contour plots, blade azimuthal position $\Theta = 75^\circ$	53
4.1	Blade 1 at $\lambda = 7$, dimensionless axial and azimuthal velocity distributions at $\Theta=45^\circ$ from stereoscopic PIV measurements. Inflow is in $+x/R$ direction.	57
4.2	Blade 2 at $\lambda = 7$, dimensionless axial and azimuthal velocity distributions at $\Theta=45^\circ$ from stereoscopic PIV measurements. Inflow is in $+x/R$ direction.	58
4.3	Blade 2 at $\lambda = 5$, dimensionless axial and azimuthal velocity distributions at $\Theta=45^\circ$ from stereoscopic PIV measurements. Inflow is in $+x/R$ direction.	58
4.4	Blade 1 at $\lambda = 7$, dimensionless radial velocity distribution from stereoscopic PIV measurements. Inflow is in $+x/R$ direction.	59
4.5	Blade 2 at $\lambda = 7$, dimensionless radial velocity distribution from stereoscopic PIV measurements. Inflow is in $+x/R$ direction.	60
4.6	Blade 2 at $\lambda = 5$, dimensionless radial velocity distribution from stereoscopic PIV measurements. Inflow is in $+x/R$ direction.	60
4.7	Dimensionless velocity plots at $\Theta=0^\circ$, $x/R = 0.05$ for three test cases, from stereoscopic PIV measurements.	61
4.8	Dimensionless velocity plots at $\Theta=0^\circ$, $x/R = 0.1$ for three test cases, from stereoscopic PIV measurements.	62
4.9	Blade 1 at $\lambda = 7$, dimensionless azimuthal vorticity distributions calculated from stereoscopic PIV measurements. Inflow is in $+x/R$ direction.	63
4.10	Blade 2 at $\lambda = 7$, dimensionless azimuthal vorticity distributions calculated from stereoscopic PIV measurements. Inflow is in $+x/R$ direction.	63
4.11	Blade 2 at $\lambda = 5$, dimensionless azimuthal vorticity distributions calculated from stereoscopic PIV measurements. Inflow is in $+x/R$ direction.	64
4.12	Representation of rectangular contour approach for circulation calculation. Non-dimensional tangential velocity contour at $r/R=0.52$	65
4.13	Blade 1 and Blade 2 at $\lambda = 7$, dimensionless spanwise bound vorticity obtained from the chordwise stereoscopic PIV experiments.	66
4.14	Dimensionless strength of trailing vortex derived from the bound circulation.	66

5.1	Dimensionless bound vorticity calculated from chordwise stereoscopic PIV measurements.	71
5.2	Dimensionless azimuthal vorticity contour at $\Theta = 0^\circ$, $\Theta = 45^\circ$, and $\Theta = 75^\circ$ from spanwise stereoscopic PIV measurements. . .	74
5.3	Schematic representation of the vortices in the near wake region. Note that the position of the vortices is taken from PIV measurements.	75
5.4	45° slice of 3D visualization of dimensionless vorticity magnitude. Vorticity iso-surfaces at $\frac{ \omega _{max}}{U_\infty} = 2.1$, and 1.5.	76
5.5	Three components of the dimensionless induced velocity distributions on the suction surface of the blade near the root. . . .	77
5.5	(continued) Three components of the dimensionless induced velocity distributions on the suction surface of the blade near the root.	78
5.6	Dimensionless spanwise velocity distributions at three spanwise positions of Blade 1 . Inflow is in $+x/R$ direction. Note that the data from PIV at $x/R = 0.025$ and $z/R = -0.05$ was masked due to reflection.	79
5.7	Isobars and limiting streamlines over the suction side of the blade root region. Figure is taken from Herraez et al. (2016).	80
5.8	Spanwise velocity distributions along the lines shown in Figures 5.6, at $z/R \cong 0.17$ along x/R , at three radial positions. . .	81
5.9	Extracted spanwise velocity points above the blade surface in the inertial frame of reference.	82
5.10	Dimensionless spanwise velocity component obtained above the blade surface from the PIV measurements in the inertial frame of reference.	82
6.1	Velocity field representation. Stationary contour (Left) and moving contour (Right). Figure is taken from Ragni (2012).	87
6.2	Boundary conditions of the measurement volume.	89
6.3	Computational domain with rotor model and a view from the Inlet.	91
6.4	Computational domain close to the blade.	91
6.5	Normal force calculations for Blade 1 obtained by different methods.	95
6.6	Normal force calculations for Blade 1 predicted by BEM and CFD	97
6.7	Normal force calculations for Blade 1 at different blade pitch angles, $\theta_{p,0}$	99

6.8	Tangential force calculations for Blade 1 predicted by different methods.	100
6.9	Chord distribution of Blade 1	100
6.10	Dimensionless axial velocity distributions for Blade 1 at three spanwise positions. Left column PIV, right column CFD. Inflow is in $+x/R$ direction. Note that the area at $x/R = 0.025$ and $z/R = -0.05$ in PIV data was masked due to reflection.	104
6.11	Dimensionless tangential velocity distributions for Blade 1 at three spanwise positions. Left column PIV, right column CFD. Inflow is in $+x/R$ direction. Note that the area at $x/R = 0.025$ and $z/R = -0.05$ in PIV data was masked due to reflection.	105
6.12	Dimensionless spanwise velocity distributions for Blade 1 at three spanwise positions. Left column PIV, right column CFD. Inflow is in $+x/R$ direction. Note that the area at $x/R = 0.025$ and $z/R = -0.05$ in PIV data was masked due to reflection.	106
6.13	Normal force calculations for Blade 2 obtained by different methods.	108
6.14	Tangential force calculations for Blade 2 obtained by different methods.	109
6.15	Chord distribution Blade 2	109
A.1	Schematic representation of open jet facility at TU Delft.	118
A.2	Close view to the hub.	119
A.3	Schematic representation of rotor model with another set of blades.	120
A.4	Measuring springs where the strain gauges are fixed.	121
A.5	Precision-machined twin level calibration target with dot pattern for stereo PIV calibration. Levels are separated by 2mm, dots are equally spaced on a 10mm grid. Figure is taken from Raffel et al. (2007).	121
A.6	An overview of the experimental set-up preparation in OJF.	123
A.7	Dimensionless azimuthal vorticity contour at $\Theta = 45^\circ$ from spanwise stereoscopic PIV measurements for Blade 2.	126
A.8	Blade geometry input in BOT for Blade 1.	127
A.9	Blade geometry input in BOT for Blade 2.	128
A.10	$Cl - \alpha$ distributions obtained from experiment and RFOIL at $Re = 5 \times 10^5$ for DU96-W-180.	129
A.11	Azimuthal vorticity distribution obtained by CFD for Blade 1 at $\theta_{p,0} = 0^\circ$	129
A.12	Velocity distributions obtained by CFD at three different blade pitch angles.	130

A.12 (continued) Velocity distributions obtained by CFD at three different blade pitch angles.	131
--	-----

List of Tables

2.1	Measurement conditions.	22
A.1	HAWT stereoscopic PIV experiments	117
A.2	PIV apparatus	122
A.3	PIV setup parameters for spanwise measurements.	122
A.4	Uncertainty in the PIV measurements	125
A.5	Uncertainty in the measurements.	125

Acknowledgements

The work presented in this thesis is the result of the PhD project sponsored by VESTAS in the Wind Energy Group of the Aerospace Faculty at Delft University of Technology. It would not have been possible without the guidance, help and support of many people that I would like to thank here.

First, I am grateful to Prof. Gerard van Bussel for his dedicated support and his valuable contribution to this thesis.

I would like to thank Carlos Simão Ferreira for his support and guidance during this work.

I would like to thank Niels Olesen and Dick Veldkamp for giving me the chance to work in this project for Vestas.

The experiments of this thesis would not have been possible without the valuable help and support of the technical staff of the faculty.

I am grateful to the committee members, namely Prof. Gijs van Kuik, Prof. Fulvio Scarano, Prof. Jeroen van Beeck, Prof. Tor Anders Nygaard and Dr. Scott Schreck for reviewing the thesis and providing valuable comments.

I wish to express my gratitude to all my colleagues at TU Delft that I had the chance to work with.

I also would like to thank my colleagues at Siemens Wind Power A/S, in particular Alex Loeven for his support during the finalization of this thesis; Stefan Oerlemans for translating my thesis summary to Dutch; Frank Scheurich and Drew Gertz for the proof reading of the thesis.

Finally, I would like to thank my family and friends for making this road more enjoyable and valuable.

Thanks to the Herning Bibliotek and Cafe Belga for providing a cool environment during the finalization of this thesis.

Buşra Akay
Herning, July 2016

Curriculum vitae and list of publications

Curriculum vitae

Busra Akay was born on the 30th August, 1980 in Kayseri, Turkey. She studied Aerospace Engineering at Middle East Technical University (Ankara, Turkey) which she obtained Bachelor (2005) and Master (2007) degrees. Afterwards, she enrolled the Research Master program (former Diploma Course) of the von Karman Institute for Fluid Dynamics (Rhode-St-Genèse, Belgium) and graduated from Turbomachinery and Propulsion Department in June 2008.

January 2009, she started her PhD on horizontal axis wind turbine blade root flow aerodynamics at the Delft University of Technology, Wind Energy Group, which has resulted in this thesis.

Currently, she is working at Siemens Wind Power A/S as an aerodynamics engineer, in Denmark.

List of publications

Journal papers

- Herraез, I., Akay B., van Bussel G.J.W., Peinke, J., Stoevesandt, B., (2015). Detailed Analysis of the Blade Root Flow of a Horizontal Axis Wind Turbine. *Wind Energ. Sci. Discuss.*, doi:10.5194/wes-2015-1, 2016.
- Akay B., Ragni D., Simão Ferreira C., van Bussel G.J.W., (2012). Investigation of the root flow in a horizontal axis wind turbine. *Wind Energy*. John Wiley & Sons, Ltd.
- Akay B., Micallef D., Simão Ferreira C., van Bussel G.J.W., (2012). Experimental analysis of the evolution of the HAWT root flow. *Journal of Physics: Conference Series*. IOP Science.
- Micallef D., Akay B., Sant T., Simão Ferreira C., van Bussel G. (2012). Flow three-dimensionality near the wind turbine blade. *Solar energy engineering*. ASME.
- Micallef D., Akay B., Simão Ferreira C., Sant T. van Bussel G., (2012). The origins of a wind turbine tip vortex. *Journal of Physics: Conference Series*. IOP Science.
- Del Campo V., Ragni D., Micallef D., Akay B., Diez F.J., Simão Ferreira C., (2012). 3D load calculation on a horizontal axis wind turbine using PIV. *Wind Energy*. John Wiley & Sons, Ltd.

Conference papers

- Del Campo V., Ragni D., Micallef D., Akay B., Diez J., Simão Ferreira C. (2013). Non intrusive 3D load calculation during yaw conditions. *EWEA 4 - 7 February 2013*, Vienna.
- Akay B., Simão Ferreira C., van Bussel G.J.W., Herraез, I., (2012). Experimental and numerical quantification of radial flow in the root region of a HAWT. *50th AIAA Aerospace Sciences Meeting including the New Horizons Forum and Aerospace Exposition*, 09 - 12 January 2012, Nashville, Tennessee.
- Micallef D., Akay B., Sant T., Simão Ferreira C. and van Bussel G. (2012). Body and wake influences on the 3D flow close to a HAWT rotor. *Euromech 528*, Wind Energy and the impact of turbulence on the conversion process, Oldenburg, Germany.
- Del Campo V., Ragni D., Micallef D., Akay B., Diez J., Simão Ferreira

C. (2012). Load calculation on a HAWT using PIV. Euromech 528, Wind Energy and the impact of turbulence on the conversion process, Oldenburg, Germany.

- Akay B, Micallef D., Ferreira C.S., van Bussel G.W.J., (2011). Stereo PIV Experiments on Horizontal Axis Wind Turbine Rotor. 46th Applied Aerodynamics Symposium, Orleans, France.
- Micallef D., Akay B, Ferreira C.S., van Bussel G.W.J., (2011). Experimental and Numerical Study of Radial Flow and Its contribution to Wake Development of a HAWT. EWEC, Brussels, Belgium.
- Akay B, Tescione G., Ferreira C.S., van Bussel G.W.J., (2010). Experimental and Numerical Investigation of the Effect of Rotor Blockage on Wake Expansion. The Science of making torque from wind Conference, Crete, Greece.
- Akay B, Tescione G., Ferreira C.S., van Bussel G.J.W. Experimental Investigation of the Wind Turbine Blade Root Flow. 48th AIAA Aerospace Sciences Meeting Including the New Horizons Forum and Aerospace Exposition, 4 - 7 January 2010, Orlando, Florida.
- Akay B., Kurtulus D.F., (2009). Unsteady Aerodynamic Computations of different Sinusoidal Flapping Motions. International Symposium, Light Weight Unmanned Aerial Vehicle Systems and Subsystems, Oostende, Belgium.
- Akay B., Kurtulus D.F., Alemdaroglu N., (2007). Parametrical Study of Sinusoidal Flapping Motion Aerodynamics. 4th Ankara International Aerospace Conference, Ankara, Turkey.
- Akay B., Kurtulus D.F., Alemdaroglu N., (2007). Unsteady Aerodynamics of Different Wing Profiles at Low Reynolds Number. NATO AVT-146 Symposium on Platform Innovations and System Integration for Unmanned Air, Land and Sea Vehicles, Florence, Italy.
- Kurtulus, D.F., Akay, B., Alemdaroglu N., (2006). Analysis of Flapping Motion Aerodynamics by Using Two Dimensional Circular Cylinder, (in Turkish). Kayseri 6th Aeronautical Symposium, Nevehir, Turkey.

Poster presentations

- Akay B., Micallef D., Simão Ferreira C., van Bussel G.J.W., (2012). Experimental analysis of the evolution of the HAWT root flow. The Science of making torque from wind Conference, Oldenburg, Germany.